Thermal Disinfection of HVAC Filters using Radiant Ceramic Heaters

By

Zoleikha Moghtader Gilvaei

A thesis submitted in partial fulfillment of the requirements for the degree of

Master of Science

in

Civil (Cross-disciplinary)

Department of Civil and Environmental Engineering

University of Alberta

© Zoleikha Moghtader Gilvaei, 2025

Abstract

This research investigates a novel method for disinfecting pleated HVAC filters through radiation-based treatment using ceramic infrared heaters. The proposed system aims to inactivate microorganisms captured on the filter surface by elevating its temperature to the thermal disinfection threshold (65 ℃) without significantly affecting filter integrity or energy efficiency.

An experimental setup was designed and constructed to evaluate the influence of system geometry and operating conditions on thermal performance. The temperature distribution across the filter surface were recorded to identify optimal configurations that achieve uniform heating with the minimum energy consumption. View factor calculations based on radiation fundamentals were performed to interpret the radiative contribution to heating, and the CFD simulations were carried out to verify the experimental temperature trends.

Results showed that in the aluminum-covered gate configuration with a single ceramic heater, the most uniform temperature distribution was achieved at a heater–filter distance of 25 cm and a tilt angle of $\alpha = 10$ °, resulting in a total temperature difference of 13.0 ℃ across the filter after a 26-minute disinfection period, with a total electrical energy consumption of 0.05 kWh. Subsequent experiments using a transparent-gated chamber equipped with two ceramic heaters demonstrated a marked improvement in performance, achieving complete filter disinfection within 17 minutes at a tilt angle of $\alpha = 0$ ° and a heater–filter distance of 35 cm, while consuming only 0.09 kWh of electrical energy with a maximum temperature difference of 8.0 ℃ .

The findings confirm that with proper configuration, the proposed system can reliably reach the disinfection temperature with reasonable energy demand, offering a practical and sustainable solution for thermal disinfection of HVAC filters.

Preface

This research is the original work by Zoleikha Moghtader Gilvaei. The experiments, their design, and equipment calibration were mainly done in collaboration with Dr. Mahmood Salimi and Ali Mirzazade Akbarpoor. No part of this research has been previously published.

Acknowledgement

I would like to express my deepest gratitude to my supervisors, Dr. Alireza Nouri, and Dr. Mahdi Shahbakhti for their invaluable guidance, continuous support, and encouragement throughout this project.

I would also like to extend my heartfelt thanks to Dr. Mahmood Salimi, our lab research assistant and my peer coach, for his exceptional technical assistance, patience, and constant support throughout my experiments and analyses.

I am grateful to my lab mates, Adib and Erfan, for their collaboration, friendship, and the many stimulating discussions we shared.

My deepest appreciation goes to Ali, my husband and peer coach in the lab. His unwavering support, encouragement, and understanding have been my greatest source of strength throughout this journey. His insightful feedback, technical guidance, and constant motivation helped me overcome many challenges along the way. I am profoundly thankful for his love, patience, and belief in me.

This research was made possible through the generous funding and support of the Natural Sciences and Engineering Research Council of Canada (NSERC) and Engineered Air, whose contributions made experimental work and equipment procurement possible. I sincerely appreciate their support and the resources they provided for our research team.

Finally, I dedicate my deepest appreciation to my family in Iran, my parents and brother, for their endless love, sacrifices, and encouragement from afar. Their faith in me has been my greatest source of strength.

List of Content

Abstract ii
Preface iii
Acknowledgement iv
List of Content v
List of Tables viii
List of Figures ix
Nomenclature xvi
Chapter 1. Introduction & Background 1
1.1 Preface 1
1.2 Overview and Problem Statement 2
1.3 Research Questions 4
1.4 Research Objectives 5
1.5 Research Hypothesis 5
1.6 Research Methodology 6
1.7 Thesis Outline 10
Chapter 2. Literature Review & Research Gap 12
2.1 Preface 12
2.2 Existing Commonly Used Disinfection Technologies 12
2.2.1 Conventional Filters 13
2.2.2 Electrostatic Filters 15
2.2.3 Antimicrobial Filters 16
2.2.4 Photocatalysis Oxidation 16
2.2.5 Plasma 16
2.2.6 Ozonation 17
2.2.7 Thermal Treatment 17
2.2.8 Ultraviolet and Microwave 18
2.3 Heat-based Disinfection Technologies 20
2.4 Radiation-based Disinfection Technologies 25
2.5 Novelty and Contributions 30
Chapter 3. Experimental Methodology & Setup 33

3.1 Preface 33
3.2 Experimental Setup Description 33
3.3 Experimental Cases 41
3.4 Uncertainty Analysis 43
3.5 Chapter summary 45
Chapter 4. Radiative Heat Transfer Analysis and Numerical Simulation 46
4.1 preface 46
4.2 Radiation Exchange: Fundamentals to Two-Surface Enclosures 46
4.2.1 Governing Equations for View Factor Determination 48
4.2.2 Application of Shape Factor Equations to the Filter Subsections 50
4.3 Numerical Analysis of Heat Distribution 54
4.3.1 Governing Equations 55
4.3.2 Surface-to-Surface (S2S) Radiation Model 56
4.3.3 Model Schematic and Boundary Conditions 58
4.3.4 Numerical Grid 59
4.3.5 Solver Setup 61
4.3.6 Sensitivity Analyses 62
4.3.6.1 Grid Independence 62
4.3.7 Numerical modeling matrix 63
4.4 Chapter Summary 64
Chapter 5. Results and Discussion 65
5.1 Preface 65
5.2 Effect of Heater–Filter Distance on Filter Temperature Distribution 65
5.3 Effect of Heat Source Temperature on The Filter Temperature Distribution 73
5.4 The Impact of Increasing Tilt Angle of the Ceramic Heater 76
5.4.1 Measurement Uncertainty and Data Representation 82
5.5 The Impact of the Reflector Behind the Ceramic Heater 83
5.6 System Performance in the Duct without Aluminum-Foil-Covered Gates 86
5.6.1 Impact of Dual Ceramic Heaters in a Transparent-Gates Duct Configuration on the System Performance 92
5.6.1.1 Evaluation of Temperature Distribution and System Performance at $\alpha = 0\,°$ 94

5.6.1.2 Evaluation of Temperature Distribution and System Performance at $\alpha = 10\,°$ and $\alpha = 20\,°$ 99
5.7 Effect of Carbon Coating on the Thermal Performance of the System 102
5.8 Comparison between the Experimental Data and the Calculated View Factor 107
5.8.1 Dominant Mode of Heat Transfer: Identification the Radiation-Dominant Period ... 109
5.8.2 Experimental Results and Temperature Distribution Analysis 113
5.8.2.1 Effect of Heater–Filter Distance on Temperature Distribution.....116
5.8.2.2 Effect of Heater Tilt Angle on Temperature Distribution 120
5.9 Comparison of Experimental Results and the Numerical Study 124
5.9.1 Uncertainty Analysis of Filter Properties and Boundary Conditions..... 125
5.9.1.1 Effect of Boundary Conditions 126
5.9.2 Effect of Thermal Conductivity 127
5.9.3 Verification of Heater Orientation Effects 129
Chapter 6. Conclusion and Future Work 135
6.1 Conclusion 135
6.2 Current Research Limitations and Future Recommendations 138
References 142
Appendix A- Matlab Code for View Factor Analysis 156
Appendix B- Experimental Results Using Two Ceramic Heaters 160

List of Tables

Table 3.1. Summary of key parameters used in the experiments..... 41
Table 3.2 Spreadsheet model showing the uncertainty budget..... 44
Table 4.1. Summary of numerical simulation cases 64
Table 5.1. the effect of changing the tilt angle on temperature distribution over the filter 82
Table 5.2. Test Parameters for Dual Ceramic Heater Configuration 93
Table 5.3. Summary of test configurations that achieved successful filter disinfection using two ceramic heaters when the gates are transparent. 101
Table 5.4. Experimental parameters investigated in this study.....113
Table 5.5. Boundary condition definitions for the three simulated cases 126
Table B.1. Experimental results for filter disinfection using two ceramic heaters 160

List of Figures

Figure 1.1. Schematic of the experimental disinfection unit developed in this study. 4
Figure 1.2. Overall research methodology..... 9
Figure 2.1. A schematic representation of different disinfection technologies including (a) antimicrobial filtration, (b) thermal treatment, (c) UV, (d) electrostatic, (e) microwave, (f) photocatalysis, (g) plasma, and (h) ozonation (reproduced from Ref. [15])..... 13
Figure 2.2. Growth of microbes on the HEPA filters over time (adapted from Ref. [10]). 15
Figure 2.3. The required temperature and exposure time for thermal inactivation of various airborne pathogens [22], [51]–[59]. 20
Figure 2.4**.** Scheme of a proposed solution for thermal inactivation of airborne pathogens. 1. filter, either coarse or fine; 2. air supply device; 3. heat exchanger for heat recovery (to warm the inlet air and cool the outlet air); 4. heater to warm the air up to the specified maximum temperature; 5. thermal insulation..... 21
Figure 2.5. Experimental setup used by Karaboke et al. [78] to investigate the use of IR radiation for surface disinfection and virus deactivation. 28
Figure 2.6. Schematic of the (a) experimental setup and (b) Temperature measurement configuration used in the study by Demit et al.[82]..... 30
Figure 3.1. (a) Experimental setup and associated equipment; (b) interior view of the unit showing the pleated filter..... 35
Figure 3.2. Views of the ceramic heater device, including (a) the front surface with mounting clips, (b) rear electrical connections, and (c) side view showing the heater thickness. 37
Figure 3.3. Ceramic heater setup with an aluminum reflector mounted on the gate to intensify forward radiation and reduce heat dissipation. 37
Figure 3.4. Views of (a) regularMERV-11 filter and (b) carbon-coated MERV-11 filter..... 38
Figure 3.5. (a) Step-up ad down transformer used to convert the 110 V laboratory supply to 220 V for powering the ceramic heater; (b) power meter connected in the circuit to monitor real-time electrical consumption during the experiments. 39
Figure 3.6. PID temperature controller used in the experimental setup. 40
Figure 3.7. (a) Data logger with connected thermocouples, (b) placement of thermocouples on the front face of the pleated filter..... 41
Figure 4.1. Network element representing the net radiation transfer from a surface. 48

Figure 4.2. Radiation network analogy for two-surface exchange [87]. 50
Figure 4.3. The schematic of the heater–filter arrangement used in the view factor analysis. The filter is divided into three subsections (bottom, middle, and top), and the infrared heater is represented as a rectangular surface. 51
Figure 4.4. Geometric configuration of (a) two parallel rectangular surfaces and (b) two surfaces in planes inclined at an arbitrary angle α. (adapted from Ref. [88]). 52
Figure 4.5. View factors between two equal, parallel, and directly opposed rectangular surfaces as a function of normalized dimensions XL and YL. (Adapted from Ref. [87]). 53
Figure 4.6. The schematic of the numerical model: a) Complete domain, ... 59
Figure 4.7. Numerical grid: (a) full computational domain, (b) front view of the domain, (c) filter region. 61
Figure 4.8. Grid independence study: comparison of the predicted temperature distribution along the symmetry line of the filter surface for four mesh densities $\alpha = 0°$, $\varepsilon = 0.8$ and $Tsetpoint = 200$ ℃. 63
Figure 5.1. Temperature distribution over the filter over time at a ceramic heater temperature of 250°C and a distance of 100 cm. 67
Figure 5.2. Temperature distribution over the filter over time at a ceramic heater temperature of 250°C and a distance of 75 cm. 67
Figure 5.3. Temperature distribution over the filter over time at a ceramic heater temperature of 250°C and a distance of 50 cm. 68
Figure 5.4. Temperature distribution over the filter over time at a setpoint temperature of 250°C and a distance of 25 cm. 69
Figure 5.5. Temperature distribution over the filter over time at $Tsetpoint = 250$ ℃℃, and a distance of 15 cm. 69
Figure 5.5. Temperature distribution over the filter over time at a$Tset - point = 250$ ℃, and a distance of 10 cm. 70
Figure 5.7. Temperature distribution of different points of the filter over time at D=75 cm and $Tsetpoint = 250$ ℃ 71
Figure 5.8. Temperature distribution of different points of the filter over time at D=50 cm and $Tsetpoint = 250$ ℃ 72

Figure 5.9. Temperature distribution of different points of the filter over time at D=25 cm and $Tsetpoint = 250$ ℃ 72
Figure 5.10. Temperature distribution of different points of the filter over time at D=15 cm and $Tsetpoint = 250$ ℃ 73
Figure 5.11. Temperature distribution over the filter over time at D=50 cm and $Tsetpoint = 300$ ℃ 74
Figure 5.12. Temperature distribution over the filter over time at D=10 cm and (a) setpoint temperature of 220 ℃ and (b) 180 ℃ 76
Figure 5.13. Temperature variation over the top (a), middle (b), and bottom (c) sections of the filter front surface at tilt angles of $\alpha = 0°$, $\alpha = 10°$, and $\alpha = 20°$, at D=25 cm and $Tset - point = 250$ ℃ 77
Figure 5.14. Temperature variation over the top, middle, and bottom regions of the filter front surface at tilt angles $\alpha = 0°$, and $\alpha = 20°$, at D=25 cm and $Tset - point = 250$ ℃ 78
Figure 5.15 a. Temperature distribution on the filter front at D=10 cm, $Tsetpoint = 250$ ℃, and $\alpha = 10$ °. 79
Figure 5.15 b. Temperature distribution on the filter front at D=10 cm, $Tsetpoint = 250$ ℃, and $\alpha = 20$ °. 79
Figure 5.16. Temperature distribution on the filter front at $Tsetpoint = 220$ ℃, D=10 cm, and at $\alpha = 20$ °. 80
Figure 5.17 a. Temperature distribution on the filter front at D=15 cm, $Tsetpoint = 250$ ℃, and $\alpha = 10$ ° 81
Figure 5.17 b. Temperature distribution on the filter front at D=15 cm, $Tsetpoint = 250$ ℃, and $\alpha = 20$ °. 81
Figure 5.18 a. Temperature distribution on the filter front D=20 cm, $Tsetpoint = 250$ ℃, and $\alpha = 10$ °. 81
Figure 5.18 b. Temperature distribution on the filter front at D=25 cm, $Tsetpoint = 250$ ℃, and $\alpha = 20$ °. 81
Figure 5.19. Average filter temperature during 25 minutes at $D = 25\,cm, \alpha = 20$ °, and $Tsetpoint = 250$ ℃. Error bars represent the 99% confidence interval of five repeated measurements (n = 5). 83

Figure 5.20. Temperature distribution on the filter front at D=25 cm, $\alpha = 20\,°$, and $Tsetpoint = 250\,℃$, when the aluminum reflector is removed 84
Figure 5.21. Temperature distribution at the (a) Bottom, (b) Middle and (c) Top side of the filter front over a 25-minute heating period, with and without the aluminum reflector at D= 25 cm, $\alpha = 20\,°$ and $Tset - point = 250\,℃$..... 86
Figure 5.22. Schematic representation of the test duct setup used for evaluating a ceramic heater performance in a duct without aluminum foil-covered gates. 87
Figure 5.23. Experimental setup used to evaluate the ceramic heater performance in a duct without aluminum foil-covered gates. (a) Front view of the duct showing the transparent polycarbonate wall after removing the aluminum. (b) Internal view of the duct showing the ceramic heater placed in front of the pleated filter, ... 88
Figure 5.24a. Temperature distribution across the filter using one ceramic heater set to 250 ℃, at D= 10 cm and $\alpha = 0\,°$ with transparent gates 89
Figure 5.24b. Temperature distribution across the filter using one ceramic heater set to 250 ℃, at D= 10 cm and $\alpha = 20\,°$ with transparent gates 89
Figure 5.25a. Temperature distribution across the filter using one ceramic heater set to 250 ℃, at D= 15 cm and $\alpha = 0\,°$ with transparent gates 89
Figure 5.25a. Temperature distribution across the filter using one ceramic heater set to 250 ℃, at D= 15 cm and $\alpha = 20\,°$ with transparent gates 89
Figure 5.26a. Temperature distribution across the filter using one ceramic heater set to 300 ℃, at D= 10 cm and $\alpha = 20\,°$ with transparent gates 90
Figure 5.26b. Temperature distribution across the filter using one ceramic heater set to 350 ℃, at D= 10 cm and $\alpha = 20\,°$ with transparent gates 90
Figure 5.27a. Temperature distribution across the filter using one ceramic heater set to 300 ℃, at D= 15 cm and $\alpha = 20\,°$ with transparent gates 91
Figure 5.27b. Temperature distribution across the filter using one ceramic heater set to 350 ℃, at D= 15 cm and $\alpha = 20\,°$ with transparent gates 91
Figure 5.28. Temperature distribution across the filter using one ceramic heater set to 300 ℃, at D= 25cm and $\alpha = 0\,°$ with transparent gates 91
Figure 5.29a. Temperature distribution across the filter using one ceramic heater set to 300 ℃, at D= 25 cm and $\alpha = 20\,°$ with transparent gates 92

Figure 5.29b. Temperature distribution across the filter using one ceramic heater set to 350 ℃, at D= 25 cm and $\alpha = 20\,^{\circ}$ with transparent gates 92
Figure 5.30. Schematic representation of the test duct setup used for evaluating two ceramic heaters performance in a duct without aluminum foil-covered gates. 94
Figure 5.31. Temperature distribution across the filter using two ceramic heaters set to 180 ℃, at D= 10 cm and $\alpha = 0\,^{\circ}$ with transparent gates 95
Figure 5.32. Temperature distribution across the filter using two ceramic heaters set to 180 ℃, at D= 15 cm and $\alpha = 0\,^{\circ}$ with transparent gates 95
Figure 5.33. Temperature distribution across the filter using two ceramic heaters set to 200 ℃, at D= 15 cm and $\alpha = 0\,^{\circ}$ with transparent gates 96
Figure 5.34a. Temperature distribution across the filter using two ceramic heaters set to 200 ℃, at D= 25 cm and $\alpha = 0\,^{\circ}$ with transparent gates 97
Figure 5.34b. Temperature distribution across the filter using two ceramic heaters set to 220 ℃, at D= 25 cm and $\alpha = 0\,^{\circ}$ with transparent gates. 97
Figure 5.35. Temperature distribution over the filter over time using two ceramic heaters with temperature of 220°C a distance of 35 cm with 0 ° tilt angle in a duct with transparent gates. ... 98
Figure 5.36a. Temperature distribution across the filter using two ceramic heaters set to 220 ℃, at D= 25 cm and $\alpha = 10\,^{\circ}$ with transparent gates. 100
Figure 5.36b. T Temperature distribution across the filter using two ceramic heaters set to 220 ℃, at D= 25 cm and $\alpha = 20\,^{\circ}$ with transparent gates. 100
Figure 5.37a. Temperature distribution across the filter using two ceramic heaters set to 220 ℃, at D= 35 cm and $\alpha = 10\,^{\circ}$ with transparent gates. 100
Figure 5.37b. Temperature distribution across the filter using two ceramic heaters set to 220 ℃, at D= 35 cm and $\alpha = 20\,^{\circ}$ with transparent gates. 100
Figure 5.38. Temperature distribution over time across different sections of the filter using two ceramic heaters at $Tsetpoint = 220$ ℃, D= 35 cm and $\alpha = 0\,^{\circ}$ with transparent gates. 101
Figure 5.39. Front and back sides of the pleated filter showing the (a) carbon-coated surface and (b) the polyester fiber surface. 103
Figure 5.40. Temperature distribution over the filter at D=15 cm, $\alpha = 0\,^{\circ}$, and $Tsetpoint = 220$ ℃, with the gates covered by aluminum foil. (a) heater facing the carbon-coated side of the filter, and (b) heater facing the uncoated side. 104

Figure 5.41. Temperature distribution over (a) carbon-coated side of the filter and (b) uncoated side of the filter, at D=35 cm, $\alpha = 0$ °, and $Tsetpoint = 220$ ℃, with the transparent gates. . 105
Figure 5.42. Temperature distribution across three sections of the filter for both the carbon-coated and regular polyester cases at D $= 35$ cm, $Tsetpoint = 300$ ℃, and $\alpha = 0$ °: (a) top section, (b) middle section, and (c) bottom section..... 107
Figure 5.43. Aluminum frame cover used to stabilize the ceramic heater temperature before exposing the filter..... 109
Figure 5.44. Temperature variation at the top, middle, and bottom sections of the filter with transparent gates and the ceramic heater stabilized at the setpoint temperature before exposure (D = 10 cm, $Tset - point = 200$ ℃, α = 20°): (a) full heating period; (b) zoomed-in view of 1–5 minutes.....110
Figure 5.45. a) Temperature rise across the filter sections at $D = 10\ cm, \alpha = 0$ °, $Tset - point = 250$ ℃, $t = 10\ s$, b) corresponding calculated heater–filter view factors at the same configuration. 115
Figure 5.46. Effect of heater–filter distance on (a) temperature rise across the top, middle, and bottom sections of the filter relative to the initial condition at different distances for $\alpha = 0$ °, $Tset - point = 250$ ℃ and (b) the corresponding view factors between the ceramic heater and the filter at different distances for $\alpha = 0$ °.....117
Figure 5.47. Effect of heater–filter distance on (a) temperature rise across the top, middle, and bottom sections of the filter relative to the initial condition at different distances for $\alpha = 10$ °, $Tset - point = 250$ ℃ , $t = 10\ s$ and (b) the corresponding view factors between the ceramic heater and the filter at different distances for $\alpha = 10$ °. 118
Figure 5.48. Effect of heater–filter distance on (a) temperature rise across the top, middle, and bottom sections of the filter relative to the initial condition at different distances for $\alpha = 20$ °, $Tset - point = 250$ ℃ , $t = 10\ s$ and (b) the corresponding view factors between the ceramic heater and the filter at different distances for $\alpha = 20$ °. 119
Figure 5.49. Effect of heater tilt angle on (a) temperature rise across the top, middle, and bottom sections of the filter relative to the initial condition at different distances for $D = 10\ cm$, $Tset - point = 250$ ℃ , $t = 10\ s$ and (b) the corresponding view factors between the ceramic heater and the filter at different tilt angle for $D = 10\ cm$..... 121

Figure 5.50. Effect of heater tilt angle on (a) temperature rise across the top, middle, and bottom sections of the filter relative to the initial condition at different distances for $D = 15\ cm$, $Tset - point = 250$ ℃ , $t = 10\ s$ and (b) the corresponding view factors between the ceramic heater and the filter at different tilt angle for $D = 15\ cm$. 122
Figure 5.51. Effect of heater tilt angle on (a) temperature rise across the top, middle, and bottom sections of the filter relative to the initial condition at different distances for $D = 25\ cm$, $Tset - point = 250$ ℃ , $t = 10\ s$ and (b) the corresponding view factors between the ceramic heater and the filter at different tilt angle for $D = 25\ cm$. 123
Figure 5.52. Schematic of the experimental setup for comparison with the numerical results. The pleated HVAC filter was mounted vertically inside an insulated enclosure, while a ceramic heater was positioned at an adjustable tilt angle in front of the filter. 125
Figure 5.53. Comparison of experimental results with numerical simulations under different boundary condition assumptions at $\alpha = 0°$, $\varepsilon = 0.8$, $k = 0.14\ wmK$, $Tsetpoint = 200$℃. .. 127
Figure 5.54. Comparison of experimental and numerical temperature distributions along the filter height for two thermal conductivity assumptions with $\varepsilon = 0.8$, $\alpha = 0°$, and $Tsetpoint = 200$℃. 129
Figure 5.55. Experimental temperature distribution along the filter height for different tilt angle. 131
Figure 5.56. Experimental temperature distribution along the filter height for different tilt angle 131
Figure 5.57. Comparison of experimental and numerical temperature distributions along the filter height at three heater tilt angles: (a) $\alpha = 0$ °, (b) $\alpha = 10$ °, and (c) $\alpha = 20$ °. 134

Nomenclature

Symbol	Definition	Symbol	Definition
q_i	Net radiative heat transfer from surface i, (W)	k	Thermal conductivity, $(W/m\,K)$
A_i	Surface area of surface i, (m^2)	T_∞	Ambient temperature, (°C)
J_i	Radiosity of surface i, (W/m^2)	T_a	Air temperature, (°C)
G_i	Irradiation incident on surface i, (W/m^2)	h	Convective heat transfer coefficient, $W/m^2\,K$
E_i	Emissive power of surface i, (W/m^2)	g	Acceleration due to gravity, (m/s^2)
F_{1-2}	View factor from surface 1 to 2	q_r	Radiative heat flux, (W)
E_b	Blackbody emissive power, (W/m^2)	q_c	Convective heat flux, (W)
Ra	Rayleigh number	N_{rc}	Radiation-to-convection ratio
Nu	Nusselt number	$T_{set-point}$	Ceramic heater setpoint temperature, (°C)
Pr	Prandtl number	D	Distance between heater and filter, (cm)
s	Distance between surfaces, (m or cm)	A_h	Surface area of heater, (m^2)
z	Vertical offset between surfaces, (m or cm)	A_f	Surface area of filter, (m^2)
x, y	Coordinate variables (m)		

Greek		Subscript	
σ	Stefan–Boltzmann constant (5.67×10^{-8}), (W/m^2K^4)	i	Index
ε_i	Emissivity of surface i	r	Radiation

ρ_{i}	Reflectivity of surface i	c	Convection
α_{i}	Absorptivity of surface i	h	Heater
α	Tilt angle between heater and filter, (°)	f	Filter
φ_i	Orientation angles of surfaces i, (°)		
ν	Kinematic viscosity, (m^2/s)		
β	Thermal expansion coefficient, $(1/T)$		
Ra	Rayleigh number		
Nu	Nusselt number		
Pr	Prandtl number		
ξ, η	Coordinate variables, (m)		

Abbreviations

CFD	Computational Fluid Dynamics
S2S	Surface-to-Surface radiation model
HVAC	Heating, Ventilation, and Air Conditioning
IR	Infrared Radiation
HEPA	High-Efficiency Particulate Air
MERV	Minimum Efficiency Reporting Value

Chapter 1. Introduction & Background

1.1 Preface

Airborne pathogens have been responsible for several recent pandemics, such as the H1N1 influenza and the novel coronavirus (SARS-CoV-2), along with its highly contagious variants, including Delta and Omicron. Globalization, growing international travel and trade, rapid urbanization, crowded living conditions, changes in human behaviour, the reemergence of dormant pathogens, and the misuse of antibiotics all contribute to the increasing threat of infectious and deadly diseases. The health and economic impacts of pandemics are profound. According to World Health Organization (WHO) data, by the end of 2022, more than 700 million COVID-19 cases had been reported worldwide, resulting in nearly seven million deaths [1–3].

The transfer of respiratory pathogens from one individual to another usually happens in three main ways; contact, droplets, and airborne transmission. Contact transmission can occur through direct physical interaction or indirectly via contaminated surfaces (fomites). In droplet transmission, relatively large respiratory particles ($> 20\ \mu m$) are released through actions such as coughing, sneezing, or speaking, and they usually settle within one meter under the effect of gravity [4,5]. In contrast, airborne transmission involves smaller particles, known as droplet nuclei, which form when larger droplets evaporate. These nuclei, usually under 5–10 μm in size, remain suspended in the air for extended periods and can travel greater distances, reaching deeper areas of the respiratory system [6,7]. Although airborne transmission has been studied for many years, it gained renewed attention during the COVID-19 pandemic. In recent decades, health authorities revised their protocols. The Studies of health authorities in the middle of 2020 have shown that viruses spread mainly through airborne particles rather than respiratory contact, and droplets. This

realization underscored the urgent need to improve our understanding of airborne transmission in order to more effectively control COVID-19 and other respiratory infections [4,8].

Today, most of the people spend much of their time inside buildings; therefore, proper thermal comfort and indoor air quality (IAQ) are vital. According to WHO [9], poor IAQ causes more than 4.6 million preventable deaths worldwide, showing how important well-designed heating, ventilation, and air conditioning (HVAC) systems are for health. Ventilation is essential for keeping indoor air clean. However, if HVAC systems are poorly designed or not properly maintained, for example, when airflow is too low or the number of air changes per hour (ACH) is insufficient, they can actually spread pathogens through ducts and air circulation. This increases the likelihood of transmitting viruses, bacteria, and fungi [10–12].

1.2 Overview and Problem Statement

The current study introduces a novel heat-based disinfection technology designed to overcome the limitations of existing disinfection methods. This thesis investigates the integration of ceramic infrared (IR) heaters with pleated HVAC filters to both capture and inactivate pathogens accumulated on the filter surface. By integrating air filtration and localized heating, this approach aims to enhance indoor air quality while minimizing the risks associated with microbial survival and re-entrainment in ventilation systems.

The proposed infrared ceramic heating system can be applied in a wide range of HVAC configurations in both residential and commercial buildings, including offices, schools, and hospitals. It can be integrated within both ductwork and air-handling units (AHUs) without major system modifications. This technology is particularly suitable for systems that do not operate

continuously. When the HVAC unit is shut off, the infrared ceramic heaters can be employed to disinfect the filter media. This ensures that the disinfection process is both energy-efficient and can be scheduled during downtime, and prevents interference with regular ventilation operation. The system is most effective with pleated MERV-rated filters commonly used in HVAC systems; however, it is not recommended for high-efficiency particulate absorbing (HEPA) filters due to their greater thickness and higher thermal resistance [13].

Figure 1.1 presents a schematic representation of the proposed disinfection system. The system primarily consists of ceramic infrared heaters, pleated HVAC filters, an aluminum-foil-covered enclosure, and two gates located at the front and back of the unit. The ceramic infrared heater is strategically positioned upstream of the pleated filter in different configurations. These arrangements are intended to examine how heater and filter configurations affect the distribution of thermal energy across the filter surface, thereby influencing temperature uniformity, pathogen inactivation, and overall disinfection efficiency. By evaluating multiple configurations, the study aims to identify the optimal design that achieves effective microbial inactivation while maintaining energy efficiency.

The ceramic heater is mounted on the front gate of the unit, allowing adjustment of the heater-to-filter distance and regulation of the enclosure size. An aluminum plate is placed directly behind the heater to serve as a reflector, and the inner walls of the enclosure are lined with aluminum foil to minimize heat loss.

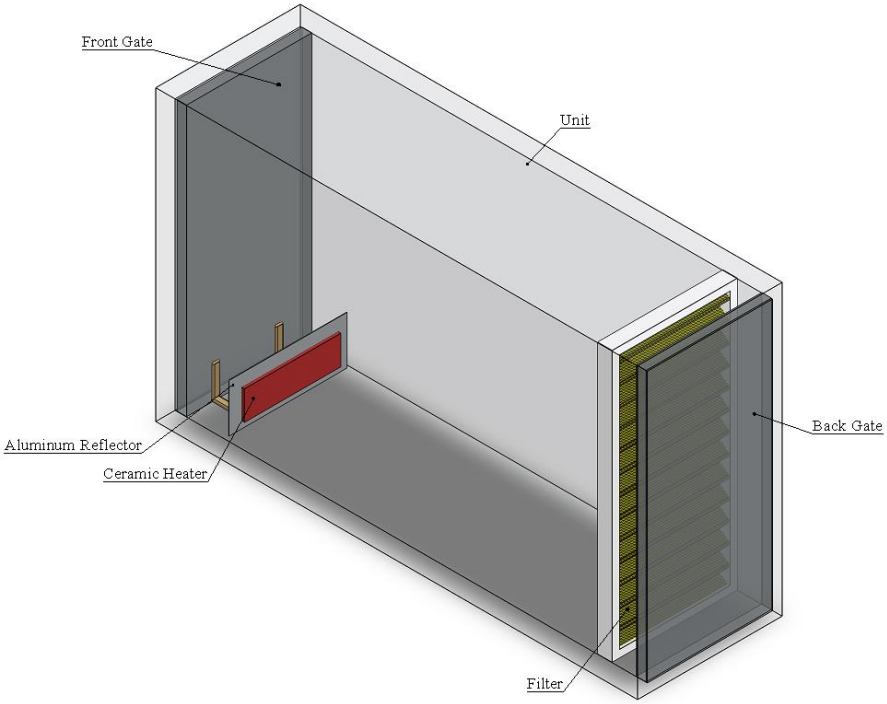

Figure 1.1. Schematic of the experimental disinfection unit developed in this study.

1.3 Research Questions

This study aims to answer the following research questions:

1. How does the placement of ceramic infrared heaters (distance and tilt angle) influence the temperature distribution across pleated HVAC filters?
2. What differences in heating uniformity arise between single-heater and dual-heater configurations?
3. How do enclosure and surface modifications, such as aluminum reflectors or carbon-coated filters, affect heat absorption and distribution?
4. Can analytical calculations and numerical simulations reliably predict the experimental thermal behaviour of the heater–filter system?

1.4 Research Objectives

The roadmap of this thesis to address the above research questions includes the following objectives:

1. Investigate the effects of heater placement parameters, including distance and tilt angle, on the temperature distribution across the filter surface and total energy consumption.
2. Evaluate the performance of single- and dual-heater configurations under transparent gate conditions that replicate real HVAC systems when fans are off, in order to determine the feasibility of ceramic heaters for in-situ disinfection during idle operation.
3. Examine how enclosure design and filter surface modifications, such as aluminum reflectors and carbon coatings, affect heat absorption and distribution.
4. Conduct analytical (view factor) calculations to illustrate the governing radiation principles and assess the influence of geometrical factors on heat transfer, and perform numerical simulations to reproduce the experimental temperature patterns.

1.5 Research Hypothesis

This research is based on the idea that combining ceramic infrared heaters with pleated HVAC filters can provide an effective way to disinfect microorganisms directly on the filter surface. The hypothesis is that with the proper placement and configuration of heaters, it is possible to create uniform and sufficient heating on the filter surface to inactivate pathogens, while still keeping the filter performance intact and avoiding unnecessary energy use.

The following hypotheses are proposed:

1. Polyester fibers, due to their high emissivity and low thermal conductivity, are expected to absorb radiant heat efficiently from ceramic heaters, resulting in an energy-efficient system.
2. Because air is essentially transparent to radiation, no additional energy is required to preheat the air, which further improves overall system efficiency.
3. Filter surface heating uniformity is highly influenced by the heater–filter distance, tilt angle, and overall filter size. When the distance is too large, non-uniform heating occurs because of convection effects and reduced radiative coverage, whereas very short distances can cause localized overheating. Achieving an optimal arrangement of these parameters enables a more uniform temperature distribution across the pleated surface.
4. Filters with higher absorptivity, such as carbon-coated polyester, are expected to achieve higher surface temperatures than uncoated filters under identical heating conditions.
5. At the start of the heating process, heat transfer is governed mainly by radiation, but as time progresses and air movement develops, natural convection plays an increasingly important role.

1.6 Research Methodology

This research uses a combined approach of experiments, analytical work, and numerical simulations to test the hypotheses and answer the research questions. In the experimental part, the focus is on how different factors affect system performance, including the distance between the heater and filter (10–100 cm), the heater tilt angle ($0°, 10°, 20°$), the use of single versus dual heaters, and enclosure conditions such as transparent gates or aluminum foil coverings. Additional tests examine whether modifying the filter surface, for example by adding a carbon coating,

enhances heat absorption and distribution. Performance is evaluated by tracking the temperature distribution across the filter, the uniformity of heating, whether the filter surface reaches the target disinfection temperature of 65 ℃, and energy efficiency. All experiments are carried out in an enclosure measuring $32\ cm \times 65\ cm \times 120\ cm$. To support these experiments, radiative heat transfer calculations based on view factor analysis are performed to understand better how geometry and exposure affect heating. For the numerical simulations, ANSYS Fluent 2023 R2 was used to verify the experimental measurements and establish a framework for future system design. At a fixed heater–filter distance, the simulations examined how changes in tilt angle influence the temperature distribution across the filter surface, and the results were compared directly with the experimental data.

In summary, the experiments provide real measurements, while the analytical and numerical studies are employed to interpret the findings. Ultimately, the system is evaluated based on its ability to deliver uniform heating, achieve the required disinfection temperature, and operate efficiently.

The overall research methodology adopted in this study is summarized in Figure 1.2. The process begins with an extensive literature review focused on the existing disinfection technologies, heat-based disinfection technologies, and radiation-based disinfection technologies. This review helped identify the key research gap and define the main experimental design parameters required for developing the proposed system.

Following the literature review, the research proceeds along two complementary pathways. The theoretical modeling branch includes both numerical simulation and view factor analysis. The numerical simulation component involves defining the computational geometry and domain in ANSYS Fluent. The simulation results are then compared with the experimental data for the

verification. In parallel, the view factor analysis defines the heater and filter geometries and calculates the radiative exchange factors to determine how tilt angle and spacing influence the radiative heat transfer. This analysis provides a qualitative understanding of the system's thermal behavior.

The experimental modeling branch involves the design and fabrication of the disinfection unit. The collected temperature data are analyzed to evaluate temperature distribution, heating uniformity, and energy consumption.

Finally, the insights obtained from both the theoretical and experimental pathways are integrated to identify the optimal heater–filter configuration that achieves effective and energy-efficient thermal disinfection.

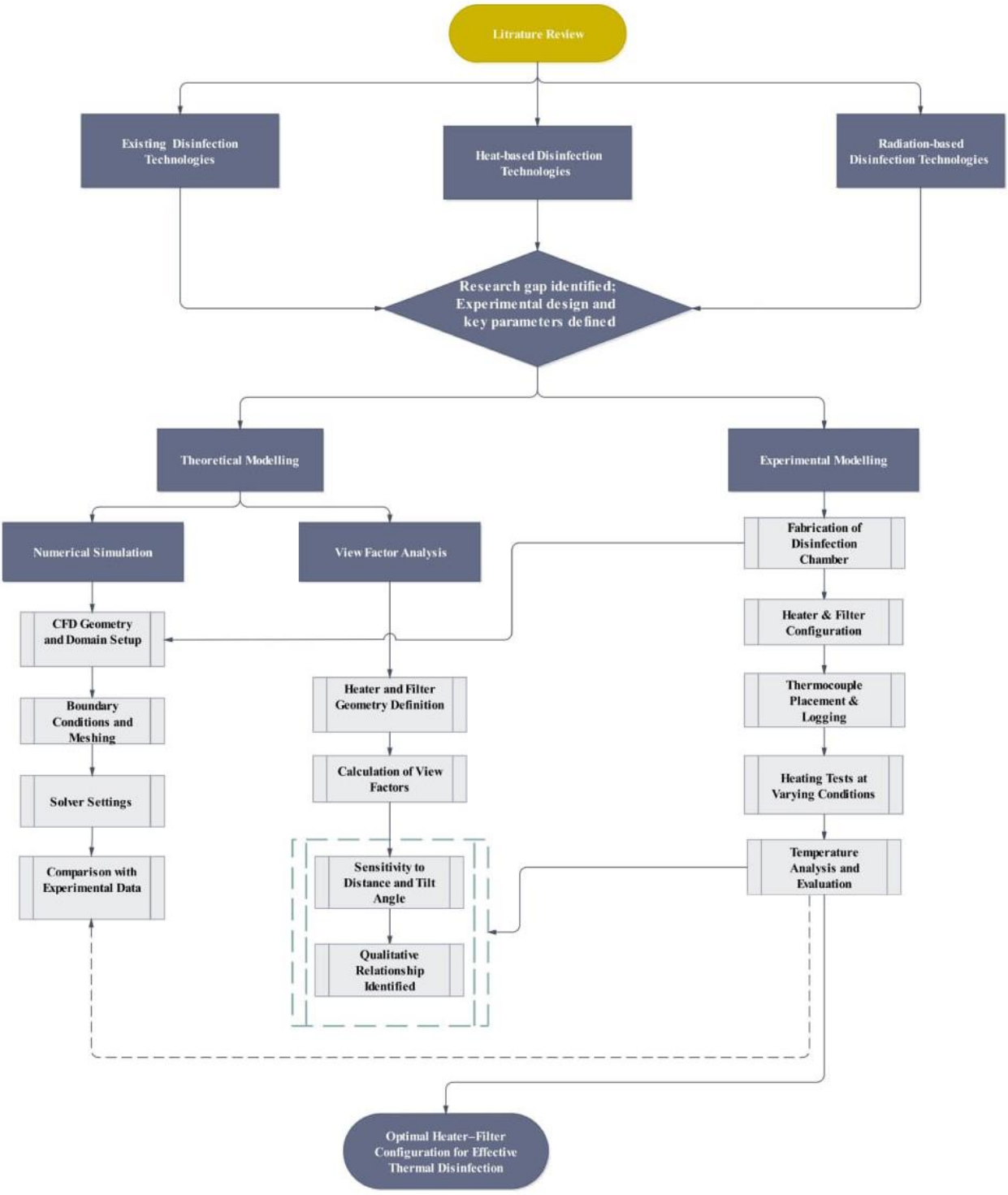

Figure 1.2. Overall research methodology

1.7 Thesis Outline

This thesis includes 7 main chapters. The content of each chapter is briefly introduced below.

Chapter 1 introduces the research motivation, problem statement, research questions, objectives, and hypothesis. It also outlines the adopted methodology and presents the overall structure of the thesis.

Chapter 2 provides a comprehensive review of existing disinfection technologies applied in HVAC systems. The review then emphasizes thermal and radiation-based disinfection approaches, which are particularly relevant to the objectives of this work. The chapter concludes by identifying the key research gaps that this thesis aims to address.

Chapter 3 describes the experimental setup designed to investigate the disinfection of pleated HVAC filters. It details the test configurations, instrumentation, and procedures.

Chapter 4 presents the analytical and numerical methodologies developed to model heat transfer within the system. The first part outlines the analytical approach used to calculate radiation view factors between the ceramic heaters and the filter, including the governing equations and the application of shape factor formulas for the studied geometry. The second part describes the numerical model used to simulate heat transfer within the system. It includes the governing equations, boundary conditions, grid generation, solver settings, and sensitivity analyses, followed by key simulation cases.

Chapter 5 presents and discusses the experimental and numerical results. It evaluates the influence of system parameters such as heater-filter distance, tilt angle, presence of reflectors, and carbon coating on thermal performance. Comparisons between experimental data, view factor predictions, and a comprehensive computational fluid dynamics (CFD) simulations are also provided.

Chapter 6, the conclusion chapter, summarizes the key findings of this research. Additionally, it discusses the limitations faced during this research and provides recommendations for future research and development.

The thesis ends with references and appendices. The references cited in this research and supplementary data are included in this section.

Chapter 2. Literature Review & Research Gap

2.1 Preface

This chapter reviews the most commonly used disinfection technologies, highlighting their mechanisms, advantages, and limitations, with a particular focus on thermal and radiation-based methods. This review is divided into three sections. The first section presents an overview of various disinfection technologies, outlining their underlying principles, applications, and effectiveness across different settings. The second section focuses on heat-based disinfection methods, emphasizing how elevated temperatures can inactivate microorganisms. Finally, the third section examines disinfection through radiation, with a particular emphasis on ultraviolet (UV) and infrared radiation, and evaluates their relative efficiency in pathogen inactivation.

2.2 Existing Commonly Used Disinfection Technologies

Over recent decades, a wide range of methods for sterilizing and disinfecting pollutants and microorganisms have been extensively investigated to address challenges in maintaining indoor air quality. A schematic view of different disinfection technologies available in the literature is illustrated in Figure 2.1. These technologies play a critical role in safeguarding public health and ensuring reliable operation of indoor environments such as hospitals and commercial buildings [14]. Conventional filters, electrostatic filters, antimicrobial filters, photocatalysis oxidation, plasma, ozonation, thermal treatment, and radiation (including ultraviolet (UV) and microwave disinfection) are the main sterilization and disinfection systems [15]. These technologies will be briefly discussed in the following sections.

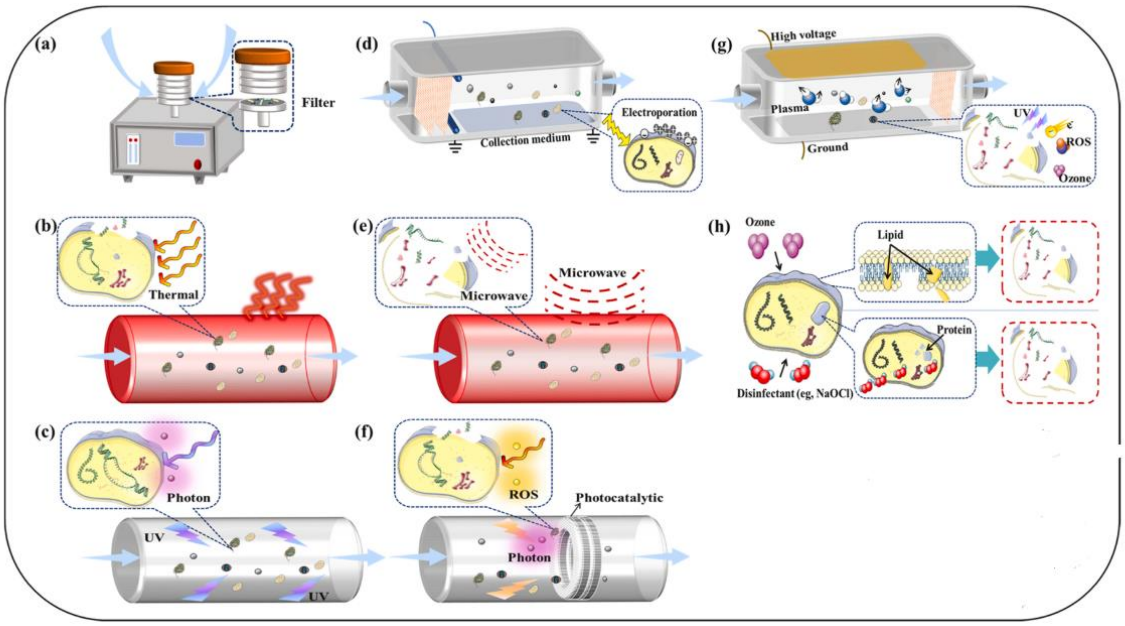

Figure 2.1. A schematic representation of different disinfection technologies including (a) antimicrobial filtration, (b) thermal treatment, (c) UV, (d) electrostatic, (e) microwave, (f) photocatalysis, (g) plasma, and (h) ozonation (reproduced from Ref. [15]).

2.2.1 Conventional Filters

Air filtration in HVAC systems plays an effective method in reducing the spread of airborne pathogens indoors [10,16]. Filters come in different grades of efficiency. For example, HEPA filters can capture 99.97% of particles as small as 0.3 microns that are especially concerning because they can penetrate deeply into the respiratory system [17]. While HEPA filters provide excellent removal efficiency, most HVAC systems still rely on conventional fibrous filters for routine air cleaning.

Conventional air filters utilize the adsorption properties of fibrous materials to capture microorganisms through three primary mechanisms: impaction, diffusion, and interception [15,18]. Conventional filters are widely used because of their low cost, ease of installation, and

commercial availability. However, they struggle to effectively capture smaller microorganisms, which can lead to secondary contamination and potentially become breeding grounds for fungi and bacteria as these particles may pass through the filter or become dislodged over time [19–21]. For example, Morisseau et al. [22] conducted several experimental tests to quantify the release of fungal particles from contaminated HVAC filters. In their study, it was shown that the proportion of particles discharged during system restart depends on the minimum efficiency rating value (MERV) of the filters. Coarse and low MERV filters released up to about 1% of their fungal load, while fine and high-MERV filters released only around 0.001%. Although these release rates appear minimal, filters can accumulate large microbial burdens during operation, meaning that even a small percentage of particles released may still translate into a significant number of viable spores entering the indoor air and threatening occupant health.

Additionally, when the filter is fully loaded and due for replacement, it may pose additional risks if not handled and disposed of properly. This demonstrates that filters, instead of serving only as protective barriers, can also act as sources of biological hazards due to microbial accumulation, as illustrated in Figure 2.2.

Another challenge of the filters is the pressure drop across the filter. This effect becomes worse as the filter loads with dust, leading to higher energy use and operating costs. Since the more resistant the filter is to airflow, the more energy the system needs to move air through it [23]. Given these challenges, it is important to explore strategies to improve filter performance and reduce associated risks. To enhance the efficiency of air filters and manage pressure drops, pleated filters can be employed [24]. Therefore, despite the fact that air filtration is crucial for enhancing indoor air quality, careful consideration of its limitations and proper maintenance is essential to ensure safety and efficiency.

Also, it is important to recognize that filtration serves primarily as a removal strategy and does not deactivate microorganisms. Therefore, supplementary disinfection technologies are necessary to address the limitations of filtration alone. Integrating these additional measures can provide a more comprehensive approach to improving indoor air quality and ensuring effective pathogen control [25].

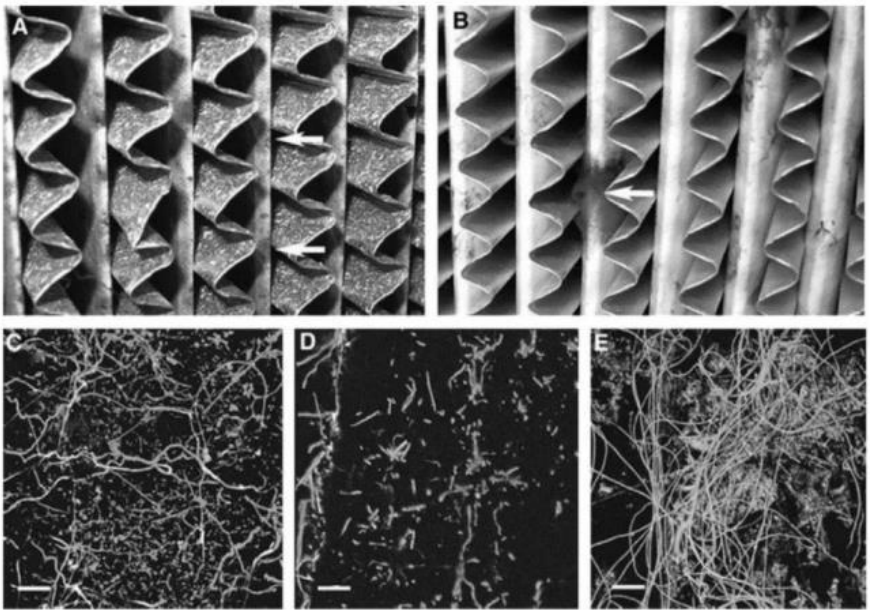

Figure 2.2. Growth of microbes on the HEPA filters over time (adapted from Ref. [10]).

2.2.2 Electrostatic Filters

These types of filters operate based on the application of electrostatic forces, including Coulomb forces between opposite charges, image forces, and polarization forces [26,27]. These filters are primarily designed for particle removal but can achieve partial inactivation as well. Their benefits include high efficiency across a broad range of particle sizes, a lower pressure drop compared to conventional filters, and commercial availability. However, they come with a high initial cost,

reduced efficiency due to dust accumulation, and a susceptibility to electric field breakdown under certain conditions [10,15].

2.2.3 Antimicrobial Filters

Antimicrobial filters employ metallic nanoparticle coatings to inactivate bio-aerosols captured on the filter surface [28,29]. These are mainly designed for inactivation. However, their performance is limited by the selective nature of the nanoparticles, which often target specific microorganisms rather than providing broad-spectrum activity. Additional drawbacks include a high initial cost, potential degradation in efficiency over time, and an increased pressure drop due to nanoparticle coatings [30,31].

2.2.4 Photocatalysis Oxidation

This disinfection method combines light with oxidation processes to generate reactive oxygen species, which effectively damage microbial cell structures. Titanium dioxide ($Ti\,O_2$) is commonly used as a catalyst to enhance this photoreaction due to its high efficiency [32,33]. This method is particularly valuable for its continuous disinfection capability and broad-spectrum antibacterial effects. However, the accumulation of particles on the catalyst surface may reduce its efficiency, and the catalyst itself generally has a limited operational lifespan. Another limitation of this technique is the generation of secondary by-products such as aldehydes and ketones [18,32,34].

2.2.5 Plasma

This disinfection technology utilizes an external electric field to generate electrons, which interact with bioaerosols and produce reactive chemical species that can damage airborne microorganisms [35,36]. This technique is capable of inactivating a diverse array of pollutants to reduce the growth

of adhering fungi and eliminate persistent odors. However, the potential generation of harmful by-products such as ozone, carbon monoxide, particulate matter, and formaldehyde is one of the drawbacks of using plasma disinfection technology. Additionally, plasma systems require operation by trained professionals and may not be cost-effective for large spaces [15].

2.2.6 Ozonation

In this method, corona discharge is used to produce ozone, which effectively inactivates microorganisms by damaging their cell membranes and proteins [37,38]. While this technique is fast and efficient against a wide variety of airborne organisms, it has several limitations. For example, production of ozone and secondary contaminants that can cause respiratory issues. As a result, ozonation is not recommended for use in occupied areas. Furthermore, ozone is inherently unstable and must be applied at carefully monitored concentrations right before usage to ensure both safety and effectiveness [37,39].

2.2.7 Thermal Treatment

This method involves the use of high temperatures, either through dry or moist heat, to eliminate bioaerosols by denaturing enzymes and proteins [40,41]. This method is characterized by its speed and high effectiveness, as it does not generate by-products and pose excessive pressure in the system. However, it requires high operating temperatures, which leads to high energy consumption. Thermal treatment is often not cost-effective for large spaces. It may add additional heat to HVAC systems and cause thermal deformation in some materials, and it is more suitable for applications in the food industry and the sterilization of medical equipment [40,42].

2.2.8 Ultraviolet and Microwave

Utilizing ultraviolet radiation in HVAC systems is one of the most common disinfection technologies. By incorporating UV lamps inside an HVAC system or a duct, engineers aim to use radiation to kill and inactivate pathogens. UV sterilization produces short-wavelength electromagnetic waves, with peak irradiance around 254 nm, to disrupt the DNA of pathogens and effectively prevent their replication [43,44]. This inactivation method is highly efficient, widely available commercially, requires no chemical additives, and creates minimal airflow resistance. UV exposure poses health risks, including skin erythema and eye damage (photokeratitis), and long-term exposure is carcinogenic. In addition, UV systems can produce ozone and free radicals and may introduce excess heat into HVAC systems, reducing overall efficiency [11,29,45,46].

Microwave disinfection technology operates via electromagnetic waves at frequencies of 300 to 3000 MHz. In this method, the induced heat generates non-ionizing electromagnetic waves that rapidly break down cell membranes, proteins, and enzymes. This method is effective in diminishing the production of unwanted disinfection by-products. Microwave disinfection is valued for its simplicity and reliability. However, potential health risks associated with microwave radiation limit its application, and it is primarily used in the food industry [47].

Despite the advantages of the technologies reported in the literature, the application of these technologies is linked to high capital costs, significant energy demands, the generation of harmful by-products, complex installation and maintenance procedures, and a decline in efficiency over time.

Among the different disinfection approaches, this study focuses especially on thermal disinfection. Heat-based inactivation is a highly effective method for eliminating a wide range of infectious microorganisms. Heat demonstrates a strong ability to penetrate material for neutralizing the

majority of infectious organisms by altering their enzymatic and protein structures. In addition, thermal treatment is recognized as an eco-friendly, effective, and safe approach for disinfecting microorganisms in HVAC systems [48–50]. Therefore, in the following sections, a thorough examination of heat-based disinfection technologies' effectiveness, applications, and operating principles are provided, along with references to the relevant literature.

Successful sterilization by heat depends primarily on two parameters: temperature and exposure time. Figure 2.3 shows the required temperature and exposure duration needed for inactivating some common airborne microorganisms. The findings indicate that most pathogens can be effectively neutralized when exposed to a steady temperature of about 65 ℃ for approximately 10 minutes [22,51–59]. This demonstrates that thermal treatment can play an important role in eliminating microorganisms trapped within HVAC filters. In the Figure 2.3, Escherichia coli, Mycobacterium tuberculosis, Legionella pneumophila, and Pseudomonas aeruginosa are classified as bacteria; Aspergillus, Penicillium, and Mucor are classified as fungi; while Rhinovirus (common cold), MERS-CoV, human influenza, MS2, avian influenza, SARS-CoV, and SARS-CoV-2 (COVID-19) are classified as viruses.

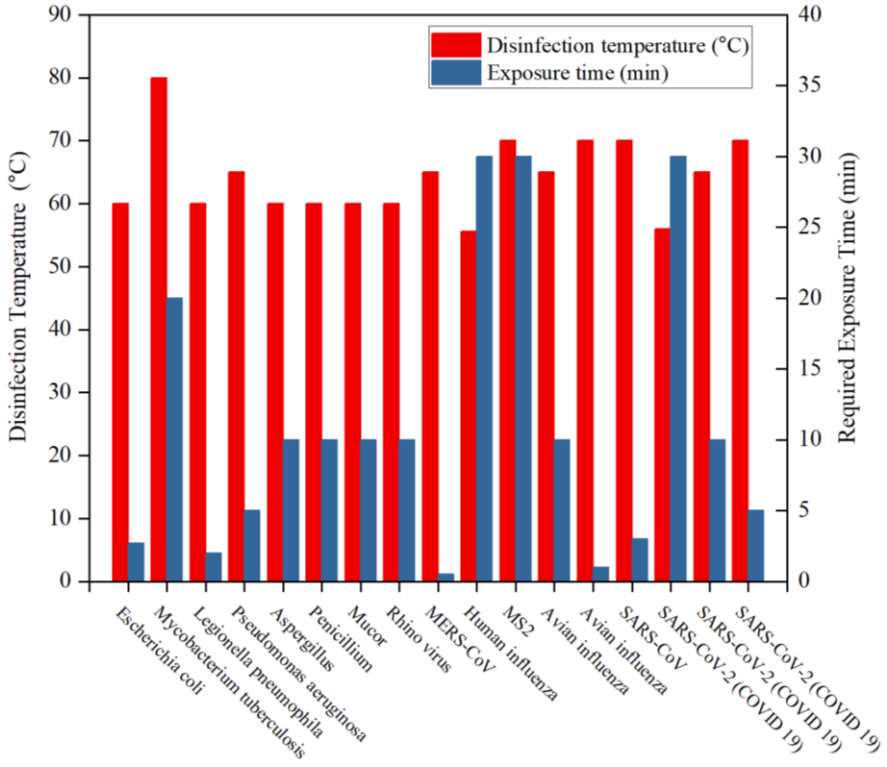

Figure 2.3. The required temperature and exposure time for thermal inactivation of various airborne pathogens [22,51–59].

2.3 Heat-based Disinfection Technologies

Heat-based technologies provide key advantages, such as ease of implementation and high efficient [41,60,61]. In this section, various aspects and applications of thermal disinfection across different systems are explored, providing a better understanding of the performance of this technology and its potential limitations. Grinshpun et al. [62] conducted an experimental investigation on the effects of axial heating in a continuous air flow chamber for the inactivation of aerosolized MS2 viruses. This system utilized dry heat without any moisture, with temperatures ranging from 50 to 300 ℃ and exposure times between 0.1 and 1 second. The results showed that at a temperature of 170 ℃ with a flow rate of 18 L/min and at a temperature of 250 ℃ with a flow rate of 30 L/min, 99.996% of viable virions were deactivated. Building on this experimental

evidence, Vlaskin [63] proposed a theoretical thermal inactivation system for air disinfection. His concept involves heating air to temperatures between 50 ℃ and 250 ℃ using a heat exchanger, followed by a cooling phase (Figure 2.4). According to the author, the effectiveness of this proposed system would depend on both temperature and exposure time. Though not experimentally validated, this system is suggested as adaptable for mobile personal disinfectors, stationary indoor air disinfectors, and HVAC systems. Overall, these studies demonstrate that heating air to high temperatures can effectively inactivate viruses, while more work is needed to turn this idea into practical and large-scale systems.

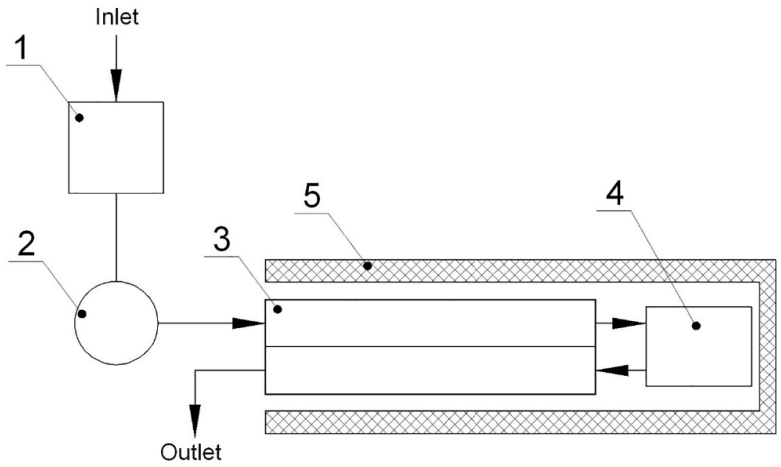

Figure 2.4**.** Scheme of a proposed solution for thermal inactivation of airborne pathogens. 1. filter, either coarse or fine; 2. air supply device; 3. heat exchanger for heat recovery (to warm the inlet air and cool the outlet air); 4. heater to warm the air up to the specified maximum temperature; 5. thermal insulation.

A range of studies has explored the application of solar thermal energy for disinfection purposes, specifically targeting the inactivation of viruses on various surfaces. One investigation by Sagade and Palma-Behnke [64], examined the practicality of using a solar thermal energy-based device to inactivate SARS-CoV-2 viruses from different surfaces, with a particular focus on cotton. The

researchers achieved a temperature range of 75 ℃ to 80 ℃, which is the required temperature for effective viral inactivation. Effective disinfection was achieved by sustaining the temperature range for 60 minutes. They also showed that the exergy efficiency of the proposed system varied from 12.62% to 22.69%. Therefore, the researchers concluded that this heat-based technology is an appropriate and cost-effective solution for reducing viruses; however, several improvements are required to minimize heat loss and extend its use to wider conditions.

In a complementary approach, Soni et al. [65] have also developed a numerical model for a solar-assisted heat treatment system aimed at airborne virus deactivation and hospital air disinfection. Their setup consists of a solar collector, auxiliary electrical heater, a porous unit, a disinfection chamber, and a cooling unit. In the proposed system, microorganisms are first captured by a porous medium, after which electrical heaters, powered by a solar collector, raise the chamber temperature to 105 ℃ for a five-minute exposure period. As a result, the air passing through the porous medium is disinfected and subsequently cooled via a heat exchanger to restore thermal comfort conditions. The system is designed to run continuously, using solar energy to heat the air during the day and switching to electric heaters embedded in the porous medium at night or during transition periods. Their simulation results indicate energy efficiencies of 37.4% and 91.1% for daytime and nighttime operations, respectively. Xi et al. [66] proposed a novel passive solar heating approach for inactivating bioaerosols. In this study, the potential of a Trombe wall, which is typically used for heating and natural ventilation, was investigated for inactivating COVID-19 viruses inside a room measuring $6\,m \times 3\,m \times 3\,m$ in China. In order to calculate the air temperature within the Trombe wall duct, they used an energy balance approach and first-order reaction kinetics were employed to estimate the thermal inactivation rate of viruses. The experimental results demonstrated that the outlet air temperature could reach up to 94.8 ℃, providing an average

thermal efficiency of 45.7 %, and simulated single-pass inactivation efficiency rates were 59.1% for SARS-CoV-2 and 89.3% for SARS-CoV-1 and MERS-CoV. While the proposed disinfected Trombe wall shows strong potential as a passive, solar-driven system for combined heating and virus inactivation, particularly at poorly ventilated or rural houses without mechanical ventilation systems, it requires experimental validation, broader climate testing, and economic assessment. In 2024, Xie. et al. [67] developed a photovoltaic-Trombe wall system including photovoltaic power generation, solar air heating, air filtration, and thermal sterilization to inactivate Klebsiella pneumoniae bacteria. The results showed that disinfection efficiency increased from 15.2% at 45 ℃ to 74.3% at 85 ℃. Simulations for winter in Hefei, China, showed electrical and thermal efficiencies of 13.4% and 21.8%, with outlet air temperatures reaching up to 75 ℃. The system also reduced indoor bacterial concentrations by more than 60%, reducing the time for a 90% drop in bacterial levels from more than three hours to roughly one hour. The design also helped prevent bacterial buildup on filters. Although this system addresses both energy efficiency and indoor air quality, it relies on a single bacterial species and provides no long-term or cost analysis.

Another heat-based disinfection technology is the use of self-heated filters, which are designed to be electrically conductive. In this regard, Yu et al. [68] investigated a novel filter design utilizing heated nickel (Ni) foam for the removal of SARS-CoV-2. Their findings indicated that when the filter temperature approached 200 ℃, nearly 99.8% of the aerosols captured by the filter were inactivated. This technology is particularly suitable for use in closed and confined environments. However, its performance under real HVAC operating conditions and long-term stability under repeated heating cycles are the main limitations of this system. In another study, Ludwig-Begall et al. [69] evaluated the effectiveness of using vaporized hydrogen peroxide (H_2O_2), and dry heat treatment for decontaminating porcine respiratory coronavirus (PRCV) from surgical face masks

and filtering facepiece respirators. In the vaporized (H_2O_2) method, the surgical masks, filtering facepiece respirators, and a chemical indicator were individually sealed in Mylar/Tyvek pouches and sterilized using vaporized hydrogen peroxide (VHP) in the V-PRO Max Sterilizer. This process utilized 59% liquid hydrogen peroxide and involved a 28-minute non-lumen cycle consisting of preparation, sterilization, and ventilation phases. In the dry heat treatment, surgical masks and filtering facepiece respirators were placed horizontally on a metal frame and inserted into an electrically heated chamber, where they were treated at a temperature of 102 ℃ ($\pm$4 ℃) for 60 minutes ($\pm$15 minutes). The results indicated that these technologies significantly reduced the presence of viruses. However, their practical application depends on factors such as scalability, equipment availability, and mask integrity after repeated cycles.

Thermal inactivation solutions have demonstrated strong potential for eliminating a wide range of microorganisms in the literature. However, several challenges limit their broader adoption. The key issues include the need for very high temperatures and long exposure times in designs, energy losses, dependence on certain operating or climate conditions, limited testing against different pathogens, and uncertainties regarding durability and cost-effectiveness in the long run. To address the drawbacks of the existing technologies, alternative approaches can be proposed to achieve disinfection without requiring bulk heating of air or surfaces.

Radiation-based technologies, such as UV and IR, provide non-contact ways to inactivate microbes quickly and can be used as a supplement or even an alternative to heat-based disinfection.

2.4 Radiation-based Disinfection Technologies

Radiation-based disinfection methods are widely used to inactivate pathogens by damaging their cellular structures and genetic material. These technologies are adaptable and effective in various settings, from healthcare to public spaces, with potential for integration into modern disinfection units [70,71].

Among radiation-based technologies, ultraviolet-C (UV-C) irradiation (UV spectrum with wavelengths between 100 and 280 nm**)** has been widely applied for microbial inactivation due to its ability to disrupt the DNA and RNA of pathogens. The performance of this method strongly depends on the intensity of the radiation and the duration of exposure, both of which lead to higher rates of inactivation [72].

To enhance the effectiveness of UV disinfection, researchers have explored combining it with other methods [73]. Mahanta et al. [74] in 2021, conducted experimental research on the effectiveness of combining heat and ultraviolet (UV) radiation to disinfect pathogenic bacteria and the SARS-CoV-2. Their goal was to develop a cost-effective, innovative method for microbial deactivation. In their experiments, they used two 100 W incandescent bulbs and two 11 W UV-C lamps within a small wooden box made from plywood to investigate the optimal temperature and exposure time for disinfection. Their results showed that glycoprotein (used as a model for the SARS-CoV-2 spike protein) and E. coli bacteria (collected from everyday items) were effectively damaged at 70 ℃ with an exposure time of 15 minutes.

Building on this research, Mahanta et al. [75], in 2022, extended their work by investigating the combined use of IR and ultraviolet-C (UV-C) radiation for disinfection. In their experiments, they used a 250 W IR lamp and two 11 W UV-C lamps. Results indicated that the combination of IR

and UV-C radiation was more effective than UV-C radiation with visible light. The optimal temperature in this method was 65.61℃ with an exposure time of 13.52 minutes, both of which were lower than the requirements reported in their 2021 study. This enhanced efficiency is attributed to the superior penetration capability of IR radiation. One potential application of this system is in disinfecting hospital waste prior to disposal, which could reduce the spread of pathogens and improve safety in waste management processes.

More recently, research has shifted toward optimizing UV disinfection for air treatment applications. In 2023, Lim et al. [76] conducted an experimental and numerical study to evaluate the performance of a UV system designed to inactivate bacterial spores in cabin air. The study specifically focused on assessing the system's effectiveness across a range of relative humidity (RH) levels. Results showed that RH significantly influences the disinfection process. For instance, at $RH = 100\ \%$, and UV dose of 20 mJ/cm^2, 99.7% of Bacillus *subtilis spores and be deactivated*, whereas at $RH = 20\ \%$ and with the same dose of UV, inactivation rate increase to 99.94%.

Despite the widespread use of UV technologies for microbial inactivation, they can also cause serious issues, including risks of eye and skin damage and the possibility of structural degradation from repeated use [77] . By contrast, the IR form of radiation, which exists between the visible red light and microwave regions of the electromagnetic spectrum (wavelengths between 0.7 μm and 1 mm), has a strong thermal effect and is safe for use.

Infrared radiation-based technologies have recently emerged as a promising approach for disinfection due to their both health and environmental advantages. For example, IR radiation does not generate harmful byproducts and is already used in therapeutic treatments and considered safe

for human exposure. These characteristics make IR particularly attractive for disinfection processes where minimizing operator hazards and preventing material degradation [78,79].

In 2002, Mata-Portuguez et al. [80] evaluated a prototype infrared sterilizer for disinfecting stainless steel dental instruments which are contaminated with *Bacillus subtilis* spores and compared the IR method with conventional dry heat technology. The results showed that the instruments were completely disinfected at approximately 180 ℃ during 9 minutes, with an energy consumption of about 600 W. They also stated that IR provides significant advantages, including shorter sterilization cycles, reduced power consumption, and the elimination of toxic residues in comparison with dry heat methods. Finally, they concluded that IR radiation can provide rapid, energy-efficient sterilization and an environmentally friendly approach; however, this method was limited to non-heat-sensitive instruments. Similarly, in 2022, Staretu and Voicu [79], proposed an infrared radiant panel system for the sterilization and disinfection of hospital protective equipment. Radiant panels, which operate on electricity, produce infrared radiation that directly heats objects in its path, effectively warming protective equipment without impacting the surrounding air temperature [80]. Consequently, they are highly efficient and convert nearly all consumed electricity into heat, so that each kilowatt of electrical power yields an equivalent amount of thermal energy [79,81]. In their work, they demonstrated the use of radiant panels for disinfecting items such as face masks, gloves, visors, gowns, and various medical utensils. They showed that temperature and exposure time can be adjusted according to characteristics of each item, so that all protective equipment consistently reached the effective disinfection range of 85 ℃ –90 ℃ without causing material damage. For example, for large loads, the system requires approximately 30 minutes to reach 90 ℃, after which a short exposure of 1–5 minutes is sufficient to achieve complete disinfection.

Extending the use of IR radiation beyond instruments and personal Protective Equipment, Karaböce et al. [78] in 2022, investigated its effectiveness for surface disinfection under both open and closed environmental conditions. They set up experiments in both open and closed environments and used scaffolding to position the IR panels at varying heights. Their study showed that virus inactivation was strongly influenced by humidity and airflow. During the experiments, the surface temperature reached up to 44 ℃ . The results demonstrated that at a relative humidity of approximately 50%, and the IR panel positioned at a height of 1.4 meters, after 3 hours of exposure in a closed environment, approximately 90% of the viruses were inactivated. While in open-air conditions, with an airflow rate of 0.20 m/s, and the IR panel placed at a height of 1.0 meters after 10 minutes, the inactivation rate was 45.7%. The reason is that although airflow enhances rapid virus inactivation by accelerating droplet evaporation, convective heat losses limit the maximum disinfection compared to stagnant conditions. The experimental setup of their study is shown in Figure 2.5. To monitor surface temperature, they utilized an IR camera to measure temperature changes induced by the IR panels. In the closed experimental setup, an air nebulizer was employed to regulate humidity in the isolated chamber.

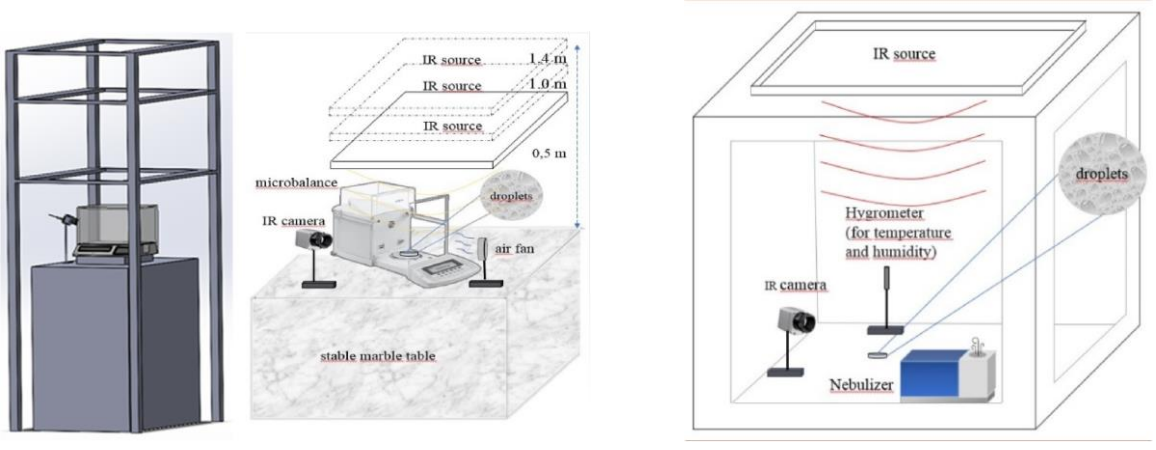

Figure 2.5. Experimental setup used by Karaboke et al. [78] to investigate the use of IR radiation for surface disinfection and virus deactivation.

IR technology has also been applied to filter disinfection to enhance disinfection efficiency. Damit et al. in 2011 [82], investigated the performance and effectiveness of using infrared radiation for air filter disinfection. In this experimental study, two reflector heat lamps (BR40) with power ratings of 125 W and 250 W were used as IR radiation sources. These lamps emitted energy at a maximum wavelength of 1 micron, which lies within the near-infrared range. A HEPA filter with a circular cross-section of 46 mm in diameter was employed in the setup. In order to increase the IR radiation absorption, an activated carbon (AC) fiber mat was incorporated in direct contact with the HEPA filter to enhance the absorption of IR radiation. Heat transfer between the AC mats and the HEPA filter occurred through conduction. The AC mat is known for its high IR absorption properties [83].

The IR lamp was positioned 20 cm from the surface of the fiber mat. To direct the radiation towards the filter, a cylindrical aluminum foil was wrapped around the lamp, and an additional aluminum foil was placed under the fiber mat to redirect the incident ray toward the filter surface. The results showed that if the filter surface temperature reached approximately 200 $°C$, microbes over the filter could be inactivated within 5 seconds. The temperature of the fiber mats was measured using an IR pyrometer, as shown in Figure 2.6.

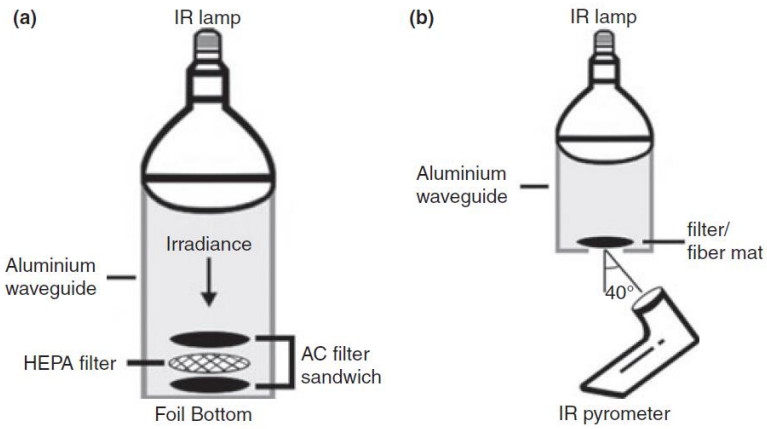

Figure 2.6. Schematic of the (a) experimental setup and (b) Temperature measurement configuration used in the study by Demit et al.[82]

The reviewed literature indicates that existing IR radiation technologies show strong potential for disinfection due to their safety, high energy conversion efficiency, and absence of harmful by-products. IR has been mostly used for the disinfection of medical instruments or decontaminating personal protective equipment and few studies have integrated IR radiation with air filtration [61].

2.5 Novelty and Contributions

It is evident from the reviewed literature that a clear gap exists between existing disinfection technologies and their applicability to HVAC filtration systems. Conventional disinfection methods often involve high operational costs, high energy consumption, complex maintenance requirements, and performance degradation over time. On the other hand, heat-based disinfection technologies offer a strong microbial inactivation capability; however, their widespread implementation is limited by high temperature requirements, long exposure times, and substantial energy losses.

The proposed infrared ceramic heating system offers several advantages over other heat-based disinfection methods, such as embedded heating systems, natural convection methods, and forced convection systems [84], all of which were developed and tested in our research group's laboratory. Unlike embedded heating systems, the current system operates externally, without integrating wires into the filter media; therefore, it is compatible with a wide range of pleated HVAC filters without modification. Also, since there is no direct contact with the filter surface, it reduces the risk of localized overheating and thermal degradation, and its standalone design simplifies maintenance, inspection, and retrofitting.

Compared with natural convection-based systems, the infrared approach provides a more uniform, controlled temperature distribution. Moreover, infrared radiation delivers energy directly to the filter surface without dependence on air movement, so the system reaches disinfection temperatures much faster. In contrast to forced convection systems, the proposed system eliminates the need for high-velocity hot air, avoiding uneven heating, excessive pressure drop, and large temperature gradients. Additionally, it can be easily installed near existing filter units with minimal duct modification and operates more quietly and efficiently due to the absence of large fans.

Similarly, radiation-based approaches such as ultraviolet technologies, despite their proven effectiveness, pose health and environmental issues that limit their use in HVAC systems. Regarding infrared radiation, although it has been widely used for the inactivation of infectious agents in "non-aerosol" applications [78,82], no technologies currently available on the market use infrared heating to inactivate pathogens in the HVAC system.

To address the mentioned research gaps, the present thesis will develop a methodology for the optimal design of an integrated system combining pleated HVAC filters with infrared ceramic

heaters for heat-based disinfection. The main novelty and research contributions of this thesis include:

1. Proposing a novel, low-cost air disinfection approach that combines air filtration with thermal inactivation.
2. Demonstrating reduction of the infection risk through on-filter inactivation of captured microorganisms, contributing to safer and cleaner indoor air.
3. Enhancing energy efficiency by utilizing infrared radiation, which transfers energy directly to the filter surface with minimal losses, as IR propagation is largely unaffected by the air medium between surfaces.
4. Identifying optimal geometric and operational parameters that promote uniform temperature fields and effective disinfection across the filter surface.
5. Establishing a modeling framework combining radiative view-factor analysis and numerical simulation to predict temperature distribution.
6. Evaluating the thermal performance of the proposed system under realistic HVAC conditions, confirming the feasibility of IR-based heat-driven disinfection.

Chapter 3. Experimental Methodology & Setup

3.1 Preface

Experiments are a primary part of this thesis, providing data to assess temperature profiles across the filter surface and to determine the effectiveness of radiative thermal disinfection as well as to evaluate how a controlled radiant heat source influences temperature distribution across different filter configurations and materials. For accurate interpretation of the results, temperatures were recorded at several points on the filter surface as well as within the test unit. Overall, these experiments were designed to capture the practical aspects of radiative heat-based disinfection.

3.2 Experimental Setup Description

The experiments were designed to measure temperature distribution over a pleated filter exposed to radiant heat transfer and to record the corresponding electrical energy consumption.

The experimental setup consists of a rectangular test unit with a cross-section of $65\ \text{cm} \times 32\ \text{cm}$ and a length of $120\ \text{cm}$. The unit is constructed from solid polycarbonate sheets with a thickness of 6 mm. To improve both structural strength and thermal insulation, twin-wall polycarbonate of the same thickness (6 mm) is used for the internal walls and to enhance stability of the unit the bottom side is strengthened with 2 cm thick wood. In addition, the interior surfaces of the unit are lined with aluminum foil to improve reflection and minimize heat losses.

In addition to the test unit itself, the experimental setup for this study includes the following components and instruments: pleated filter, including regular MERV-11 and carbon-coated MERV-8, a ceramic heater as the radiant heat source, a PID (Proportional–Integral–Derivative) controller, Type-T thermocouples, and data loggers. In the following the detailed of each part are describe.

The completed setup, which includes the experimental equipment, can be seen in Figure 3.1a and 3.1b.

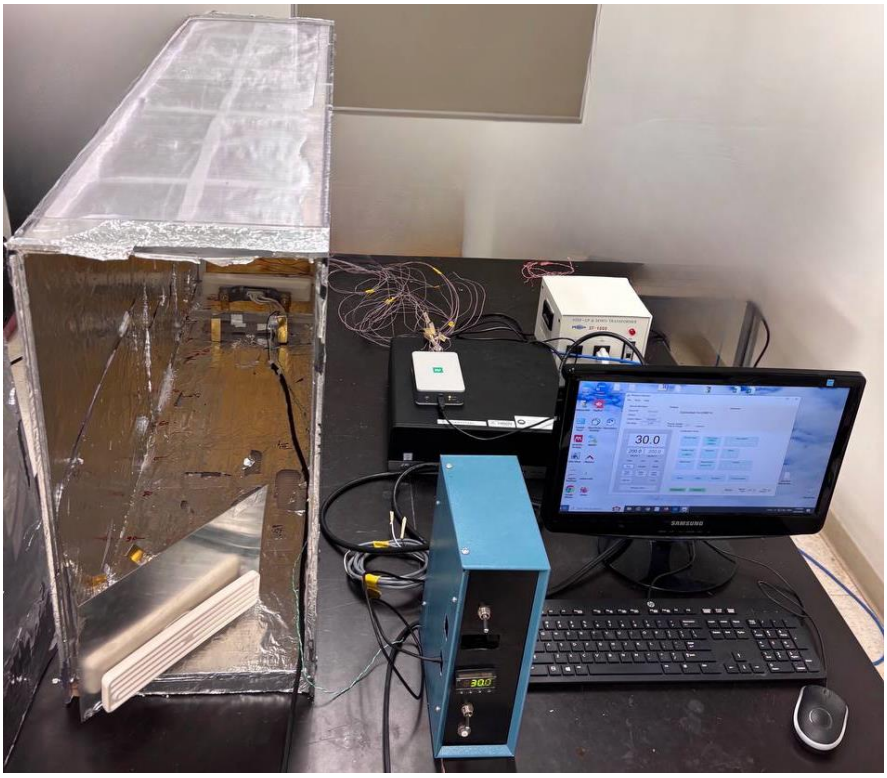

(a)

(b)

Figure 3.1. (a) Experimental setup and associated equipment; (b) interior view of the unit showing the pleated filter.

The primary heat source in the experimental setup was a ceramic infrared panel radiator. Its role was to provide stable radiant heating to the pleated filter surface (Figure 3.2). The technical specifications of the ceramic heater device are listed below:

- Type: HTS/1 flat ceramic infrared radiator
- Power rating: 200 W
- Operating voltage: 230 V
- Dimensions: $245 \times 60 \times 30\ mm$ (length × width × height)

- Maximum permissible surface temperature: up to 860 ℃, with a typical operating range of 450–700 ℃
- Radiant wavelength range: 2–10 μm

The HTS/1 radiator is manufactured using a hollow-casting ceramic process with internal insulation, which enhances radiant efficiency while minimizing heat loss to the backside [85]. Also, a key feature of this model is the built-in Type-K thermocouple, integrated into the ceramic body, which provides direct surface temperature measurement and feedback during operation.

The ceramic heater was placed directly facing the pleated filter within the polycarbonate unit (see Figure 3.3), with an aluminum reflector mounted behind it to enhance forward radiation and reduce heat losses to the enclosure.

The heater was mounted on the polycarbonate gate, which was lined with aluminum foil to enhance thermal shielding and minimize heat losses. This configuration directed most of the radiant energy toward the filter surface, ensuring uniform and repeatable heating throughout all experiments.

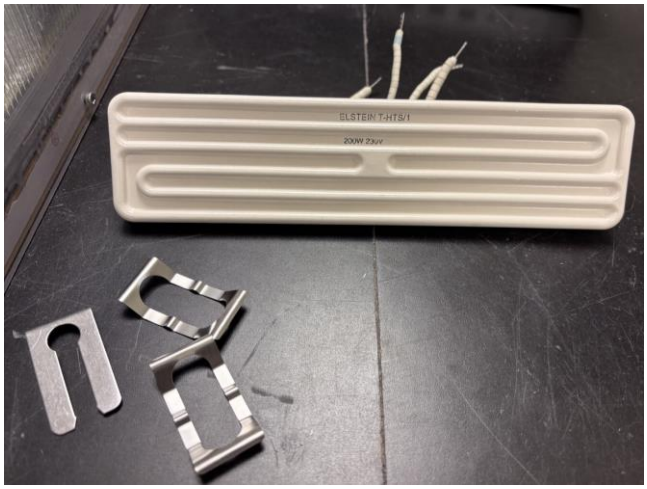

(a)

(b)

(c)

Figure 3.2. Views of the ceramic heater device, including (a) the front surface with mounting clips, (b) rear electrical connections, and (c) side view showing the heater thickness.

Figure 3.3. Ceramic heater setup with an aluminum reflector mounted on the gate to intensify forward radiation and reduce heat dissipation.

Two types of commercial polyester pleated HVAC filters were employed in this study: a regular MERV-11 filter and a carbon-coated MERV-8 filter with dimensions of $12 \times 24\ in$ (Figure 3.4a and 3.4b). These were selected to represent typical filtration media used in ventilation systems and to evaluate how surface treatments influence heating and disinfection performance. The filters were set up vertically inside the unit, facing the ceramic heater. To monitor the surface temperature distribution throughout the heating cycles, fifteen T-type thermocouples (OMEGA) with a diameter of 0.08 mm and accuracy of ± 0.5 ℃ were attached to the pleats of the filter.

Since the laboratory power supply operated at 110 V and the ceramic heater required 220 V, a step-up &down transformer was used to convert the input voltage from 110 V to 220 V. The output of the transformer was then connected to a power meter (Poniie-PN2000), which enabled real-time measurement of the electrical consumption during each experiment (Figure 3.5a and 3.5b).

(a) (b)

Figure 3.4. Views of (a) regularMERV-11 filter and (b) carbon-coated MERV- 8 filter.

(a) (b)

Figure 3.5. (a) Step-up ad down transformer used to convert the 110 V laboratory supply to 220 V for powering the ceramic heater; (b) power meter connected in the circuit to monitor real-time electrical consumption during the experiments.

A PID temperature controller (OMEGA-CN32PT-145) was used to manage the ceramic heater's surface temperature (Figure 3.6). It worked by adjusting the electrical power sent to the heater based on the feedback signal, allowing the heater to quickly reach and reliably hold the target temperature during the experiments.

The PID controller was powered through the connection of the transformer and the power meter. Then the ceramic heater was connected directly to the PID, with two terminals for the 220 V supply and two for the built-in Type-K thermocouple.

During operation, the PID compared the measured temperature with the chosen setpoint and adjusted the electrical power delivered to the heater as needed. By rapidly modulating the supplied power, the controller reduced fluctuations, prevented overshoot, and kept the heater at a steady operating temperature.

This closed-loop control enabled the ceramic heater to rapidly reach and accurately maintain the target temperature required for disinfection. At the same time, the power meter provided a direct measurement of the electrical energy consumed, ensuring that both thermal and energy performance were consistently monitored.

Figure 3.6. PID temperature controller used in the experimental setup.

A sixteen-channel data logger (NI-9213) was used to record the temperature distribution throughout the experimental unit. A total of nine thermocouples were mounted on the front face of the pleated filter, and five thermocouples were placed on the back side of the filter to capture the surface temperature distribution. The final thermocouple was positioned on the polycarbonate gate, at the location where the ceramic heater was mounted, to track background and reflective heating effects.

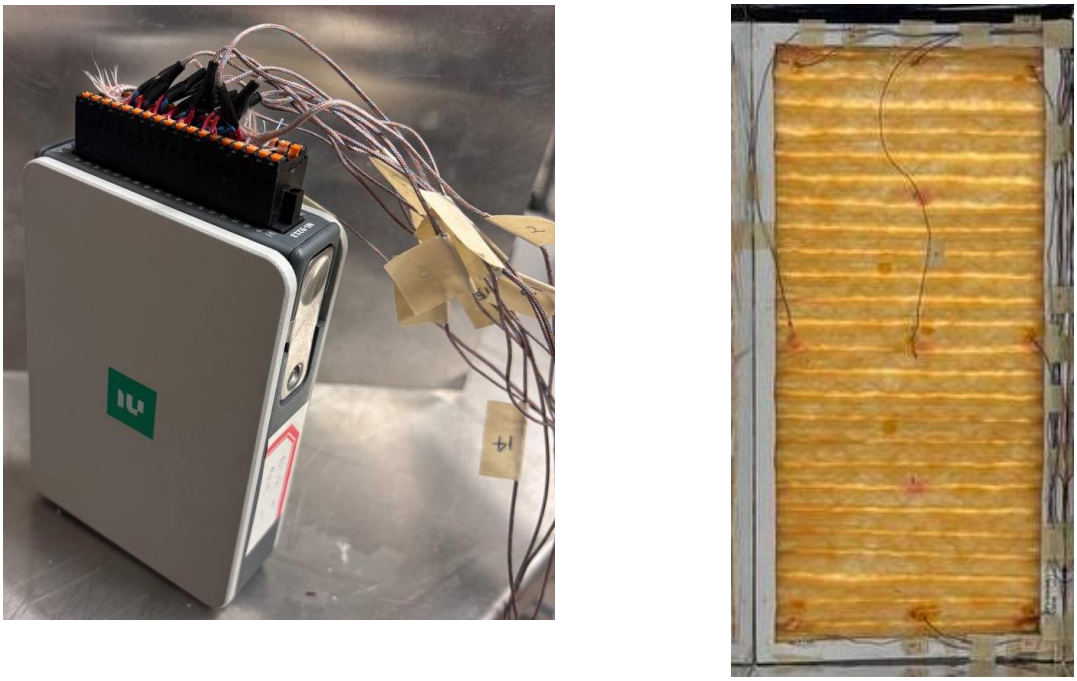

(a) (b)

Figure 3.7. (a) Data logger with connected thermocouples, (b) placement of thermocouples on the front face of the pleated filter.

3.3 Experimental Cases

To investigate the performance of using ceramic heaters for disinfecting pleated HVAC filters, a series of experiments was designed and conducted under varying configurations. Table 3.1 summarizes the key operating parameters and geometrical conditions used in the experiments.

Table 3.1. Summary of key parameters used in the experiments

Parameters	Symbol/Unit	Range / Value	Description
Heater–Filter Distance	D (cm)	10-100	Center-to-center spacing between heater and filter
Heater Tilt Angle	α (°)	0, 10, 20	Inclination of the ceramic heater relative to vertical
Heater Set-Point Temperature	$T_{setpoint}$ (℃)	180-350	Controlled at ceramic surface (PID sensed point)
Filter Type	-	MERV 8 & 11	Pleated HVAC filter (Regular and Carbon-coated)

Each case targeted a specific parameter and purpose to isolate their influences on temperature distribution and heating uniformity. Before starting each test, the experimental unit was set up with the ceramic heater(s) and pleated HVAC filter arranged at the required distance and tilt angle for that configuration. The thermocouples were connected to the data logger, and the system was left to stabilize at room temperature (22 ℃) before switching on the heater.

The ceramic heater setpoint temperature was then adjusted using the PID controller to the desired temperature. The temperature distribution across the filter surface is continuously recorded at a sampling interval of 0.1 seconds. Each run was continued until the filter surface reached the target disinfection temperature of 65 ℃. Then the tests were run for an additional 10 minutes to ensure the filter is disinfected. Between tests, the unit was allowed to cool back to ambient conditions to minimize any carry-over effects from the previous run. The investigations were grouped into four categories:

Group I: Experiments conducted in a fully aluminum-foil-covered unit with a single ceramic heater. These tests examined the influence of heater-to-filter distance, heater tilt angle, heater setpoint temperature, and filter materials (regular versus carbon-coated) on the temperature distribution across the filter surface.

Group II: Experiments using one or two ceramic heaters in units where the gates were not covered with aluminum foil, to study the combined effect of heater quantity and boundary conditions.

Group III: Targeted experiments conducted under specific conditions to allow comparison with analytical calculations. The aim was to predict the experimental data with analytical results.

Group IV: Experiments carried out under selected conditions to provide a direct basis for comparison with numerical simulations.

3.4 Uncertainty Analysis

Doing uncertainty analysis is an important part of every experimental study, as the uncertainty of the equipment used for measurements can accumulate and affect the experimental results. The primary source of uncertainty in the current experiments arises from the temperature measurements. The uncertainty associated with temperature measurements was evaluated in accordance with the Ref. [86], considering both Type A and Type B components. Type A uncertainty represents random variations obtained from repeated measurements, while Type B uncertainty accounts for systematic effects related to sensor calibration, data logger accuracy, and resolution.

The average filter temperature ($\bar{T}$), standard deviation (s), and standard uncertainty of the mean (u) were calculated sequentially using the following equations:

$$\bar{T} = \frac{\sum_{i=1}^{n} T_i}{n} \tag{3.1}$$

$$s = \sqrt{\frac{\sum_{i=1}^{n} (T_i - \bar{T})^2}{n-1}} \tag{3.2}$$

$$u = \frac{s}{\sqrt{n}} \tag{3.3}$$

where T_i represents the individual readings, and n is the number of measurements. For n = 5, the maximum standard uncertainty throughout the 25-minute experiment durations was calculated as $u = 0.43$ ℃.

Type B uncertainties were estimated from manufacturer specifications and calibration certificates, including thermocouple calibration, data-logger accuracy, and data-logger resolution.

The corresponding probability distributions, divisors, and standard uncertainties for each component are summarized in Table 3.2.

Table 3.2 Spreadsheet model showing the uncertainty budget

Source of uncertainty	**Value** (℃)	**Probability distribution**	**Divisor**	**Standard uncertainty** (℃)
Thermocouple calibration uncertainty	0.5	Normal	2	0.25
Data logger uncertainty	0.25	Normal	2	0.125
Data logger resolution	0.001	Rectangular	$\sqrt{3}$	0.0006
Standard uncertainty of mean of 5 repeated readings	0.43	Normal	1	0.43
Combined standard uncertainty	-	Assumed normal	-	0.51
Expanded uncertainty	-	Assumed normal (k=2.58)	-	1.32

The Divisor represents the factor used to convert a specified tolerance or uncertainty range (e.g., ± value) into a standard uncertainty (1 s) based on the assumed probability distribution. For a normal distribution, the divisor is 2, while for a rectangular (uniform) distribution, it is $\sqrt{3}$, as recommended by Bell (2001) [86].

The combined standard uncertainty was obtained as [86];

$$u_c = \sqrt{\sum u_j^2} \qquad 3.4$$

which resulted in $u_c = 0.51$ ℃. The expanded uncertainty, representing the range within which the true temperature value is expected to lie with approximately 99 % confidence, was calculated as [86],

$$U = k\, u_c \tag{3.5}$$

where $k = 2.58$ is the coverage factor corresponding to a 99 % confidence level. Thus, the expanded uncertainty for all temperature measurements was $U = 1.02$ ℃.

Accordingly, each measured temperature can be reported as:

$$T = \bar{T} \pm 1.32\ ℃ \tag{3.6}$$

which means the true value of temperature is expected to fall within $\pm$ 1.32 ℃ of the measured mean value with 99 % confidence. This expanded uncertainty should been consistently applied in all reported temperature values, tables, and figures throughout this thesis.

3.5 Chapter summary

This chapter presented the experimental setup and methodology used to evaluate radiative heat-based disinfection of pleated HVAC filters. The detailed of the construction of the test unit, the instruments used, and the testing conditions to measure temperature distribution, energy consumption, and heating uniformity across different filter types and configurations was provided. In addition, this chapter included the uncertainty analysis conducted to assess the reliability and accuracy of the experimental measurements.

Chapter 4. Radiative Heat Transfer Analysis and Numerical Simulation

4.1 preface

This chapter applies the fundamental principles of radiative heat transfer and numerical simulation to analyze the thermal behavior of the proposed system. The first part outlines the theoretical basis for radiation exchange between surface to emphasize the role of view factors in determining geometric relationships that influence heat transfer. The subsequent numerical analysis employs these principles to simulate the temperature distribution within the enclosure. This combined theoretical and computational approach provides a foundation for interpreting experimental observations and understanding the dominant heat transfer mechanisms in the system.

4.2 Radiation Exchange: Fundamentals to Two-Surface Enclosures

In analyzing radiative heat transfer within an enclosure, it is first necessary to consider the basic principles of radiation exchange together with the geometric aspects that govern the transfer, commonly referred to as view factors.

According to Incropera and DeWitt's Fundamentals of Heat and Mass Transfer [87], the net exchange of radiation at surface i can be expressed in terms of the radiosity (J), the irradiation (G), and the surface blackbody emissive power (E_b). This general framework provides the basis for later emphasizing the role of view factors in quantifying the interaction between different surfaces.

$$q_i = A_i(J_i - G_i) \tag{4.1}$$

And the radiosity which is defined as the total energy leaving a surface (emission plus reflection), is expressed as [87]:

$$J_i = E_i + \rho_i G_i \tag{4.2}$$

In Eq. (4.2), ρ_i denotes the surface reflectivity. The net radiative transfer from the surface may also be expressed in terms of the surface emissive power and the absorbed irradiation [87]:

$$q_i = A_i(E_i - \alpha_i G_i). \tag{4.3}$$

where α_i is the absorptivity of the surface, and for an opaque surface $a_i = 1 - \rho_i$. According to Kirchhoff's law of thermal radiation, for a surface in thermal equilibrium, the emissivity equals the absorptivity, i.e., $\varepsilon_i = a_i$ [87].

Using the definition $\varepsilon_i = \frac{E_i}{E_{bi}}$, for opaque, diffuse–gray surfaces, the radiosity can be related to the blackbody emissive power (E_{bi}) , as follows [87]:

$$J_i = \varepsilon_i E_{bi} + (1 - \varepsilon_i) G_i \tag{4.4}$$

And equivalently [87];

$$q_i = \frac{E_{bi} - J_i}{(1 - \varepsilon_i)/\varepsilon_i A_i} \tag{4.5}$$

This form of radiative transfer, illustrated by the network element in Figure 4.1, is driven by the potential difference $(E_{bi} - J_i)$ and is characterized by a surface radiative resistance expressed as $(1 - \varepsilon_i)/\varepsilon_i A_i$.

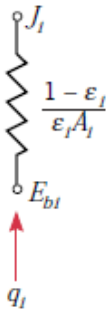

Figure 4.1. Network element representing the net radiation transfer from a surface.

In radiative heat transfer analysis, the view factor is a key parameter that quantifies the geometric relationship between two surfaces. It represents the fraction of radiation leaving one surface that directly reaches another, independent of surface temperatures or emissivity's [87]. Accurate evaluation of view factors is particularly important for modeling heat transfer in enclosures with complex geometries, such as filter–heater systems. The reason is that it directly affects the prediction of temperature distribution and thermal performance.

The following section presents the governing equations and methodologies for calculating the view factors relevant to this study, providing the foundation for linking experimental observations with theoretical predictions.

4.2.1 Governing Equations for View Factor Determination

The calculation of view factors is grounded in the fundamental principles of radiative heat exchange between surfaces. The view factor, F_{1-2} represents the proportion of radiation leaving surface 1 that is incident directly on surface 2. Its evaluation depends solely on geometry and orientation, and it satisfies both reciprocity and summation rules [87].

The radiative exchange between the heater surface (1) and the filter surface (2) can be quantified using the concept of view factors. For two differential surface elements dA_1 and dA_2, separated by a distance R, the view factor is defined as:

$$F_{1-2} = \frac{1}{A_1}\int_{A_1}\int_{A_2}\frac{\cos\varphi_1 \cos\varphi_2}{\pi R^2} dA_2 dA_1 \quad 4.6$$

where φ_1 and φ_2 are the angles between the surface normal and the line joining the two differential areas.

In this study, the following assumptions are applied:

1. Both the absorber (filter) and heater surfaces are diffuse and gray.
2. The intervening medium (i.e., air in this study) is nonparticipating, meaning it does not absorb, scatter, or emit thermal radiation.
3. Radiation exchange is modeled using the radiation network analogy, where the net heat flux between surfaces is determined from the balance of emitted, reflected, and absorbed radiation.

The exchange of thermal radiation between two diffuse–gray surfaces separated by a nonparticipating medium can be conveniently represented by a network analogy [87]. In this approach, each surface is treated as a radiosity node that exchanges radiation with the other surfaces, as introduced in section 4.1. The analogy resembles an electrical circuit, where the blackbody emissive power ($E_{bi} = \sigma T_i^4$) provides the driving potential, and the surface and geometric properties of the enclosure appear as resistances.

Using the network representation which is illustrated in Figure 4.2, the radiation exchange between two surfaces can be expressed as:

$$q_{1-2} = q_1 = -q_2 = \frac{\sigma\left({T_1}^4 - {T_2}^4\right)}{\frac{1-\varepsilon_1}{\varepsilon_1 A_1} + \frac{1}{A_2 F_{2-1}} + \frac{1-\varepsilon_2}{\varepsilon_2 A_2}} \quad 4.7$$

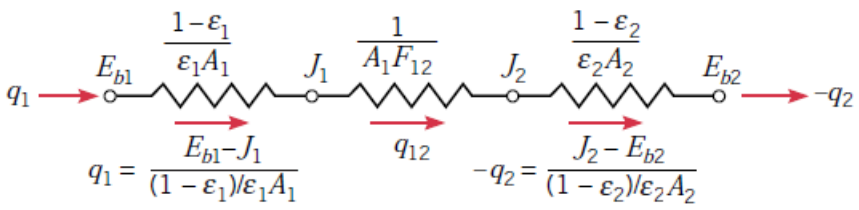

Figure 4.2. Radiation network analogy for two-surface exchange [87].

q_1 is the net rate of radiation leaving surface 1, which must be equal to the net rate of radiation received by surface 2 (q_2). Both terms are therefore equivalent to the net rate of radiative exchange between the two surfaces, denoted as q_{1-2}, since the enclosure considered here involves only two surfaces.

In the present study, several surface pairs may participate in radiative exchange, including heater–filter, heater–wall, and wall–filter interactions. However, in the present calculations, only the radiation exchange between the heaters and the filter is considered, as this interaction represents the dominant exchange mechanism and provides a reasonable simplification for the scope of the analysis.

4.2.2 Application of Shape Factor Equations to the Filter Subsections

To investigate the effect of radiation on different regions of the filter surface, the filter was divided into three subsections: bottom, middle, and top. This subdivision enables a direct comparison between the temperature distribution obtained experimentally and the corresponding view factors of the heater to each subsection, as illustrated in Figure 4.3.

For the calculation of view factors from the heater to each subsection, the shape factor equations for plane rectangular surfaces developed by Gross.et.al. [88] were employed. Their method provides analytical and semi-analytical formulations for evaluating view factors between rectangular surfaces of arbitrary position and size with parallel boundaries. They aimed to offer

practical equations for calculating shape factors in engineering problems, for example, in solar receivers or enclosures subdivided into many surface elements [88]. This approach is particularly suitable for the present configuration, as it avoids the complexity of shape-factor algebra and allows efficient computation of view factors for the three defined filter subsections.

Accordingly, the heater was treated as one surface and each filter subsection as a separate rectangular surface. The view factor between the heater and each subsection was then calculated using the Gross et al. [88] formulations. These values were subsequently compared with the experimentally measured temperature rise across the bottom, middle, and top regions of the filter.

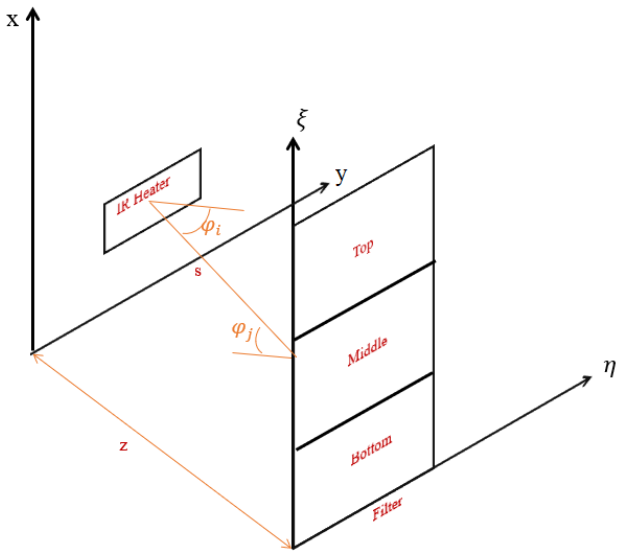

Figure 4.3. The schematic of the heater–filter arrangement used in the view factor analysis. The filter is divided into three subsections (bottom, middle, and top), and the infrared heater is represented as a rectangular surface.

The view factor of the heater to the filter's subsections when the heater and the filter are at an arbitrary angle of α is calculated by [88]:

$$A_h F_{h-f} = -\frac{\sin^2\alpha(\eta-y)}{2\pi}\int_\xi \left[\frac{\cos\alpha(x-\xi\cos\alpha)-\xi\sin^2\alpha}{\sin^2\alpha(x^2-2x\xi\cos\alpha+\xi^2)^{1/2}}\tan^{-1}\left[\frac{\eta-y}{(x^2-2x\xi\cos\alpha+\xi^2)^{1/2}}\right] + \right.$$

$$\frac{\cos\alpha}{\sin^2\alpha(\eta-y)}\left[[\xi^2\sin^2\alpha+(\eta-y)^2]^{1/2}\tan^{-1}\left[\frac{x-\xi\cos\alpha}{[\xi^2\sin^2\alpha+(\eta-y)^2]^{1/2}}\right]-\xi\sin\alpha\ \tan^{-1}\left[\frac{x-\xi\cos\alpha}{\sin\alpha}\right]\right]+$$

$$\left.\frac{\xi}{2(\eta-y)}\ln\left[\frac{x^2-2x\xi\cos\alpha+\xi^2+(\eta-y)^2}{x^2-2x\xi\cos\alpha+\xi^2}\right]\right]\ d\xi \qquad 4.8$$

And when the heater and filter are positioned parallel (i.e., $\alpha = 0\,°$, the view factor is calculated from [88]:

$$A_h F_{h-f} = \frac{1}{2\pi}\left[(\xi-x)(z^2+(\eta-y)^2)^{1/2}\,tan^{-1}\left(\frac{\xi-x}{(z^2+(\eta-y)^2)^{1/2}}\right)\right]-(\eta-y)z\ tan^{-1}\left(\frac{(\eta-y)}{z}\right)+$$

$$[z^2+(\xi-x)^2]^{1/2}(\eta-y)\,tan^{-1}\left[\frac{\eta-y}{[z^2+(\xi-x)^2]^{1/2}}\right]+\frac{1}{2}(\xi-x)^2\ln\left[\frac{z^2+(\eta-y)^2+(\xi-x)^2}{(\xi-x)^2}\right]+\frac{1}{2}z^2\ln[z^2+$$

$$(\eta-y)^2]-\frac{1}{2}\ [(z^2+(\xi-x)^2)]\ ln[z^2+(\eta-y)^2+(\xi-x)^2] \qquad 4.9$$

Figure 4.4 illustrates the relative position of the two surfaces considered in the view factor calculations, namely the heater and the filter.

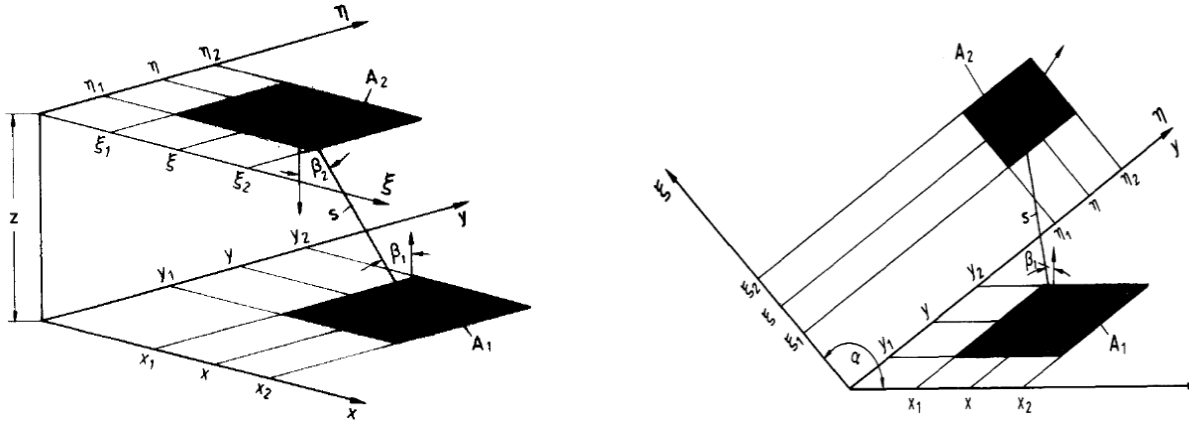

Figure 4.4. Geometric configuration of (a) two parallel rectangular surfaces and (b) two surfaces in planes inclined at an arbitrary angle α. (adapted from Ref. [88]).

As seen in equation 4.8, the expression is too complicated to be solved analytically, equation 4.9 was employed for the calculations of two parallel surfaces. For the case of two surfaces lying in planes inclined at an arbitrary angle α, either equation 4.6 or 4.8 can be used.

Therefore, to calculate the view factors between the heater and the filter under tilted and offset positions, a numerical double-area integration was employed. Since no simple analytical solution exists for the geometry under investigation, the configuration factor integral was solved using a discretization (panel method) implemented in MATLAB (Appendix A). In this approach, both surfaces are subdivided into a large number of differential elements. For each pair of elements, the fundamental relation of radiative exchange was applied, and the contributions were numerically integrated to obtain the total view factor. To verify the accuracy of the implementation, the code was also applied to the case of two identical and parallel surfaces. The results were compared with the reference Figure 4.5 from Incropera [87] , as well as with the analytical solutions presented by Gross et al. [88] for parallel rectangular surfaces (Eq. 4.9).

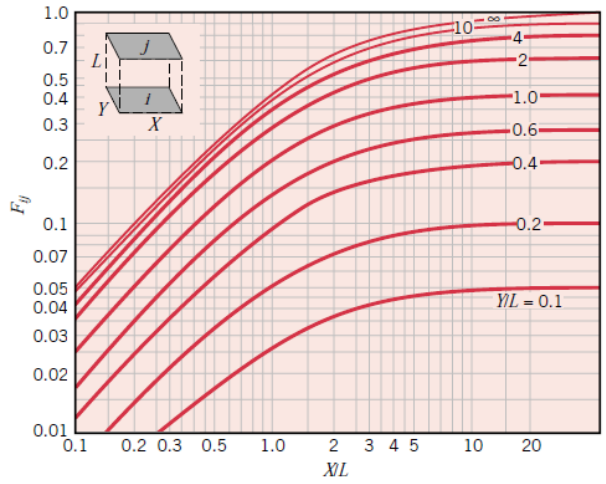

Figure 4.5. View factors between two equal, parallel, and directly opposed rectangular surfaces as a function of normalized dimensions X/L and Y/L. (Adapted from Ref. [87]).

The comparison of the experimental results with the calculated view factors is provided in chapter 5, section 5.6.

4.3 Numerical Analysis of Heat Distribution

A numerical study was performed to demonstrate that, even with certain simplifications and assumptions, the model can effectively reproduce the main temperature patterns observed in the experiments. The analysis focuses on evaluating the influence of parameters such as thermal conductivity, and heater orientation. The simulations offered useful insight into how these factors affect the temperature distribution across the filter.

The numerical model is created based on the following assumptions:

- Air and filter properties are constant and isotropic. Air properties were assumed constant because the temperature variation in the computational domain was not large enough to cause significant property changes. Moreover, as radiation dominated the heat transfer during the short comparison period, the effect of temperature-dependent air properties was negligible.
- The filter is simplified as a thin and flat solid plate rather than a pleated medium. This simplification was necessary because pleat-level modelling would require extensive computational resources and detailed material characterization.
- The ceramic heater surface temperature is considered constant.
- Only radiation heat transfer is considered and natural convection effects are neglected. This assumption allowed the analysis to focus on radiation-driven interactions between the heater and the filter. As will be thoroughly discussed in Chapter 5, radiation dominates the heat transfer process during the very early stage of heating. Therefore, Since the objective of the numerical study was to reproduce the temperature behavior of the filter and compare it with

experimental results, the simulations were limited to the during which radiation is the prevailing mode of heat transfer.

In addition, the small temperature difference between the enclosure walls and the surrounding room minimized the potential contribution of wall-driven convection. At the same time, the convective heat transfer coefficient at room conditions is relatively low [87]. Together, these considerations justified neglecting natural convection in the numerical model.

- Radiation is modeled using the Surface-to-Surface (S2S) radiation model. This model is appropriate for enclosures where radiation is the prevailing mode of heat transfer, and it has been successfully applied in similar studies reported in the literature [89].
- The walls, ceramic heater, and the filter (i.e., all the surfaces) are assumed to be gray and diffuse, and their emissivity is precisely equal to their absorptivity.

In the following sections, the details related to governing equations, boundary conditions, numerical grid, and solver settings will be discussed.

4.3.1 Governing Equations

The first governing equation is the conservation of energy. Under the assumptions adopted in this study, it reduces to the unsteady heat conduction equation.

$$\rho_s C_{p,s} \frac{\partial T}{\partial t} = \nabla . (k_s \nabla T) \tag{4.10}$$

where ρ is the density, C_p is the specific heat capacity, and k is the thermal conductivity of the filter medium, and subscript s denotes solid properties.

In this formulation, radiation does not appear as a volumetric source term; instead, it is introduced through boundary conditions applied at the surfaces.

In this study, the air between the heater and the filter was assumed to be a non-participating medium, meaning that it does not absorb, emit, or scatter radiation and the S2S model was used.

4.3.2 Surface-to-Surface (S2S) Radiation Model

ANSYS Fluent's S2S radiation model is based on the assumption that surfaces behave as gray and diffuse. For a gray surface, the emissivity is independent of wavelength, and by Kirchhoff's law, the emissivity is equal to the absorptivity ($\varepsilon = \alpha$). For diffuse surfaces, the reflectivity is independent of the direction of the incident or emitted radiation [90].

In this framework, the exchange of radiative energy occurs only between surfaces and is unaffected by the transparent medium that separates them. According to the gray-body model, when a radiative flux (G) is incident on a surface, a fraction is reflected (ρG), a fraction is absorbed (αG), and a fraction is transmitted (τG). Since surfaces in most engineering applications, including the present case, are opaque to thermal radiation in the infrared spectrum, transmissivity can be neglected, so $\tau = 0$ [87,91,92].

Applying conservation of energy gives $\alpha + \rho = 1$. Substituting $\alpha = \varepsilon$, it follows that $\rho = 1 - \varepsilon$. This model calculates the radiative heat flux leaving a surface as the sum of the directly emitted energy and the portion of the incident radiation reflected from other surfaces. The energy leaving from surface k expressed as [93]:

$$q_{out,k}^{rad} = \varepsilon_k \sigma \mathrm{T}_k^4 + \rho_k q_{in,k} \qquad 4.11$$

Where $q_{out,k}$ is the energy flux leaving the surface k ,ε_k is the emissivity, σ is the Stefan-Boltzmann constant, and $q_{in,k}$ is the energy flux incident on the surface from the surroundings [93].

Incident energy flux $q_{in,k}$ can be expressed as:

$$A_k q_{in,k} = \sum_{j=1}^{N} A_j q_{out,j} F_{jk} \quad 4.12$$

Where A_k is the area of surface k and F_{jk} is the view factor between surface k and surface j.

For N surfaces:

$$A_j F_{jk} = A_k F_{kj} \; For \; j = 1, 2, 3, \dots, N \quad 4.13$$

So that;

$$q_{in,k} = \sum_{j=1}^{N} F_{kj} q_{out,j} \quad 4.14$$

Therefore, the net radiative heat flux leaving surface k is expressed as:

$$q_{out,k} = \varepsilon_k \sigma \mathrm{T}_k^4 + (1 - \varepsilon_k) \sum_{j=1}^{N} F_{kj} q_{out,j} \quad 4.15$$

Equation 4.15 can also be written in terms of radiosity. In this form, the equation becomes

$$J_k = E_k + \rho_k \sum_{j=1}^{N} F_{kj} J_j \quad 4.16$$

The term $E_k = \varepsilon_k \sigma \mathrm{T}_k^4$ represents the emissive power of surface k, i.e., the energy it emits due to its own temperature. The term $\rho_k \sum_{j=1}^{N} F_{kj} J_j$ accounts for the reflected radiation received from all other surfaces.

This system of coupled surface energy balances is solved simultaneously for all surfaces, and the resulting net radiative fluxes are imposed as boundary conditions in the conduction equation. In other words, radiation enters the analysis only through surface boundary conditions. The S2S

model provides the net radiative heat flux $q_{out,k}^{rad}$ at each wall, which is then applied to the solid energy equation, while the air is treated as a non-participating medium with no volumetric radiation source.

4.3.3 Model Schematic and Boundary Conditions

Figures 5.1a and 5.1b illustrate the schematic of the numerical model developed for this study. The computational domain consists of three main components: a thin solid filter, a ceramic heater, and the main enclosure. The filter has dimensions of $30.5\ \text{cm} \times 61\ \text{cm}$ ($12\ \text{in} \times 24\ \text{in}$) with a thickness of 0.5 mm. The ceramic heater measures $24.5\ \text{cm} \times 6\ \text{cm}$ with a thickness of 30 mm, while the main unit has dimensions identical to the filter section ($30.5\ \text{cm} \times 61\ \text{cm}$) and a thickness of 12 mm.

The equivalent thickness of the filter in the simulation was calculated based on the actual properties of the filter used in the experiments. For this, the experimental pleated filter was first weighed ($m \cong 130\ g$), and using its measured mass along with the known surface area ($A = 12 \times 24\ inches$) the corresponding volume was estimated. The density of the polyester fibres, as reported in the literature [94] ($\rho = 1390\ kg/m^3$), was used in this calculation to ensure that the simulated filter preserved the same material characteristics as the actual one. Therefore, the equivalent thickness was calculated using $t = \frac{m}{\rho \times A}$, resulting in a value of approximately 0.5mm.

The boundary conditions used for this simulation are as follows:

- Constant temperature (T_h) at the ceramic heater surface.
- Zero heat flux on the outer walls, (top, bottom, left, right).

- Radiative exchange at the front and back walls (unit gates), both covered with aluminum foil.
- All the internal walls covered with aluminum foil, treated as radiative surfaces.
- The filter is a solid conduction domain. At its exposed surface, the normal conductive heat flux is balanced by the net radiative flux obtained from the S2S radiation model:

$$-k_f \frac{\partial T}{\partial n} = q_{out,k}^{rad} \qquad 4.17$$

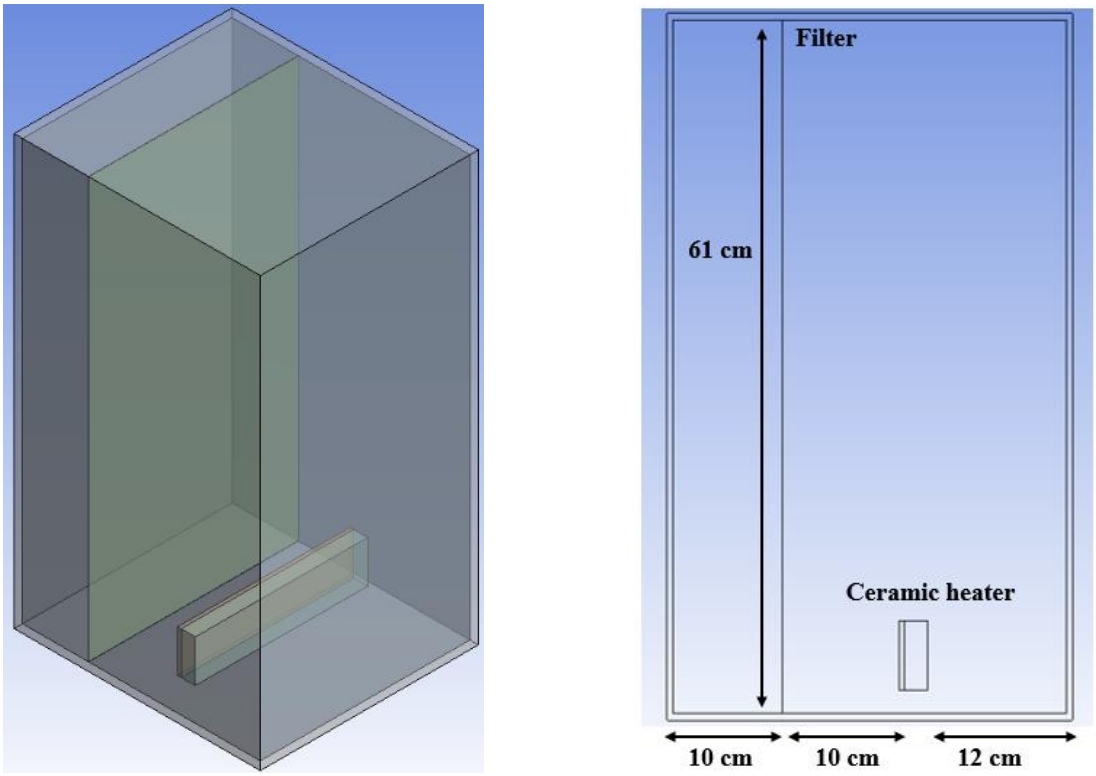

(a) (b)

Figure 4.6. The schematic of the numerical model: a) Complete domain,

4.3.4 Numerical Grid

The computational domain was discretized using a structured mesh generated in ANSYS Meshing. To improve the accuracy of the results near the heater surface and the filter face, a finer mesh was

applied. In addition, the blocking approach was implemented during grid generation to maintain a structured mesh throughout the domain, and mesh growth ratios were introduced to gradually increase cell size away from critical regions to reduce the total number of elements. The total number of elements in the final grid was approximately 7 million cells (Figure 5.2). To better capture the heat transfer, the mesh was refined near the filter and ceramic heater, while larger elements were used farther away to save computation time. The element size around the filter was about 0.16 mm, and for the ceramic heater, it was 0.5 mm.

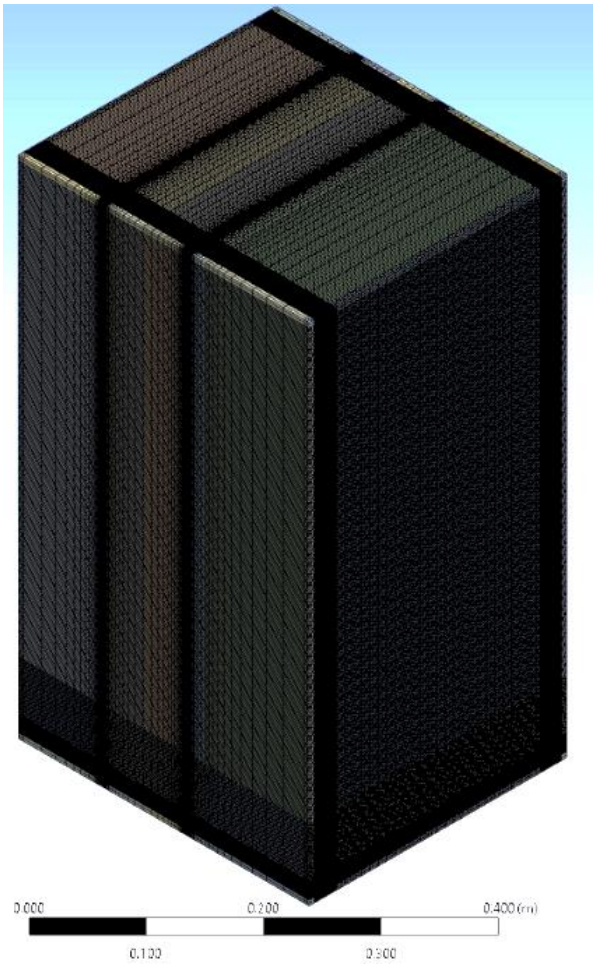

(a)

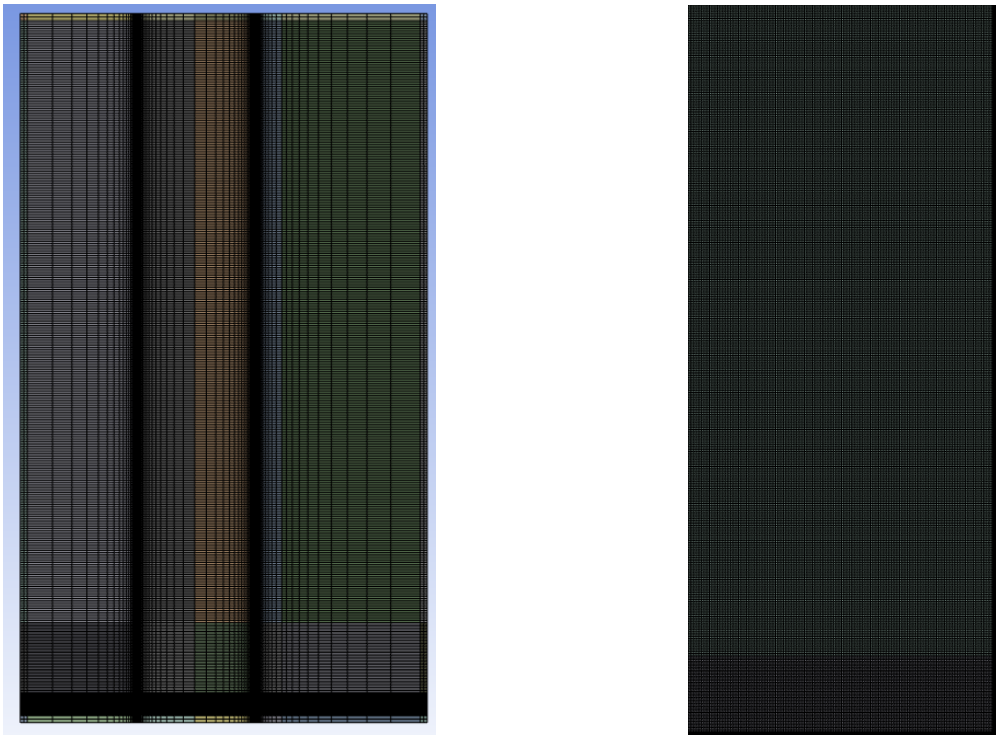

(b) (c)

Figure 4.7. Numerical grid: (a) full computational domain, (b) front view of the domain, (c) filter region.

4.3.5 Solver Setup

The Ansys Fluent 2023 R3 solver was used to discretize and solve the governing equations in an unsteady mode, with a fixed time step of 0.1 s and a maximum of 200 iterations per step. Only the energy equation was activated, while the momentum equations were omitted since convection was not considered. Heat transfer was modelled through conduction in the solid domains and radiation between boundaries. The maximum number of radiation iterations per time step was set to 50, with a residual convergence criterion of 1×10^{-5}. The second-order upwind discretization method was used to increase the stability and accuracy of the solution. The residuals of the simulation were set to 1×10^{-5}, and the simulation continued until the residuals became stable and numerical and physical convergences were achieved. The model was initialized with the hybrid method, setting the initial temperature uniformly to 296 K across the entire domain.

4.3.6 Sensitivity Analyses

4.3.6.1 Grid Independence

To ensure that the numerical results are not dependent of the grid size, a grid independence study was carried out. Four different grids were generated, ranging from approximately 2 to 8 million elements. The key factor in this process was the filter mesh element size, which directly influenced the overall grid resolution. The temperature distribution along the symmetry line on the filter surface was selected as the primary evaluation parameter, since it directly reflects the heat transfer characteristics between the heater and the filter.

According to Figure 5.3, refining the mesh from Case 1 to Case 3 progressively improved the accuracy of the predicted temperatures. However, the difference between Case 4 and Case 3 was negligible (less than 1%). Accordingly, Case 3 was selected as the optimal grid. The results thus confirm that the adopted mesh is adequate for ensuring grid-independent solutions. It provides sufficient resolution to capture heat transfer characteristics with confidence, while maintaining a reasonable computational cost.

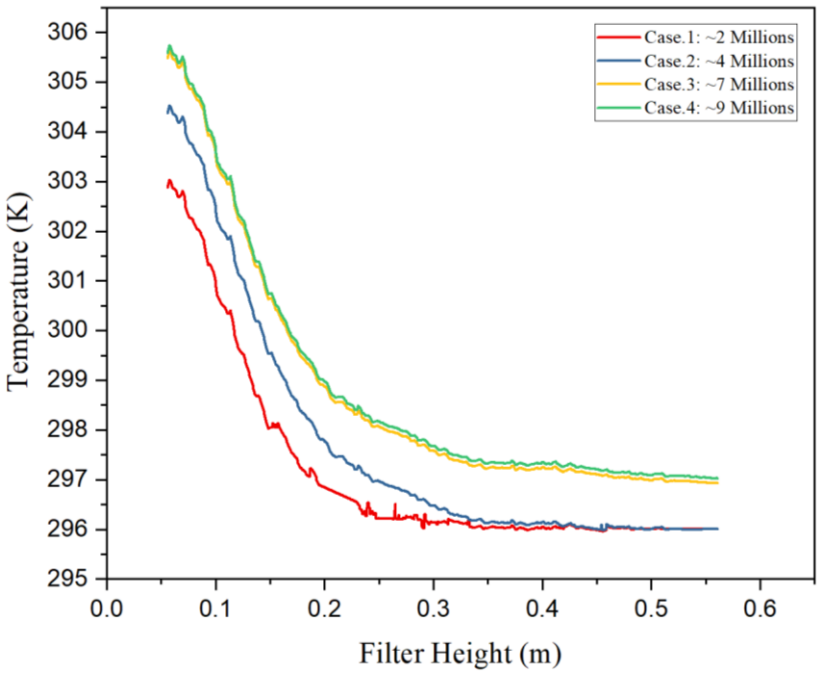

Figure 4.8. Grid independence study: comparison of the predicted temperature distribution along the symmetry line of the filter surface for four mesh densities $\alpha = 0°$, $\varepsilon = 0.8$ and $T_{setpoint} = 200$ ℃.

4.3.7 Numerical modeling matrix

The main simulations can be categorized into two groups. The first group focused on evaluating the influence of effective parameters such as thermal conductivity and different boundary conditions, through comparison of numerical predictions with experimental measurements. After identifying the parameter set that yielded the closest agreement with experiments, a second group of simulations was performed to model with three tilt angles of the ceramic heater, and the results were again compared with the experimental measurements. Table 4.1 presents the numerical simulation cases categorized by parameter variation and heater orientation.

The results of these simulations and their effects on the filter temperature will be plotted and discussed in Chapter 5.

Table 4.1. Summary of numerical simulation cases

Groups	Heater-Filter Distances (cm)	Tilt angle (°)	Ceramic heater setpoint temperature (℃)
Group 1	10	0	200
Group 2	10	0, 10, 20	200

4.4 Chapter Summary

This chapter analyzed radiative heat transfer between the infrared ceramic heater and the filter surface through both theoretical and numerical approaches. The fundamental principles of radiation exchange and the calculation of view factors were presented to describe the geometric dependence of radiative energy transfer. Building on this foundation, a three-dimensional numerical simulation was conducted using the S2S radiation model to replicate the experimental configuration and evaluate the resulting temperature distribution. The assumptions, boundary conditions, and solver settings were selected to ensure consistency with the experimental setup. Together, these analyses provide a comprehensive understanding of the radiative interactions governing heat transfer within the heater–filter system.

Chapter 5. Results and Discussion

5.1 Preface

In this chapter, the results obtained from the experimental, analytical, and numerical investigations are presented and analyzed. The primary purpose of this chapter is to evaluate the thermal performance of the developed radiant heating system and its ability to achieve uniform temperature distribution over pleated HVAC filters. The findings are discussed in relation to the effects of key parameters, such as the heater–filter distance, heater tilt angle, heater setpoint temperature, filter type, and system configuration on temperature uniformity and potential disinfection efficiency.

The experimental results form the basis of this thesis and provide the direct evidence of the system's thermal behaviour under controlled conditions. View factor calculations and numerical results are then compared with the experimental findings in order to provide deeper insight into the dominant heat transfer mechanisms, particularly radiation and natural convection and their influence on surface temperature distribution. Together, these analyses provide a comprehensive understanding of the thermal interactions within the system and confirm the validity of the proposed infrared heating approach.

5.2 Effect of Heater–Filter Distance on Filter Temperature Distribution

In this section, tests are conducted at a setpoint temperature of 250 ℃ and different heater to filter distances. The tested distances include 100 cm, 75 cm, 50 cm, 25 cm, 15 cm, and 10 cm. These experiments aim to assess the impact of heater placement on temperature distribution across the filter. The results indicated that changing the distance between ceramic heater and filter at a constant setpoint temperature has significant effect on the temperature distribution over the filter. For example, at a distance of 100 cm, only the upper region of the filter's front surface reached the

target temperature of 65 ℃. When the distance was reduced to 75 cm, both the upper and middle regions of the front surface, as well as the upper region of the back surface, achieved 65 ℃. At D=50 cm, nearly the entire filter reached the target temperature within 25 minutes, except for the lower section of the back surface, which remained below 65 ℃, as shown in Figures 5.1, 5.2 and 5.3 respectively.

The rise in filter temperature is attributed to the combined influence of radiative and natural convective heat transfer. As the air near the lower region of the filter's front surface absorbs incident radiation, its temperature and buoyancy increase, and warmer air transports heat toward the upper section of the filter. As a result, the lower section receives comparatively less convective heating and lead to the development of a vertical temperature gradient across the surface. This behaviour indicates that at larger heater–filter distances, natural convection becomes the dominant heat transfer mechanism. In contrast, the effect of radiative exchange between the heater and filter reduces with increasing distance.

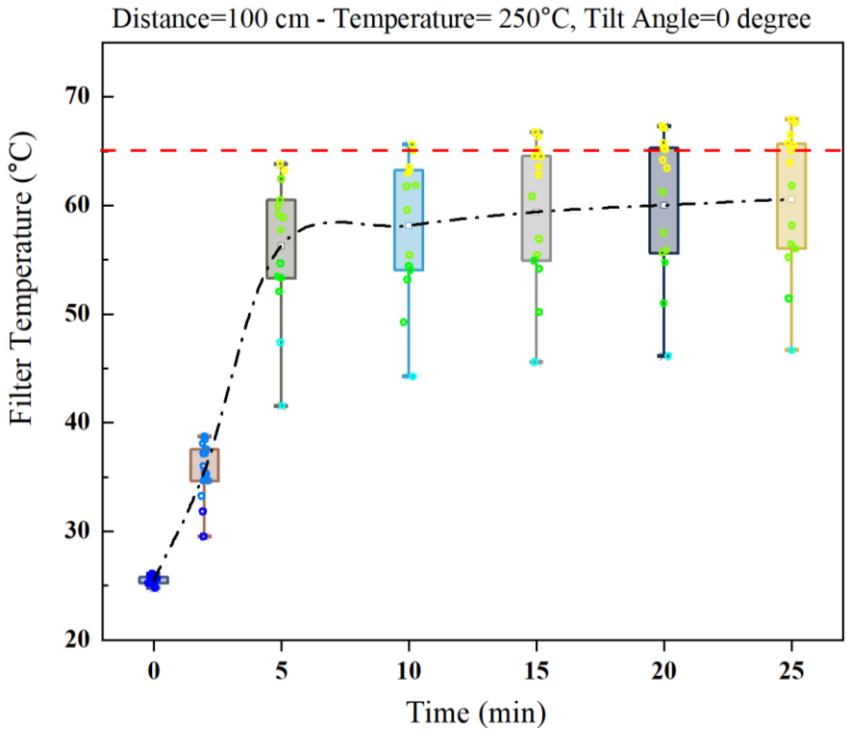

Figure 5.1. Temperature distribution over the filter over time at a ceramic heater temperature of 250°C and a distance of 100 cm.

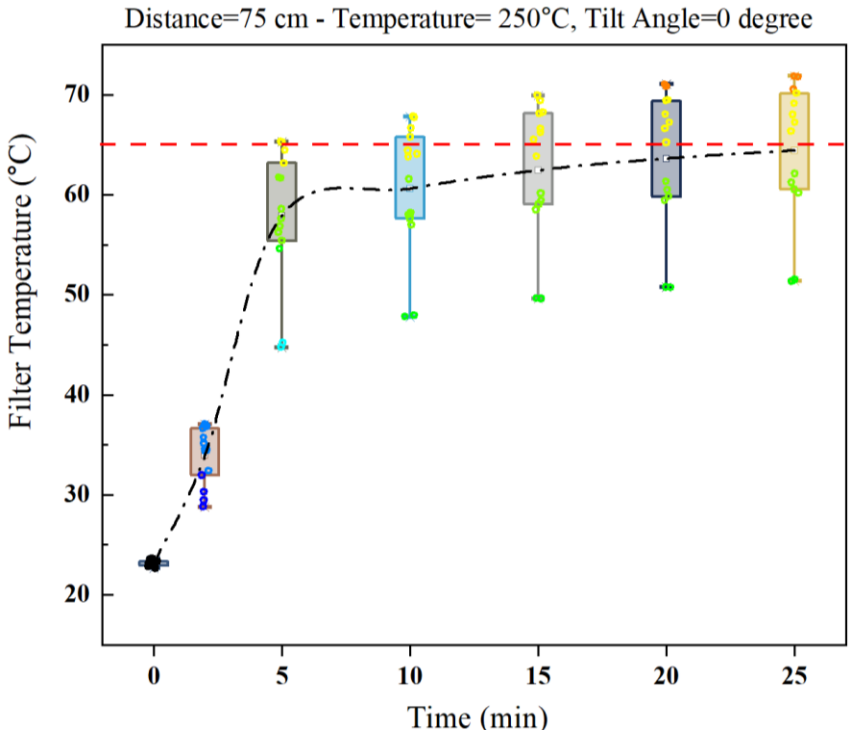

Figure 5.2. Temperature distribution over the filter over time at a ceramic heater temperature of 250°C and a distance of 75 cm.

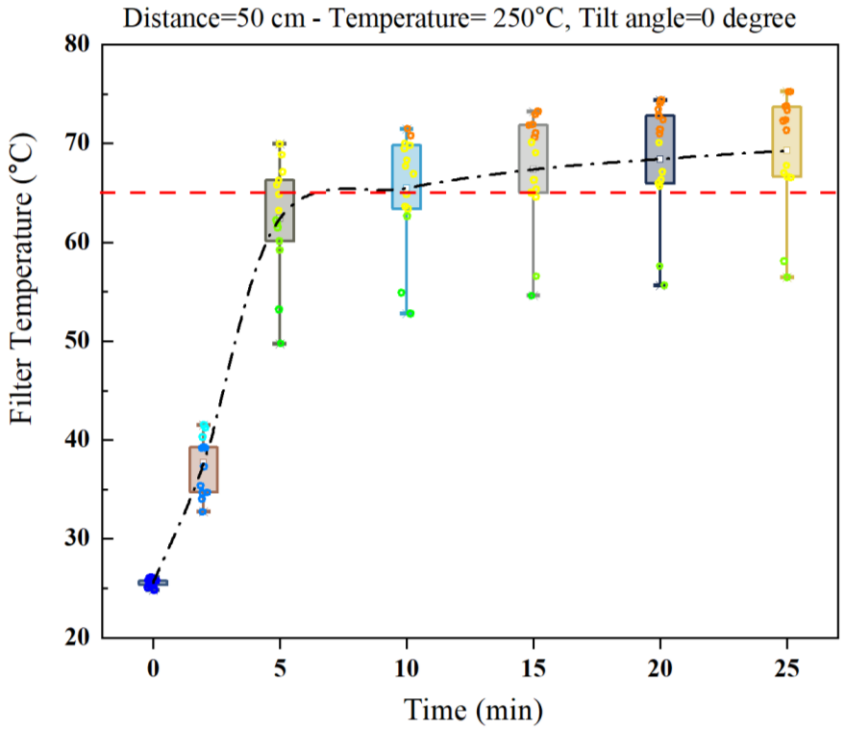

Figure 5.3. Temperature distribution over the filter over time at a ceramic heater temperature of 250°C and a distance of 50 cm.

According to the Figures 5.4 and 5.5 at heater–filter distances of 25 cm and 15 cm, the minimum temperature on the filter surface reached 65 ℃ after 14 minutes and 8 minutes, respectively. Additionally, the results showed that reducing the distance to 10 cm resulted in a large surface temperature gradient on the filter, ranging from 40 ℃ to 90 ℃, which can compromise disinfection uniformity. As can be seen from Figure 5.6, after approximately 5 minutes, the maximum temperature over the filter exceeded 90 ℃, while the minimum temperature was around 40 ℃. As a result, reducing the gap between the heater and the filter consistently raises the temperature measured on the filter. This occurs because, as the heater moves closer to the filter, the view factor between the two surfaces increases. Therefore, a greater portion of the emitted radiant energy can be absorbed by the filter. Also, the heat loss decreases at shorter distances.

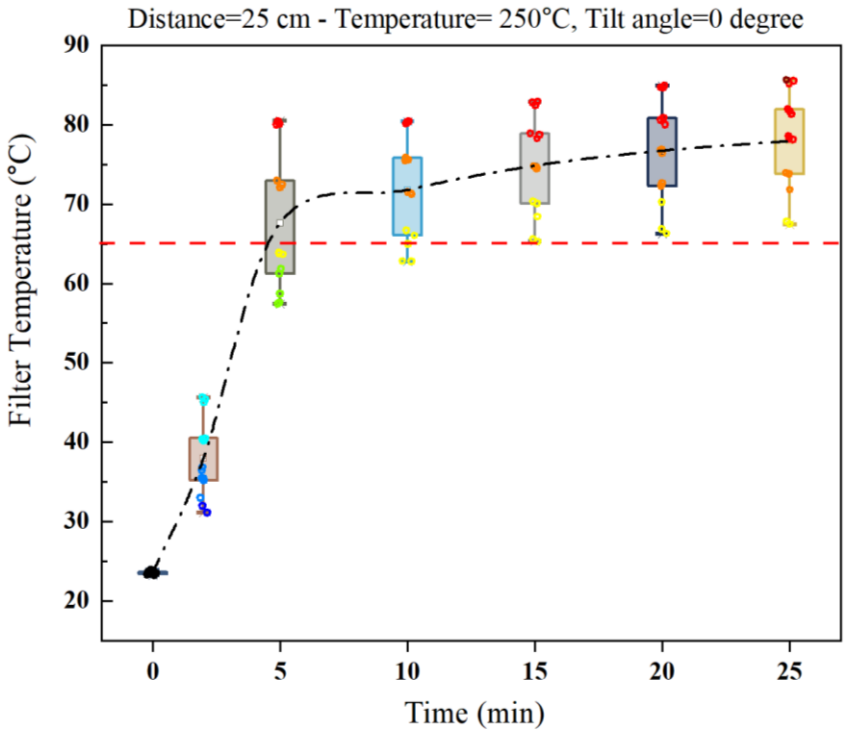

Figure 5.4. Temperature distribution over the filter over time at a setpoint temperature of 250°C and a distance of 25 cm.

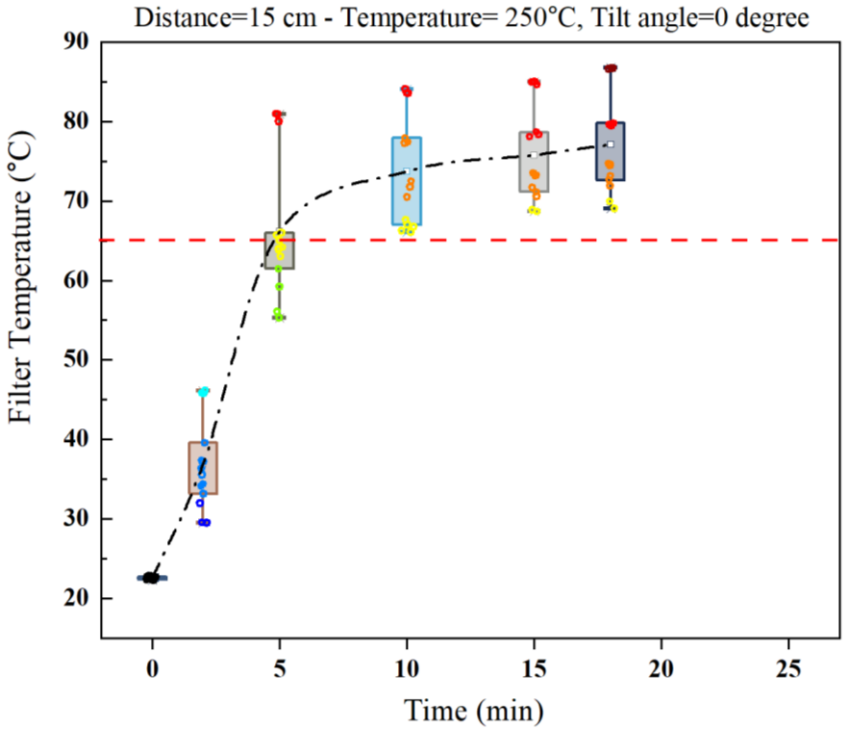

Figure 5.5. Temperature distribution over the filter over time at $T_{setpoint} = 250$ ℃℃, and a distance of 15 cm.

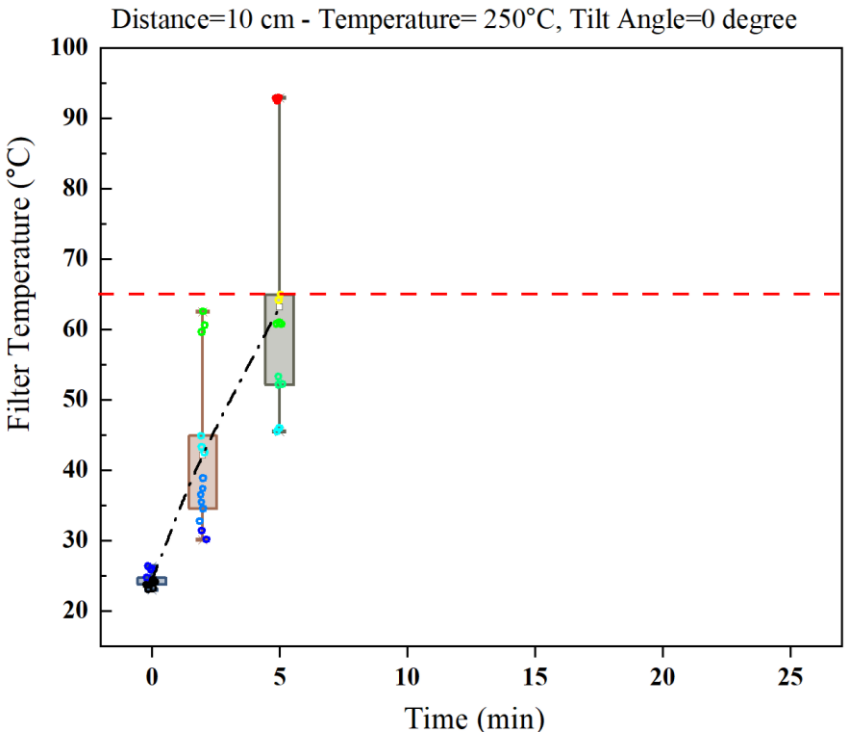

Figure 5.5. Temperature distribution over the filter over time at a$T_{set-point}$ = 250 ℃, and a distance of 10 cm.

Furthermore, the maximum temperature location over the filter depends on the distance between the heater and the filter. At distances of 100 cm and 75 cm, the maximum temperature happens in the top section of the filter front. However, at a distance of 50 cm, the maximum temperature is in the middle part of the filter. At shorter distances (i.e., 25, 15 and 10 cm), the bottom part of the filter face reaches the highest temperature. These findings highlight the interaction of different heat transfer modes. For example, natural convection becomes more influential heat transfer at higher distances, while at closer distances, the dominant heat transfer is radiation. In addition, the back side of the filter is warmed based on the conduction. Figures 5.7 to 5.10 showed the temperature distribution across different sections of the filter over time at heater-to-filter distances of 75 cm, 50 cm, 25 cm, and 15 cm, respectively. As shown, when D = 75 cm, the highest temperature appears at the upper region of the filter front. At D = 50 cm, both the middle and upper regions

show higher temperature levels, while at D = 25 cm and D = 15 cm, the maximum temperature shifts toward the lower portion of the filter front. In all cases, the minimum temperature occurs at the bottom region on the rear side of the filter. This is attributed to the influence of natural convection. Initially, the back side of the filter is heated by conduction through the filter media. Once the rear surface temperature increases, natural convection in the adjacent air layer becomes the dominant mode of heat transfer; therefore, the heat moves upward and the temperature on the back side of the filter increases more slowly but continuously over time.

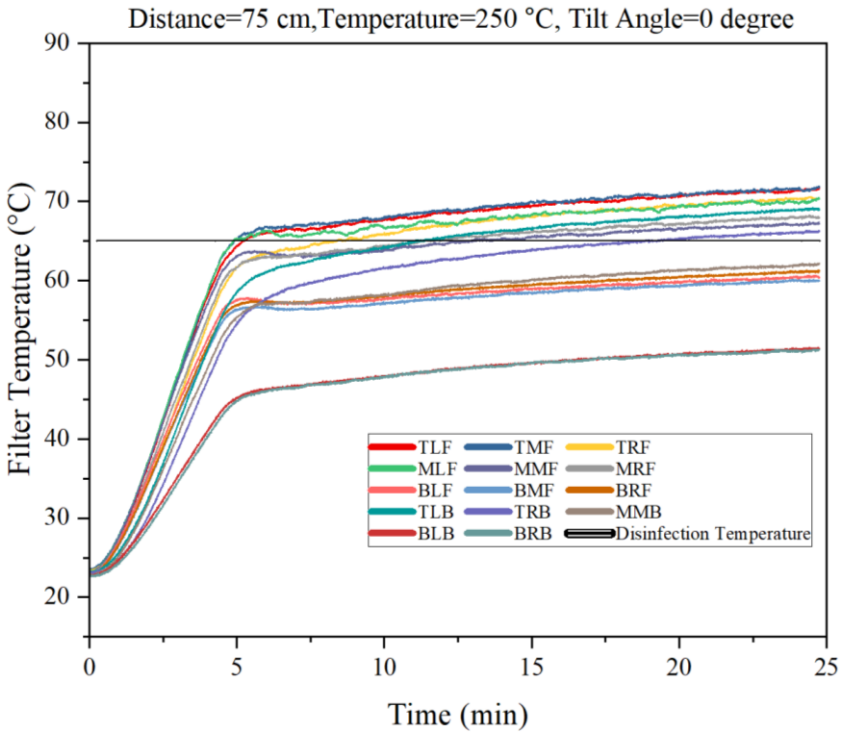

Figure 5.7. Temperature distribution of different points of the filter over time at D=75 cm and $T_{setpoint} = 250$ ℃

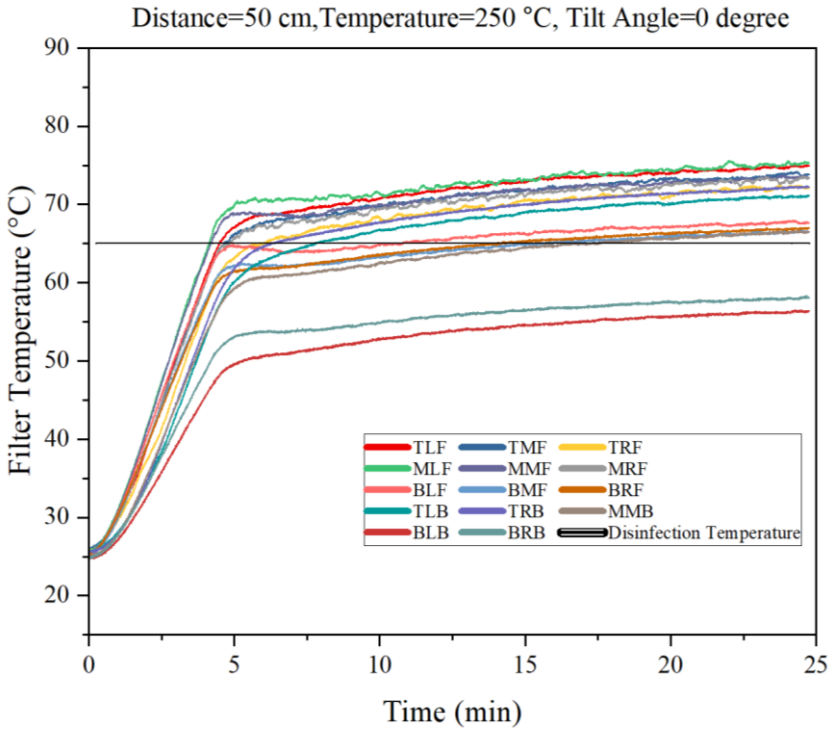

Figure 5.8. Temperature distribution of different points of the filter over time at D=50 cm and $T_{setpoint}$ = 250 ℃

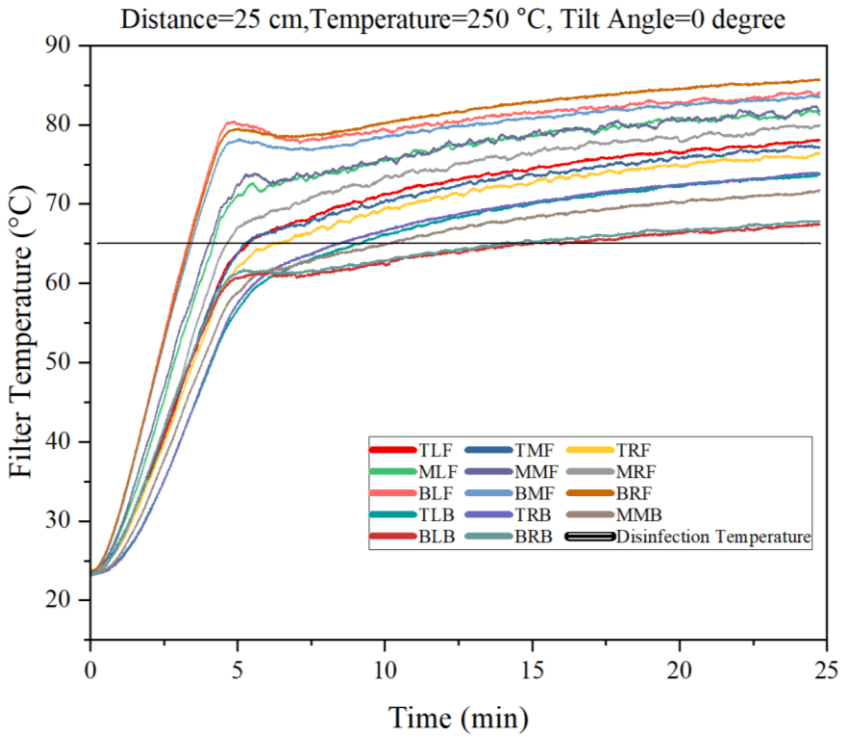

Figure 5.9. Temperature distribution of different points of the filter over time at D=25 cm and $T_{setpoint}$ = 250 ℃

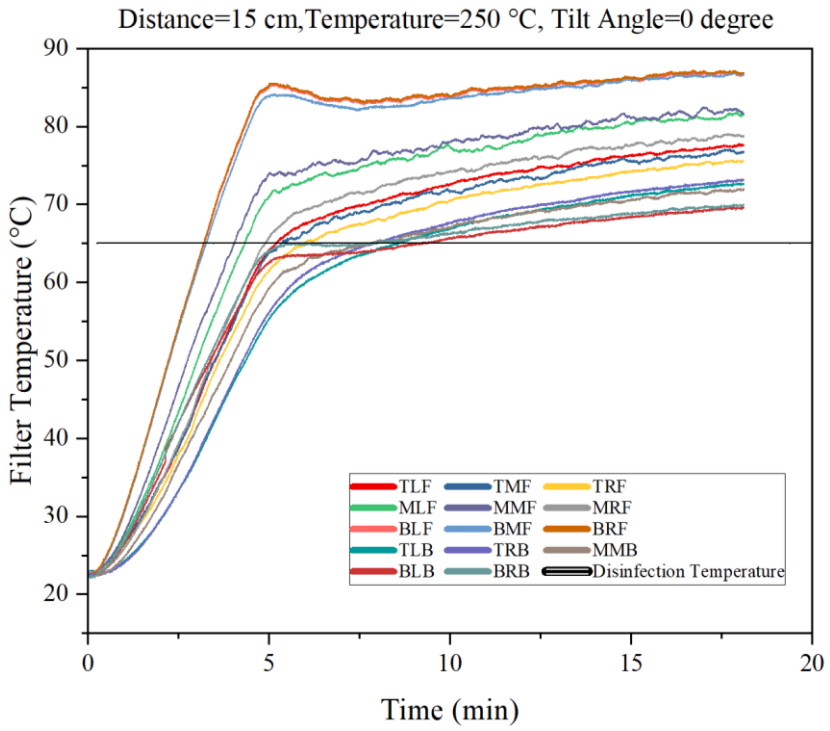

Figure 5.10. Temperature distribution of different points of the filter over time at D=15 cm and $T_{setpoint}$ = 250 ℃

5.3 Effect of Heat Source Temperature on The Filter Temperature Distribution

In this section, the influence of the ceramic heater's setpoint temperature on the temperature distribution over the filter surface is evaluated. As discussed in Section 5.1, at distances of 50 cm and greater, the minimum temperature over the filter did not reach the required disinfection threshold of 65 ℃. These findings indicated that increasing the setpoint temperature is necessary at larger distances. Figure 5.11 illustrate the temperature variations over the filter at a setpoint temperature of 300 ℃ for D = 50 cm. A comparison between Figure 5.3 and Figure 5.11 shows that when the setpoint temperature was raised from 250 ℃ to 300 ℃ at D = 50 cm, the minimum temperature across the filter reached 65 ℃ within 22 minutes. In contrast, at 250 °C, the minimum temperature did not reach 65 ℃ even after 25 minutes.

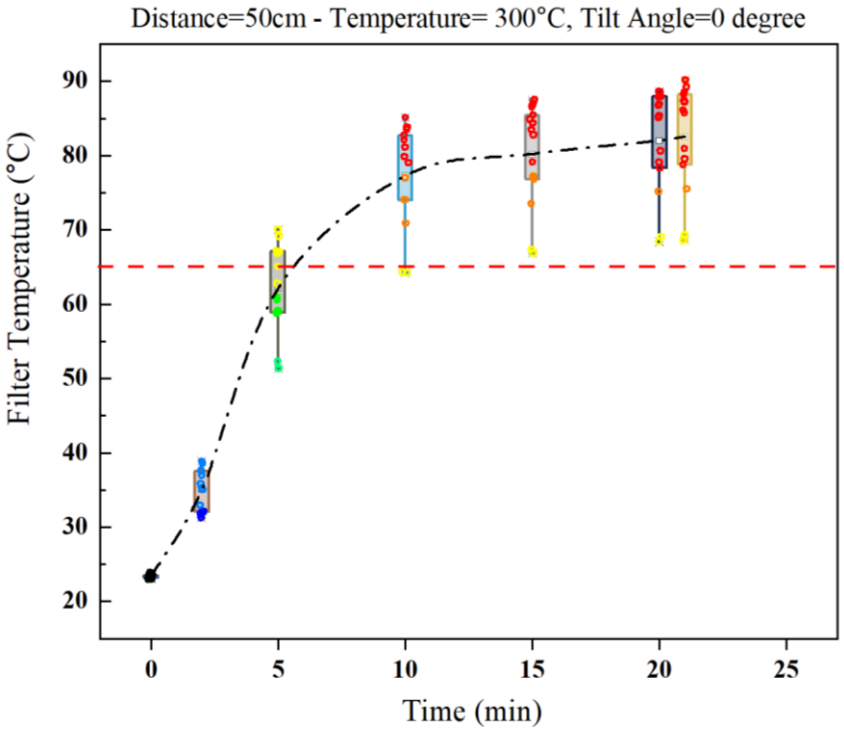

Figure 5.11. Temperature distribution over the filter over time at D=50 cm and $T_{setpoint}$ = 300 ℃

Conversely, at shorter distances such as D = 10 cm, the maximum temperature exceeded 90 ℃ while the minimum remained around 40 ℃. For safety reasons, the system was stopped once this condition was reached, therefore, at smaller distances, a reduction in setpoint temperature is required to prevent overheating. In Figures 5.12a and 5.12b the temperature variations over the filter at a setpoint temperature of 220 ℃ and 180 ℃ for D = 10 cm, are represented. As shown in Figure 5.12a, at 220 °C the maximum temperature again rose above 90 ℃ within a few minutes, confirming that this condition still leads to local overheating.

The comparison between Figures 5.6 and 5.12b demonstrates that lowering the setpoint temperature from 250 ℃ to 180 ℃ at D = 10 cm significantly changes the thermal behavior across the filter. At a heater setpoint of 180 ℃, the maximum surface temperature reached slightly above

70 ℃ after 25 minutes, while at 250 ℃ it exceeded 90 ℃ in less than five minutes, posing a potential risk of filter damage. However, the minimum temperature at 180 ℃ remained around 50 ℃, suggesting that although this lower setpoint improved temperature uniformity, it was insufficient to achieve the required disinfection temperature across the entire filter surface.

These observations confirm that appropriate adjustment of the heater setpoint temperature is essential to maintain safe and uniform heating conditions across the filter surface at different distances.

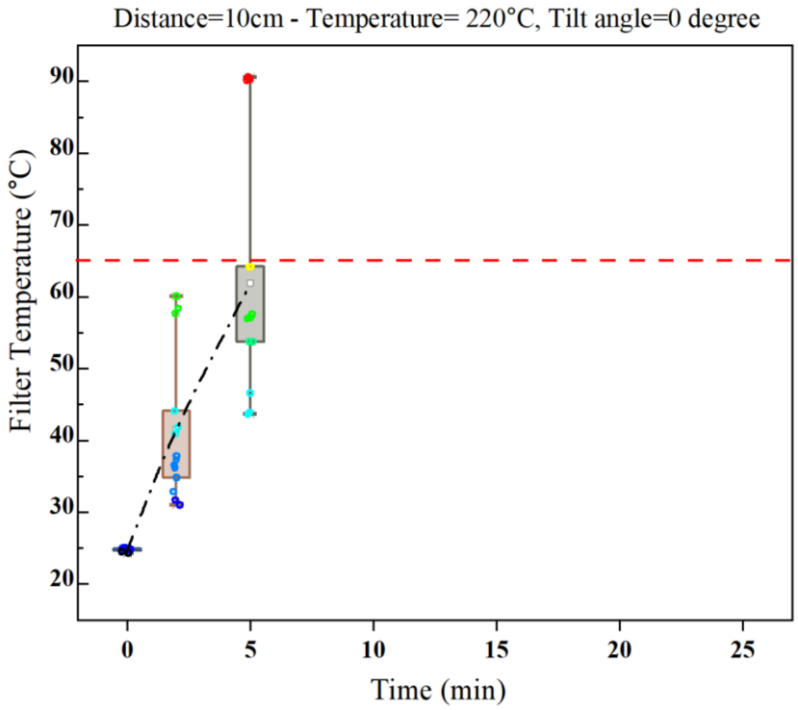

(a)

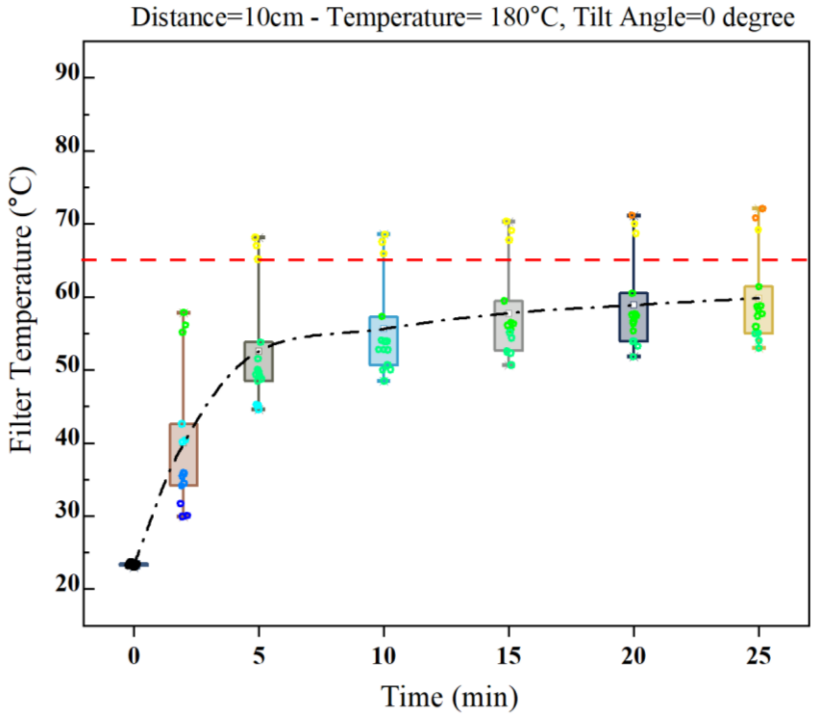

(b)

Figure 5.12. Temperature distribution over the filter over time at D=10 cm and (a) setpoint temperature of 220 ℃ and (b) 180 ℃

5.4 The Impact of Increasing Tilt Angle of the Ceramic Heater

As discussed, at closer distances, the maximum temperature was located on the bottom side of the filter. Therefore, if the tilt angle of the ceramic heater increased, the temperature distribution would become more uniform. Figure 5.13 represent temperature variation of the front surface of the filter at different tilt angles during 25 minutes at a heater–filter distance of 25 cm and a setpoint temperature of 250 ℃. As can be seen from the Figure 5.13, the temperature at the bottom section of the filter decreased with increasing tilt angle, whereas the temperatures at the middle and top sections increased. For example, the temperature at the bottom when $\alpha = 0°$ decreased from approximately 84.1 ℃ to about 78.3 ℃ at $\alpha = 20°$ during 25 minutes.

These behaviors can be attributed to the change in the radiative view factor between the heater and the filter as the tilt angle increases. A detailed explanation of this phenomenon is provided in Section 5.8. To better compare the temperature behavior across different regions of the filter, Figure 5.14 presents the temperature variation at tilt angles of 0° and 20°.

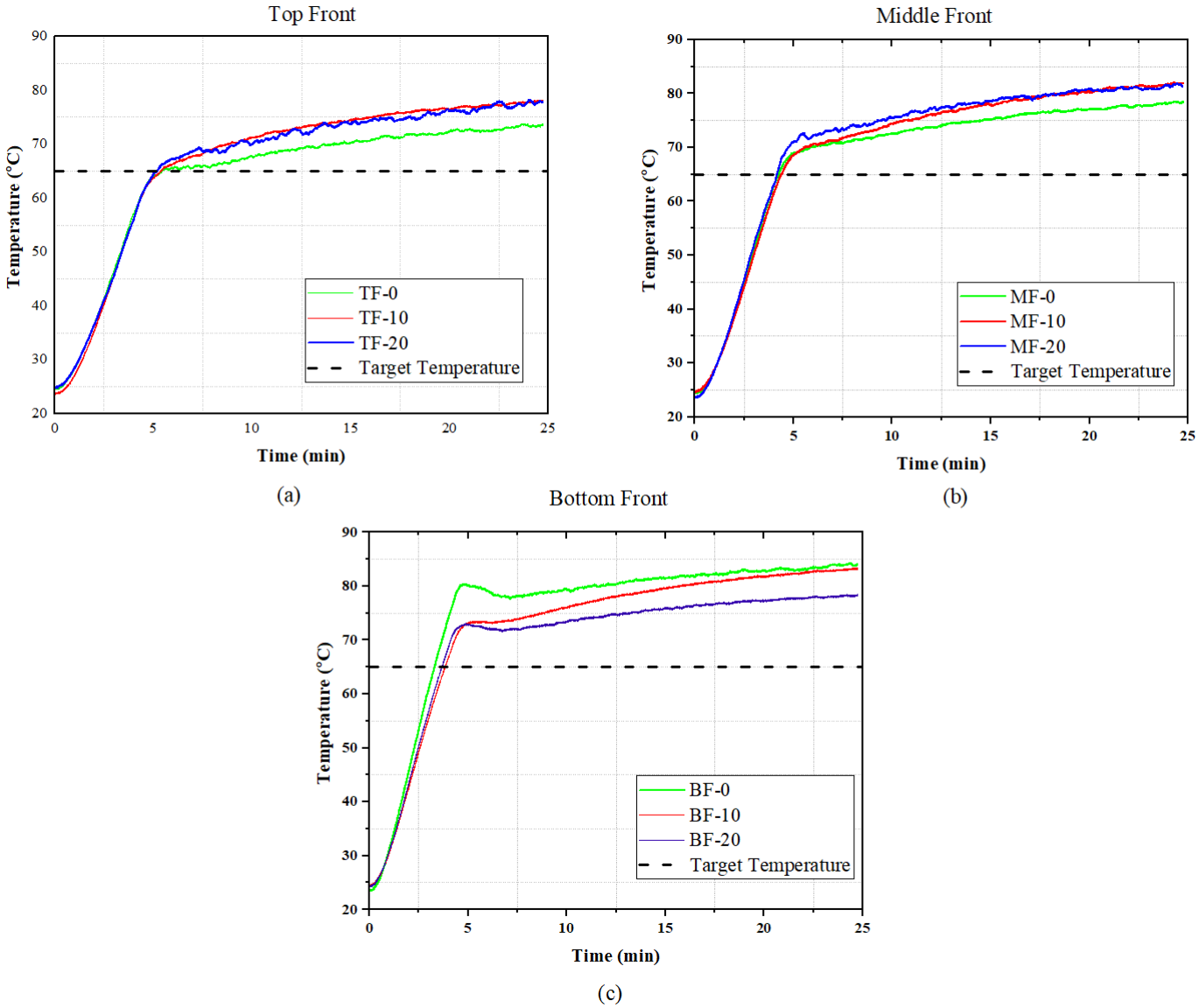

Figure 5.13. Temperature variation over the top (a), middle (b), and bottom (c) sections of the filter front surface at tilt angles of $\alpha = 0°$, $\alpha = 10°$, and $\alpha = 20°$, at D=25 cm and $T_{set-point} = 250$ ℃

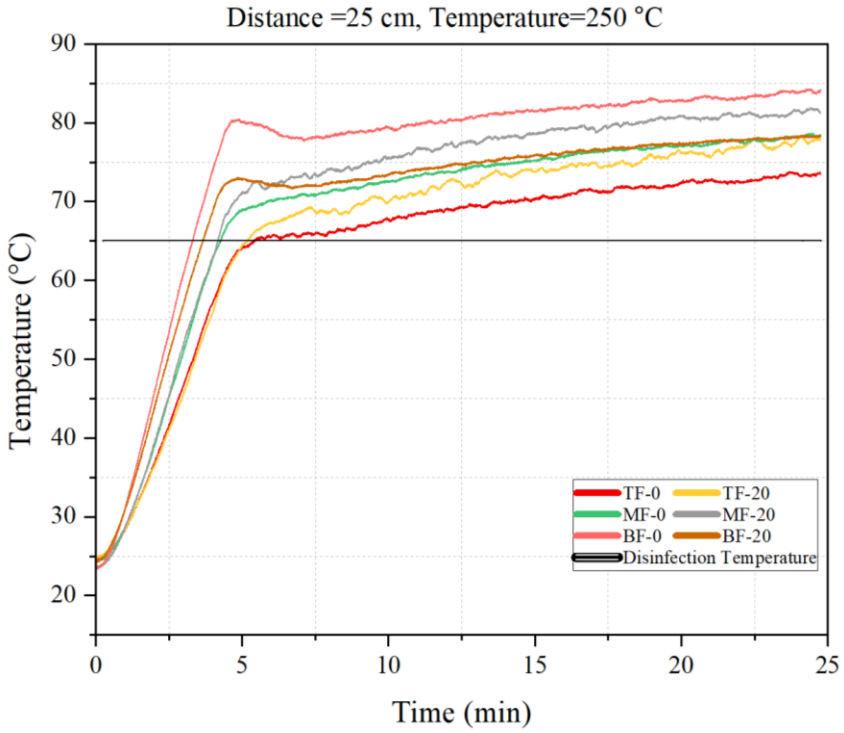

Figure 5.14. Temperature variation over the top, middle, and bottom regions of the filter front surface at tilt angles $\alpha = 0°$, and $\alpha = 20°$, at D=25 cm and $T_{set-point} = 250$ ℃

Moreover, the results demonstrated that at a distance of 10 cm and a setpoint temperature of 250 ℃, when the heater was positioned horizontally (tilt angle=0 °), the maximum temperature difference between the top and bottom sides of the filter was approximately 40 ℃ after 5 minutes of heating (Figure 5.5). In contrast, when the tilt angle was increased to 10° and 20°, the temperature difference across the front surface of the filter decreased to about 36.2 ℃ and 23.3 ℃ after the same duration, respectively (Figure 5.15a and 5.15b). This finding indicates the positive influence of increasing the tilt angle, which enhances the temperature uniformity over the filter surface. Regarding figure 5.15b. at a setpoint temperature of 250 ℃ and a tilt angle of 20 °, although the minimum temperature over the filter reached 65 ℃ after 8 minutes, the maximum temperature exceeded 90 ℃ after 12 minutes.

Therefore, lower setpoint temperature was selected for this configuration. Figure 5.16, show the temperature distribution at D= 10 cm, and setpoint temperature of 220 ℃. It can be observed that adjusting the tilt angle and setpoint temperature allows the filter to be effectively disinfected even at a shorter distance. At D = 10 cm, $\alpha = 20$ ° and a setpoint temperature of 220 ℃, the filter can be disinfected after 25 minutes, with a maximum temperature difference of about 15.1 ℃ across the entire filter and approximately 10 ℃ on the front surface.

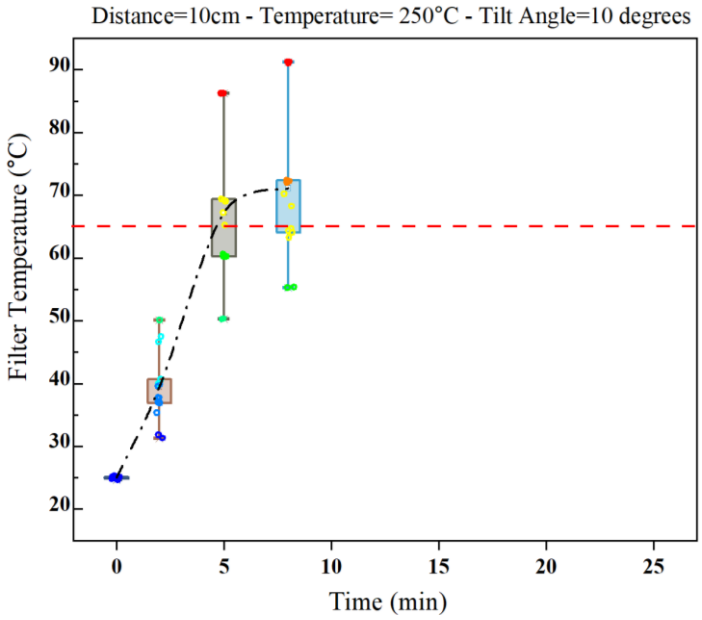

Figure 5.15 a. Temperature distribution on the filter front at D=10 cm, $T_{setpoint} = 250$ ℃, and $\alpha = 10$ °.

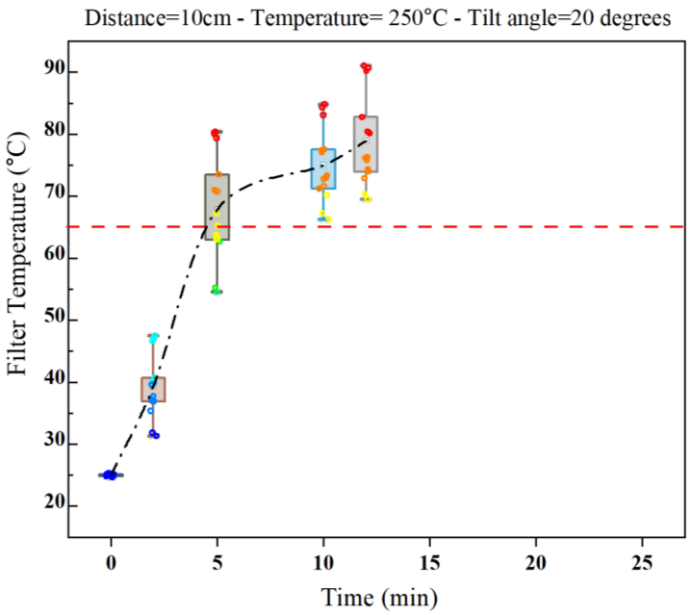

Figure 5.15 b. Temperature distribution on the filter front at D=10 cm, $T_{setpoint} = 250$ ℃, and $\alpha = 20$ °.

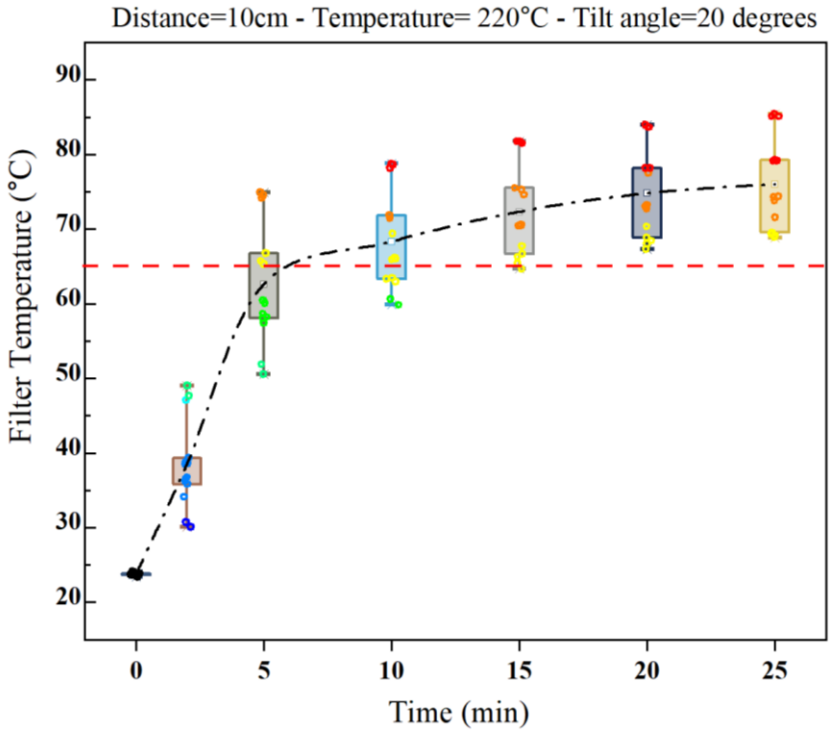

Figure 5.16. Temperature distribution on the filter front at $T_{setpoint}$ = 220 ℃, D=10 cm, and at α = 20 °.

In the following, temperature distribution over the filter for tilt angles of $\alpha = 10\,°$ and $\alpha = 20\,°$ at distances of 15 cm and 25 cm, are presented in Figures 5.17 and 5.18, respectively. Regarding Figures 5.17(a) and 5.17(b), at $\alpha = 10\,°$, the filter reached the target temperature of 65 ℃ faster than at $\alpha = 20\,°$, requiring 17 minutes and 22 minutes, respectively. However, the maximum temperature difference over the filter at $\alpha = 20\,°$ was smaller than that at $\alpha = 10\,°$, indicating improved temperature uniformity at the higher tilt angle. However, at D = 25 cm, there is no significant difference in the temperature distribution over the filter when changing the tilt angle. This indicates that at larger distances, the variations in the geometric orientation between the heater and the filter have only a minor influence on the portion of radiative energy received by the filter surface.

For a better comparison, the results for three tilt angles, along with the corresponding energy consumption of the cases in which the filter achieved complete disinfection, are summarized in Table 5.1.

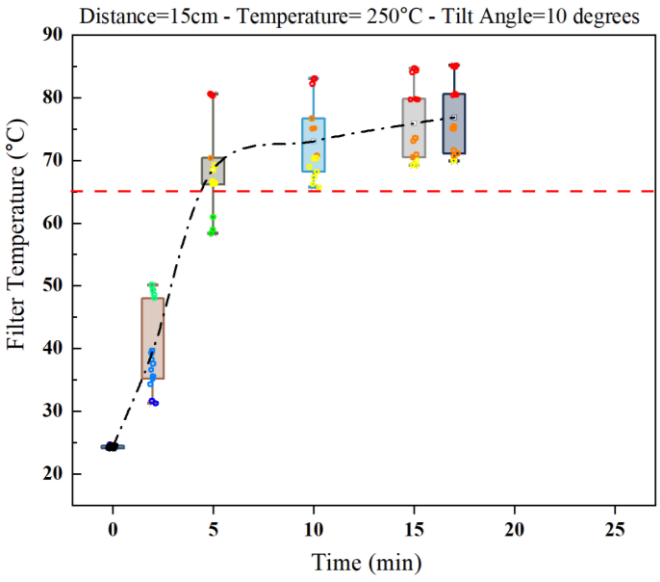

Figure 5.17 a. Temperature distribution on the filter front at D=15 cm, $T_{setpoint} = 250$ ℃, and $\alpha = 10$ °

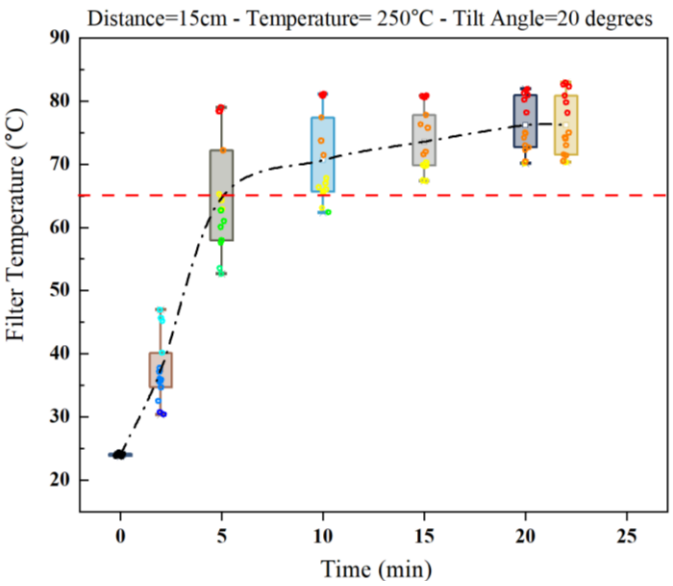

Figure 5.17 b. Temperature distribution on the filter front at D=15 cm, $T_{setpoint} = 250$ ℃, and $\alpha = 20$ °.

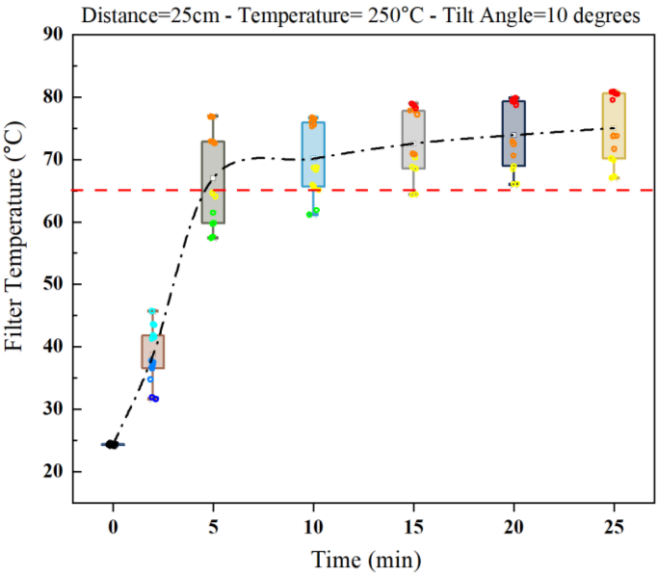

Figure 5.18 a. Temperature distribution on the filter front D=20 cm, $T_{setpoint} = 250$ ℃, and $\alpha = 10$ °.

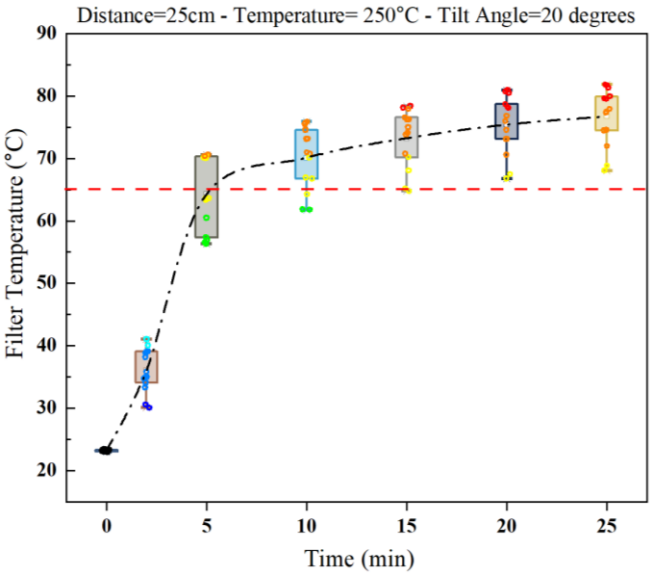

Figure 5.18 b. Temperature distribution on the filter front at D=25 cm, $T_{setpoint} = 250$ ℃, and $\alpha = 20$ °.

Table 5.1. the effect of changing the tilt angle on temperature distribution over the filter

Tilt Angle (α°)	Distance (D) (cm)	Setpoint Temperature ℃	Duration (min)	Electrical Energy Consumption (kWh)	Total Temperature Difference ℃	Temperature Difference (filter front) ℃
0	15	250	18	0.04	16.2	12.1
	25	250	24	0.05	18.1	7.0
	50	300	21	0.06	21.5	15
10	15	250	17	0.04	15.5	10.5
	25	250	26	0.05	13.0	7.5
20	10	220	25	0.05	16.5	11.1
	15	250	22	0.05	11.3	8.2
	25	250	25	0.05	16.2	5.6

In summary, a comprehensive analysis of how variations in heater-to-filter distance and tilt angle affect the temperature distribution across the filter surface was provided. Consequently, the most suitable configuration depending on the specific application requirements can be selected based on prioritized criteria, such as energy efficiency, processing time, or thermal uniformity.

5.4.1 Measurement Uncertainty and Data Representation

The methodology used for evaluating measurement uncertainty is described in detail in chapter 3, section 3.4. The Figure 5.19 is presented here to illustrate how the uncertainty range compares with the measured temperature variations. Because the magnitude of the uncertainty was found to be minor, the detailed uncertainty analysis was performed only for the temperature distribution data corresponding to a single representative condition ($D = 25\ cm, \alpha = 20\ °,$ and $T_{setpoint} = 250$ ℃). Since the overall uncertainty was relatively small compared with the recorded temperature differences, it had a negligible effect on the measured temperature distribution and temporal evolution, confirming the reliability and repeatability of the experimental data.

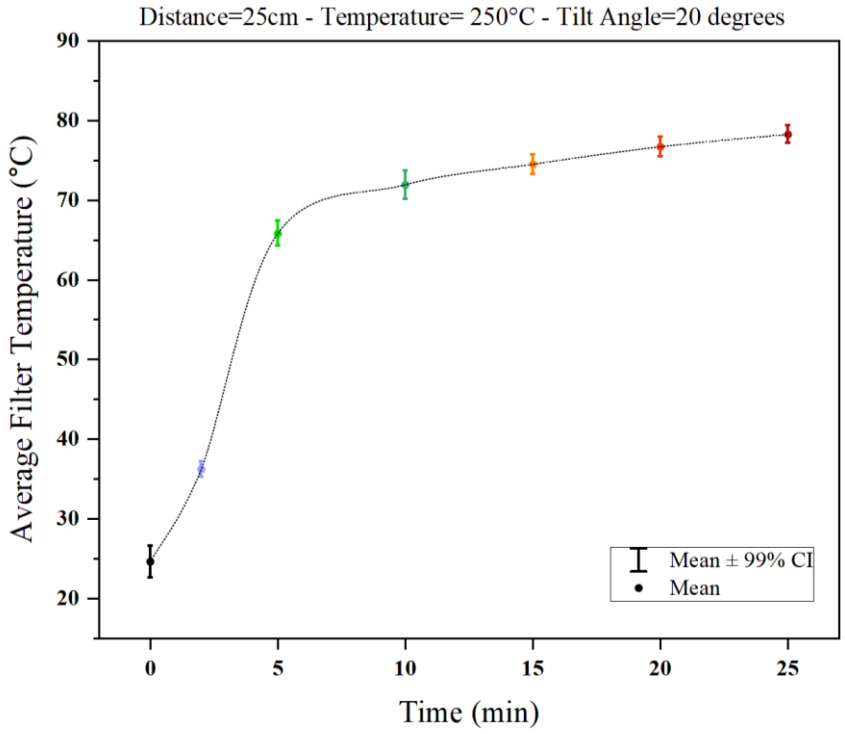

Figure 5.19. Average filter temperature during 25 minutes at $D = 25\ cm, \alpha = 20\ °,$ and $T_{setpoint} = 250$ ℃. Error bars represent the 99% confidence interval of five repeated measurements ($n = 5$).

5.5 The Impact of the Reflector Behind the Ceramic Heater

In this section, the effect of placing aluminum foil as a reflector directly behind the ceramic heater is investigated. The results demonstrate the positive impact of using a reflector. For instance, as previously shown in Figure 5.20, at D=25 cm, $\alpha = 20\ °$ and setpoint temperature of 250 ℃, the minimum temperature over the filter reaches 65 ℃ in 15 minutes when the ceramic heater is mounted with a reflector. In contrast, when the reflector is removed, this time increases to 20 minutes (Figure 5.21). This reduction in the time required to reach the target temperature decreases the overall disinfection duration and contributes to improved energy efficiency. Furthermore, after 25 minutes, thermal uniformity across the filter surface increases, and the temperature difference between the bottom and top sections decreases from approximately 9.2 ℃ (without reflector) to about 7.5 ℃ (with reflector), indicating a more even heat distribution.

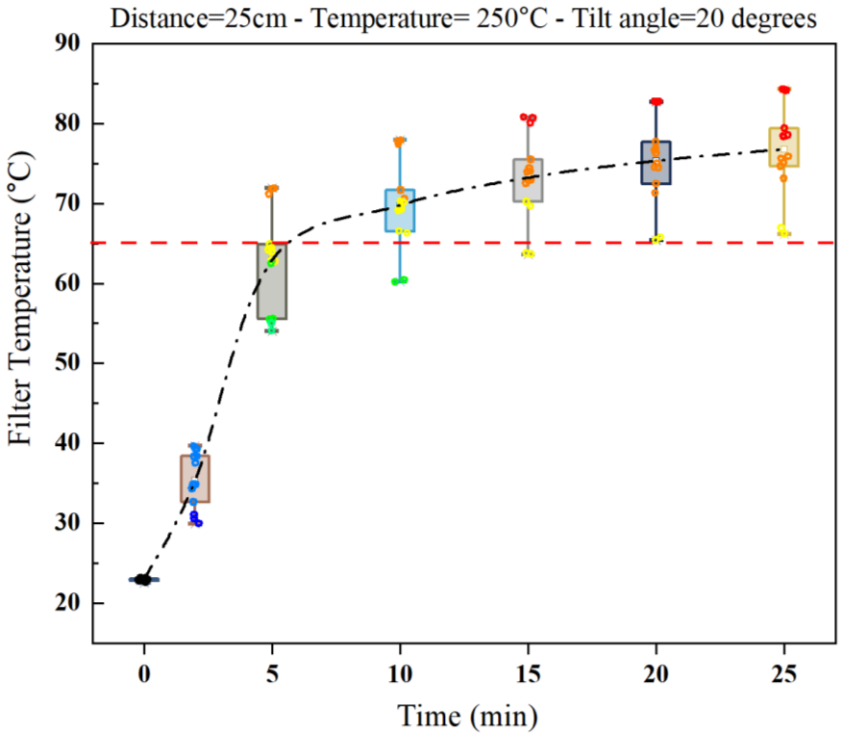

Figure 5.20. Temperature distribution on the filter front at D=25 cm, $\alpha = 20$ °, and $T_{setpoint} = 250$ ℃, when the aluminum reflector is removed

Figure 5.21 shows temperature variation at different sections (bottom, middle, and top) of the filter front with and without the aluminum reflector at D=25 cm, $\alpha = 20$ ° and setpoint temperature of 250 ℃. As it is evident from Figures 5.21 a, 5.21 b and 5.21 c, the impact of the aluminum reflector is most noticeable at the bottom section of the filter front. However, the middle and top sections show negligible change. In other words, due to natural convection, heat tends to rise, which causes the temperature at the top of the filter to be higher than at the bottom, leading to uneven heating along the vertical direction. Consequently, the reflector, by increasing the amount of radiative heat directed toward the lower part of the filter, helps balance this uneven distribution. It ensures that

the bottom section, which generally stays cooler, receives more heat, resulting in a more uniform temperature across the filter surface.

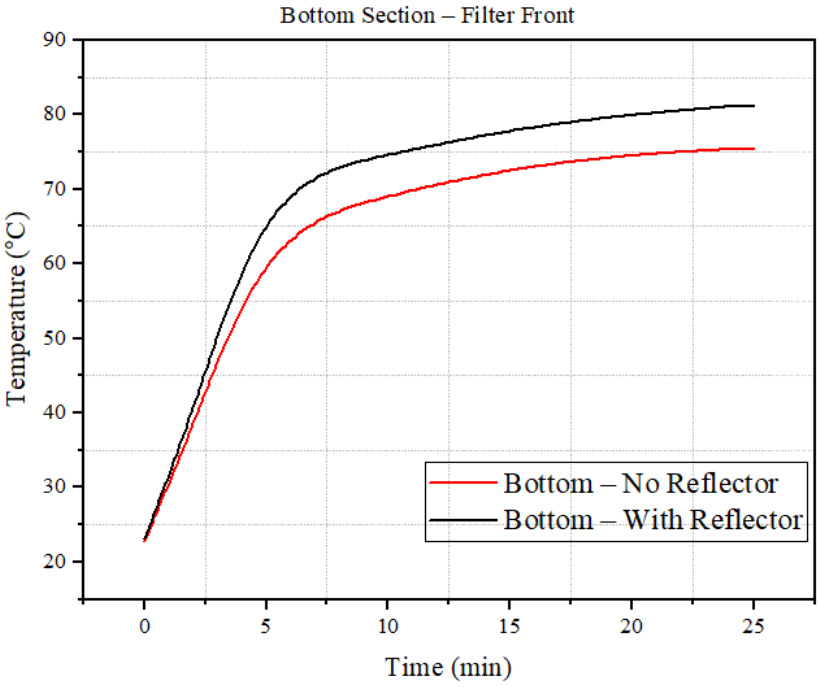

(a)

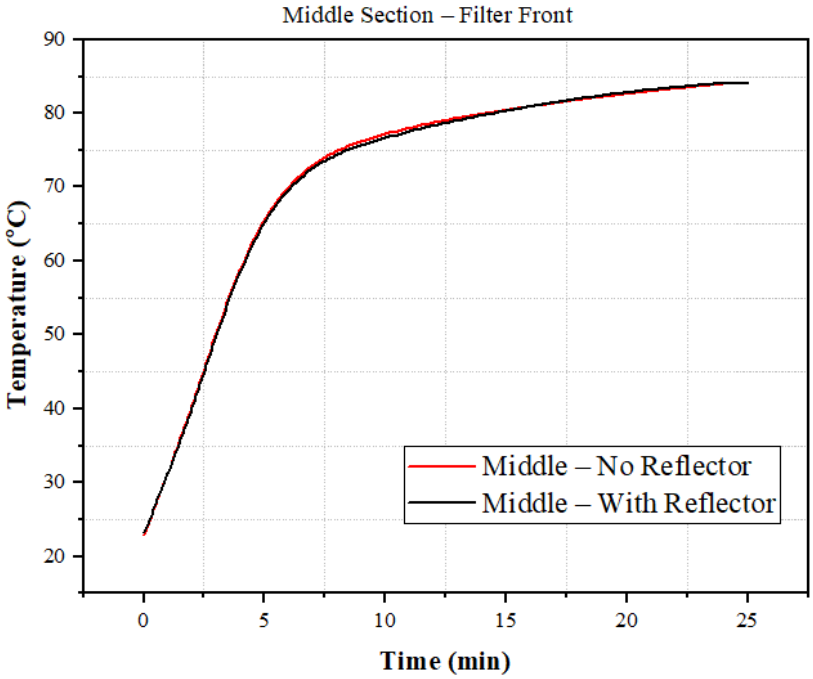

(b)

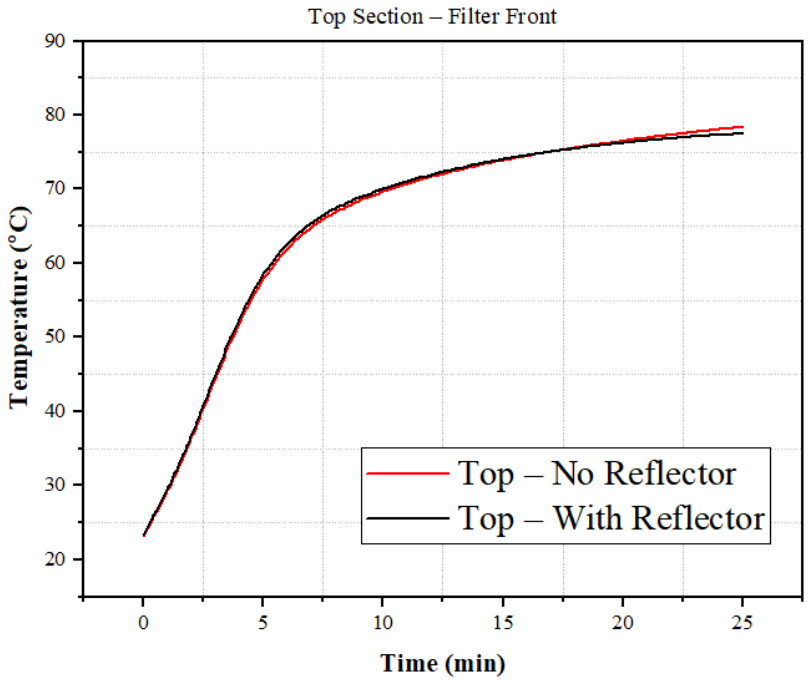

(c)

Figure 5.21. Temperature distribution at the (a) Bottom, (b) Middle and (c) Top side of the filter front over a 25-minute heating period, with and without the aluminum reflector at D= 25 cm, $\alpha = 20$ ° and $T_{set-point} = 250$ ℃.

5.6 System Performance in the Duct without Aluminum-Foil-Covered Gates

In this section, the performance of ceramic heaters is evaluated in a duct setup that represents a realistic configuration of an HVAC system operating without active airflow. The main reason is to assess the heater's direct influence on temperature distribution and disinfection efficiency without external modifications. To remove auxiliary influences, the aluminum foil covering the unit's gates and the reflector mounted behind the ceramic heater were removed.

Initially, a single ceramic heater is used without a reflector or a mounted gate. The aluminum foils are removed from both sides of the unit. Experiments are conducted at distances of 10 cm, 15 cm, and 25 cm, and tilt angle of 0 ° and 20 °, using ceramic heater setpoint temperatures of 250 ℃, 300 ℃, and 350 ℃. Figures 5.22 and 5.23 illustrate the schematic and actual setup of the test unit,

respectively. In Figure 5.23, the configuration includes the removal of aluminum foil from the side gates to reflect a simplified HVAC duct layout.

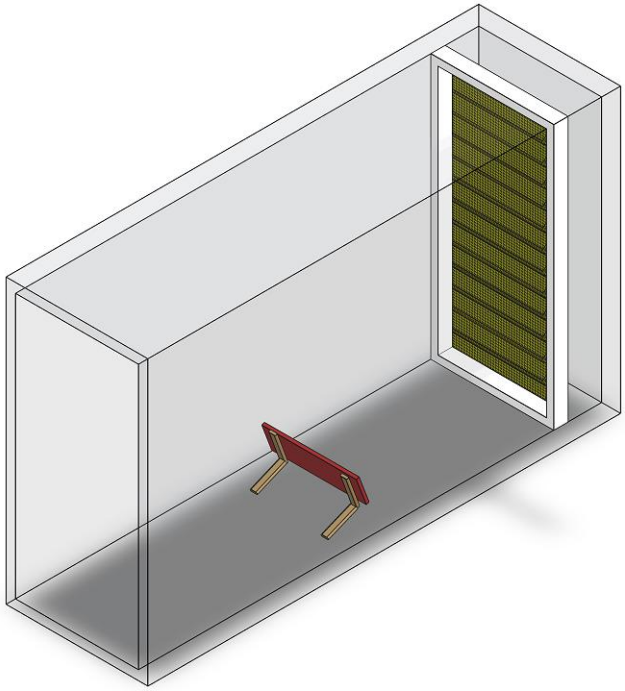

Figure 5.22. Schematic representation of the test duct setup used for evaluating a ceramic heater performance in a duct without aluminum foil-covered gates.

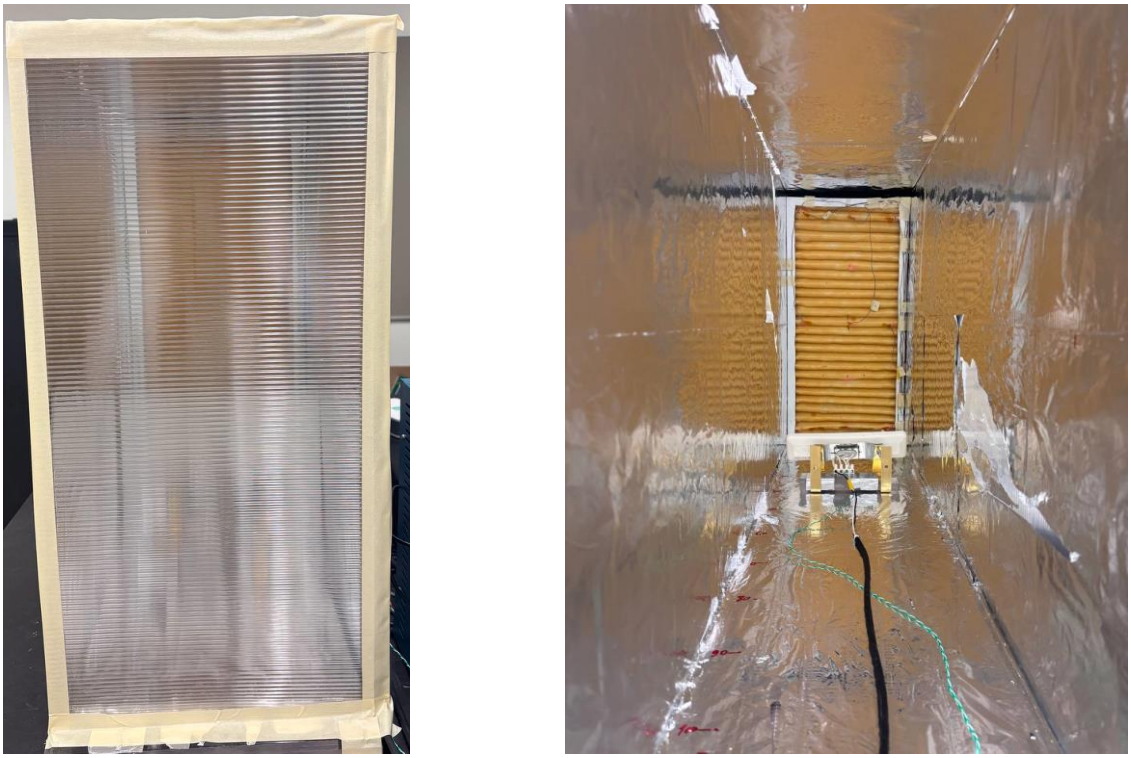

(a) (b)

Figure 5.23. Experimental setup used to evaluate the ceramic heater performance in a duct without aluminum foil-covered gates. (a) Front view of the duct showing the transparent polycarbonate wall after removing the aluminum. (b) Internal view of the duct showing the ceramic heater placed in front of the pleated filter,

Figures 5.24 and 5.25 show the temperature distribution over the filter at D=10 cm and D=15 cm, with tilt angles of $\alpha = 0\,^\circ$ and $\alpha = 20\,^\circ$, respectively. In these tests, one ceramic heater is used in front of the filter without using any aluminum foil covered for the unit's gates. The results showed that at a distance of D = 10 cm and a setpoint temperature of 250 ℃, the maximum temperature on the filter surface exceeded 95 ℃ after 5 minutes when the tilt angle was $\alpha = 0\,^\circ$. However, when the tilt angle was increased to $20\,^\circ$, the temperature over the filter surface was significantly reduced and remained under 65 ℃. Similarly, as shown in Figure 5.25, when the distance was increased to 15 cm, the filter temperature remained below 65 ℃ at the back side of the filter for $\alpha = 0\,^\circ$ and over the entire filter surface for $\alpha = 20\,^\circ$. Therefore, higher setpoint temperature to achieved effective disinfection at larger heater-to-filter distances is recommended.

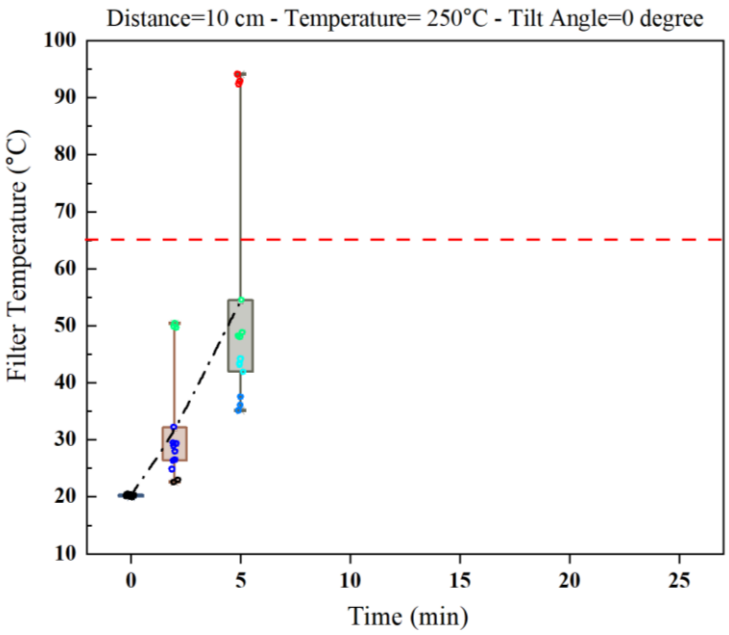

(a)

Figure 5.24a. Temperature distribution across the filter using one ceramic heater set to 250 ℃, at D= 10 cm and $\alpha = 0°$ with transparent gates

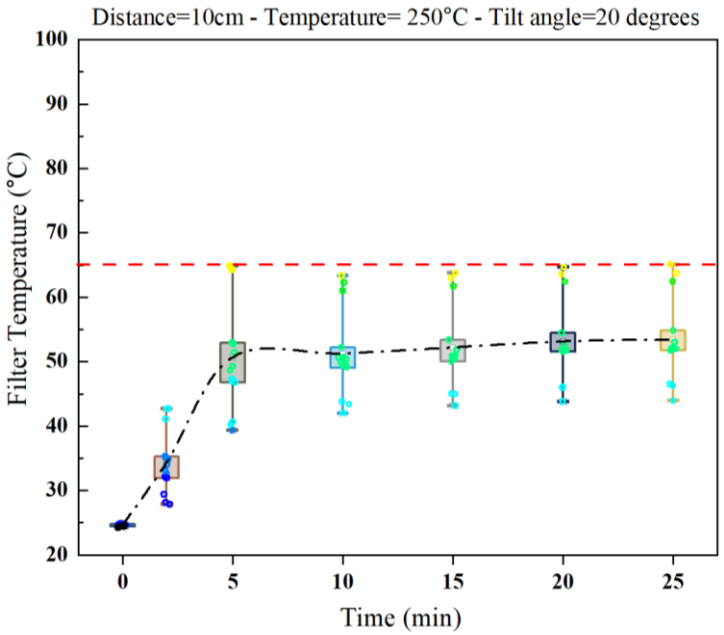

(b)

Figure 5.24b. Temperature distribution across the filter using one ceramic heater set to 250 ℃, at D= 10 cm and $\alpha = 20°$ with transparent gates

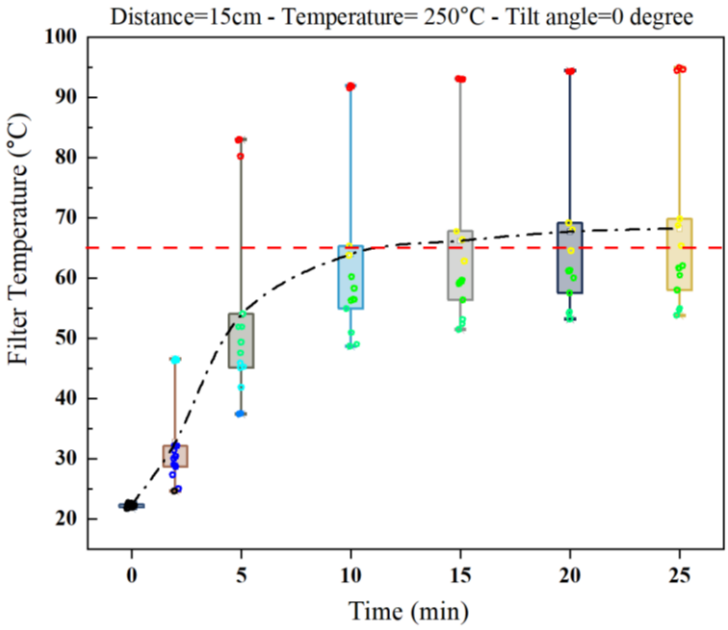

(a)

Figure 5.25a. Temperature distribution across the filter using one ceramic heater set to 250 ℃, at D= 15 cm and $\alpha = 0°$ with transparent gates

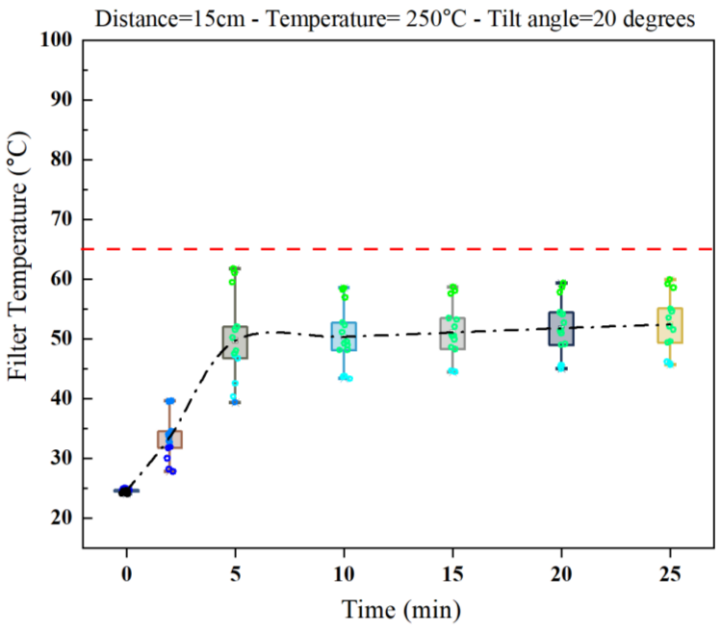

(b)

Figure 5.25a. Temperature distribution across the filter using one ceramic heater set to 250 ℃, at D= 15 cm and $\alpha = 20°$ with transparent gates

Figures 5.26a and 5.26b illustrate the temperature variation across the filter at a distance of 10 cm and a tilt angle of 20 °, with setpoint temperatures of 300 ℃ and 350 ℃, respectively. At a setpoint temperature of 300 ℃, the filter temperature remained nearly constant after 10 minutes and did not reach the target disinfection threshold of 65 ℃. In contrast, increasing the setpoint temperature to 350 ℃ led to a maximum filter temperature of 90 ℃, while the minimum remained below 65 ℃ over the 17-minute test duration. Similar temperature behavior was observed in other different configurations, which are presented in Figures 5.27- 5.29.

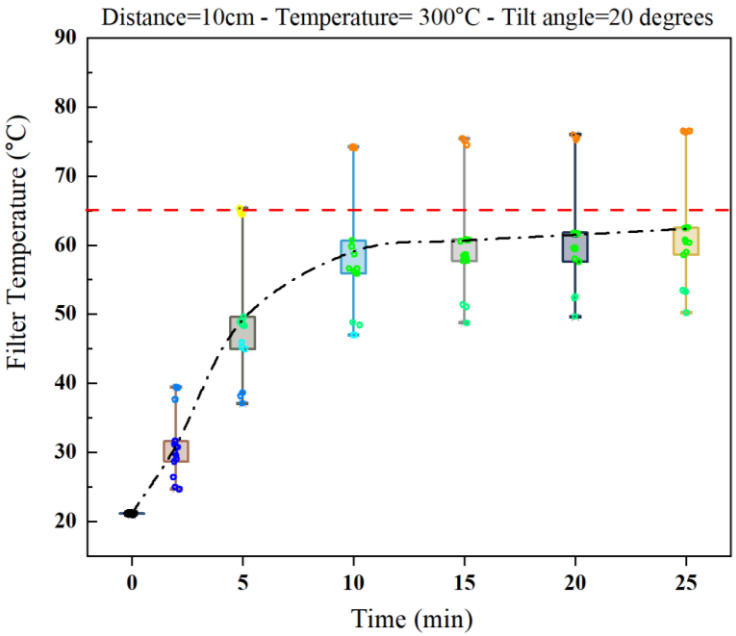

Figure 5.26a. Temperature distribution across the filter using one ceramic heater set to 300 ℃, at D= 10 cm and $\alpha = 20°$ with transparent gates

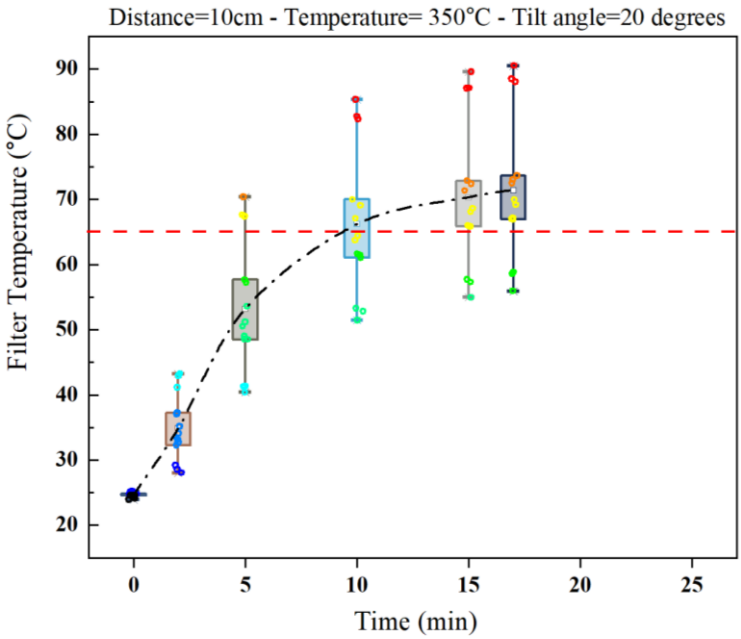

Figure 5.26b. Temperature distribution across the filter using one ceramic heater set to 350 ℃, at D= 10 cm and $\alpha = 20°$ with transparent gates

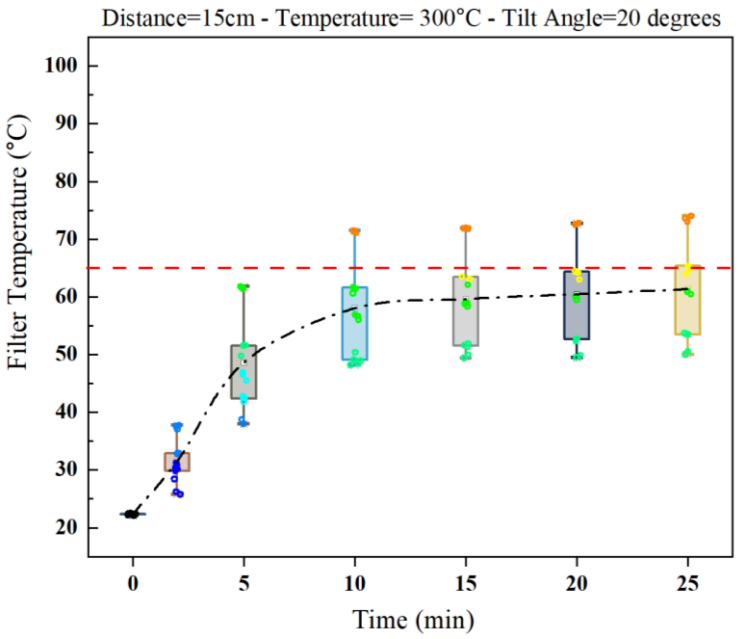

(a)

Figure 5.27a. Temperature distribution across the filter using one ceramic heater set to 300 ℃, at D= 15 cm and $\alpha = 20°$ with transparent gates

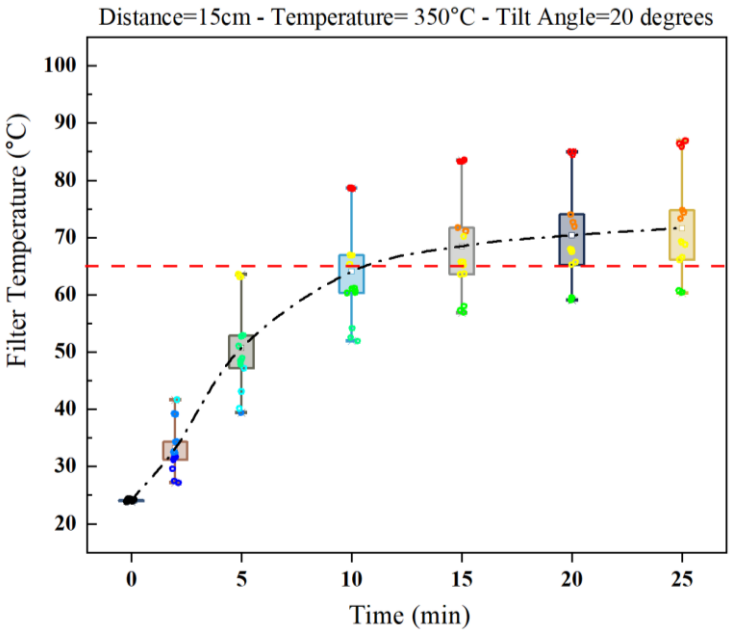

(b)

Figure 5.27b. Temperature distribution across the filter using one ceramic heater set to 350 ℃, at D= 15 cm and $\alpha = 20°$ with transparent gates

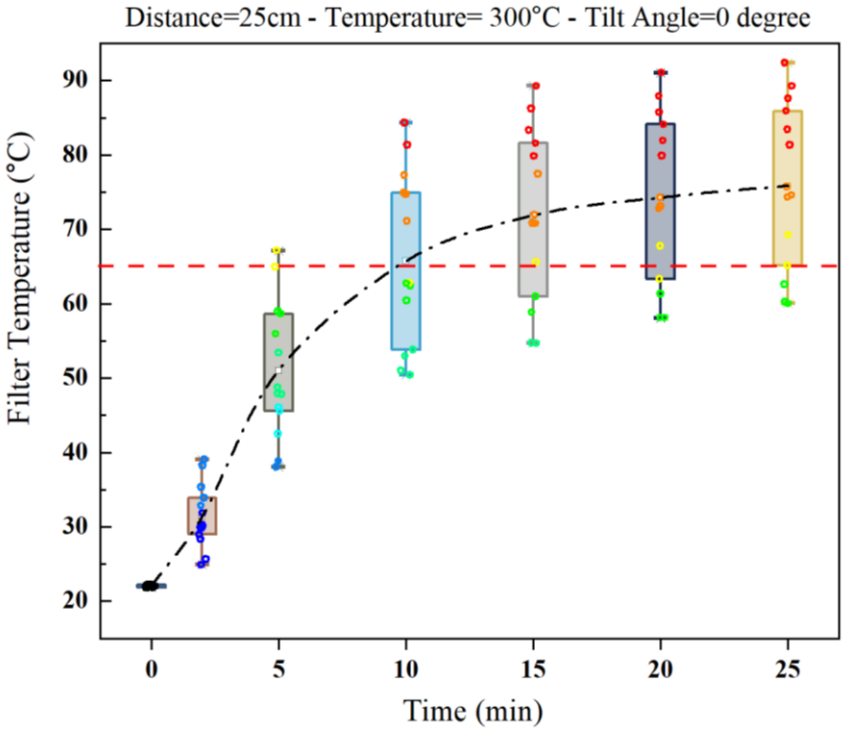

Figure 5.28. Temperature distribution across the filter using one ceramic heater set to 300 ℃, at D= 25cm and $\alpha = 0°$ with transparent gates

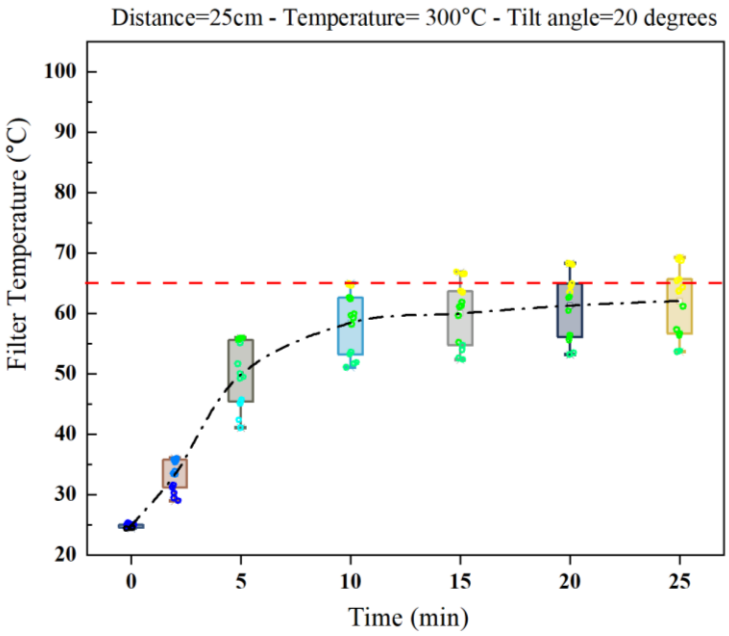

(a)

Figure 5.29a. Temperature distribution across the filter using one ceramic heater set to 300 ℃, at D= 25 cm and $\alpha = 20°$ with transparent gates

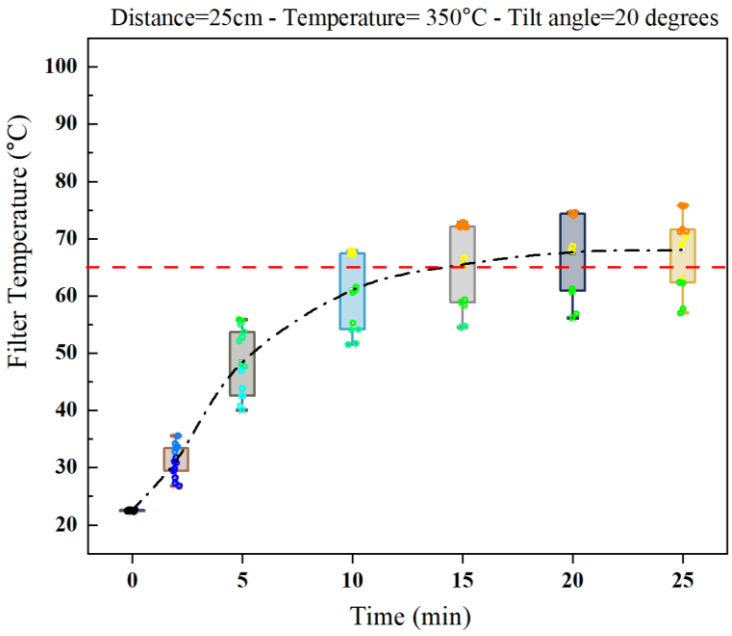

(b)

Figure 5.29b. Temperature distribution across the filter using one ceramic heater set to 350 ℃, at D= 25 cm and $\alpha = 20°$ with transparent gates

At the end, the results indicate that when a single ceramic heater is positioned in front of the filter without any auxiliary reflector to enhance radiation, the filter surface fails to reach the target disinfection temperature of 65 ℃.

Therefore, to achieve more uniform heating and ensure disinfection, an additional ceramic heater is recommended on the backside of the filter.

5.6.1 Impact of Dual Ceramic Heaters in a Transparent-Gates Duct Configuration on the System Performance

In this section, the effect of using two ceramic heaters at both side of the filter, is evaluated under identical conditions, including setpoint temperature, tilt angle, and heater-filter distance. In Figure

5.30 the schematic layout of the unit with two ceramic heaters positioned in front of the filter is presented.

In these tests, the selected setpoint temperatures for the heaters were 180 ℃, 200 ℃, 220 ℃. Due to energy dissipation to the surrounding environment, the maximum temperature of the ceramic heaters did not exceed 230°C during the tests, indicating that the system reached a thermal equilibrium with its surroundings. Consequently, the maximum setpoint temperature for these tests was limited to 220 ℃. Different configurations are listed in Table 5.2.

Table 5.2. Test Parameters for Dual Ceramic Heater Configuration

Distance (cm)	Tilt Angle (degree)	Ceramic heaters' temperature
10	0	180
15	10	200
25	20	220
35		

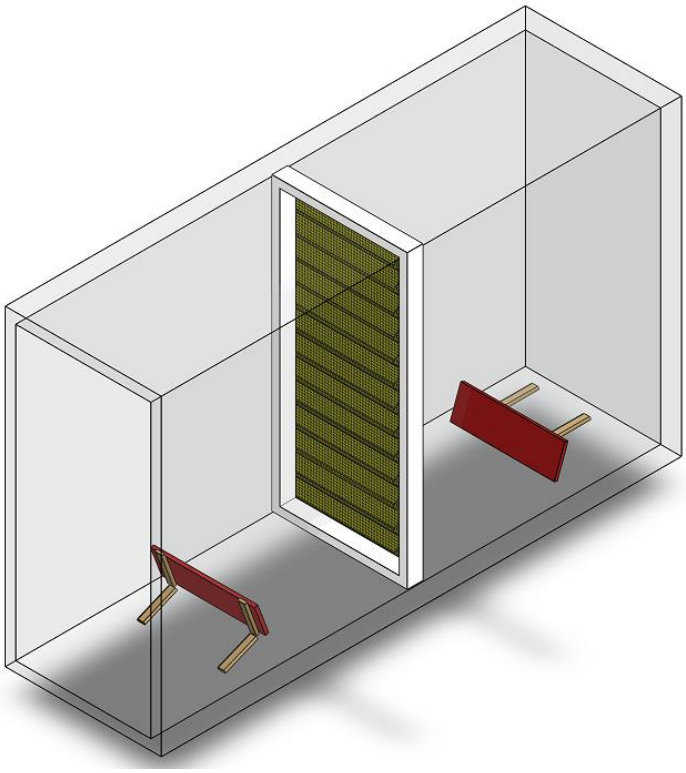

Figure 5.30. Schematic representation of the test duct setup used for evaluating two ceramic heaters performance in a duct without aluminum foil-covered gates.

5.6.1.1 Evaluation of Temperature Distribution and System Performance at $\alpha = 0$ °

Figure 5.31 illustrates box plot of the temperature distribution across the filter at D=10 cm, $\alpha = 0$ ° and setpoint temperature of 180 ℃ for both ceramic heaters. It was seen that the maximum temperature over the filter exceeded 93.0 ℃ after 3 minutes, while the minimum temperature was 34 ℃. When the distance was increased to 15 cm (Figure 5.32), even after 25 minutes of operation, the minimum filter temperature failed to reach the target disinfection threshold of 65 ℃.

However, regarding Figure 5.33, when the setpoint temperature was increased to 200 ℃ at D=15 cm and $\alpha = 0$ °, the maximum temperature reached 96 ℃, but the minimum temperature remained at only 43.0 ℃.

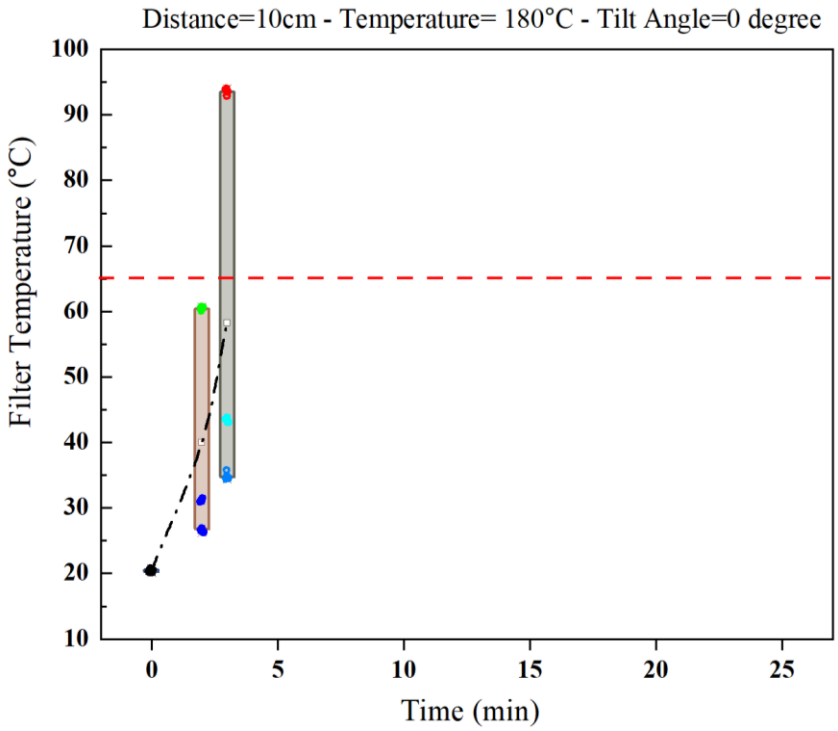

Figure 5.31. Temperature distribution across the filter using two ceramic heaters set to 180 ℃, at D= 10 cm and $\alpha = 0\,^{\circ}$ with transparent gates

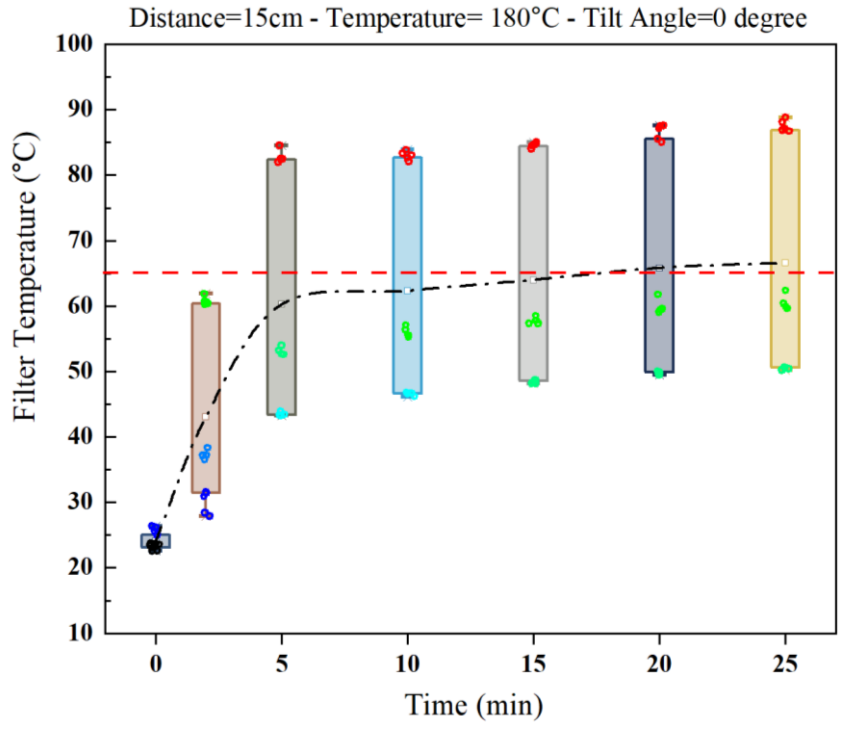

Figure 5.32. Temperature distribution across the filter using two ceramic heaters set to 180 ℃, at D= 15 cm and $\alpha = 0\,^{\circ}$ with transparent gates

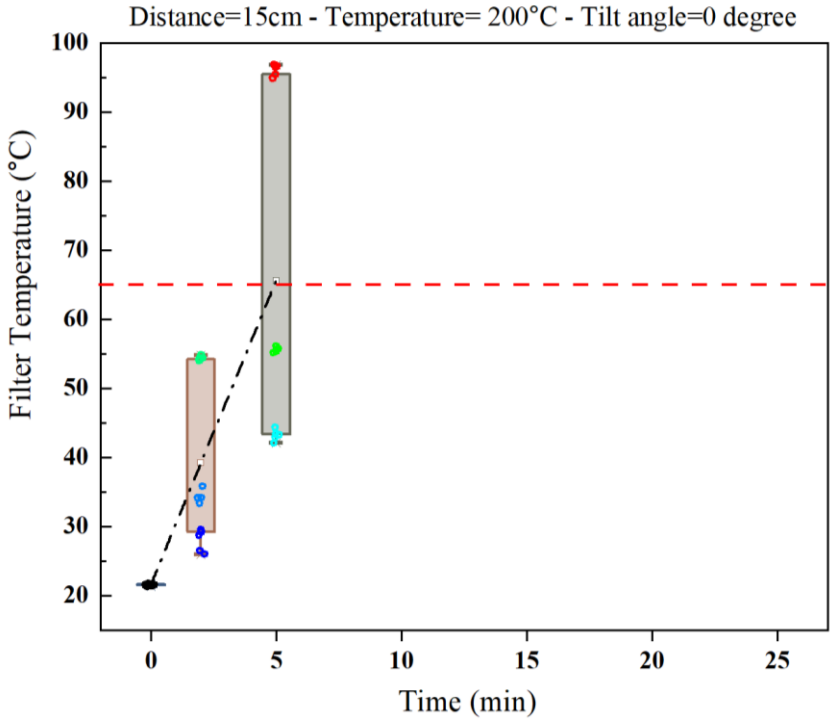

Figure 5.33. Temperature distribution across the filter using two ceramic heaters set to 200 ℃, at D= 15 cm and $\alpha = 0\,^{\circ}$ with transparent gates

Temperature variation over the filter at D= 25 cm, $\alpha = 0\,^{\circ}$ and setpoint temperature of 200 ℃ and 220 ℃ are provided in Figures 5.34a and 5.34b, respectively. The results indicate that a setpoint temperature of 200 ℃ is insufficient for effective disinfection, as the minimum filter surface temperature remained below 65 ℃ even after 25 minutes of heating. However, by increasing the setpoint temperature to 220 ℃, the filter's minimum surface temperature reached 65 ℃ after 15 minutes. Considering the required disinfection exposure time of 10 minutes and with a maximum surface temperature of 95 ℃, the filter was successfully disinfected after 25 minutes.

The total electrical energy consumption measured during this period was 0.10 kWh, and the maximum temperature difference across the filter surface was approximately 24 ℃.

Although disinfection was achieved under this configuration, the distance between the filter and ceramic heaters, as well as the tilt angle, were increased to reduce the temperature difference across the filter surface.

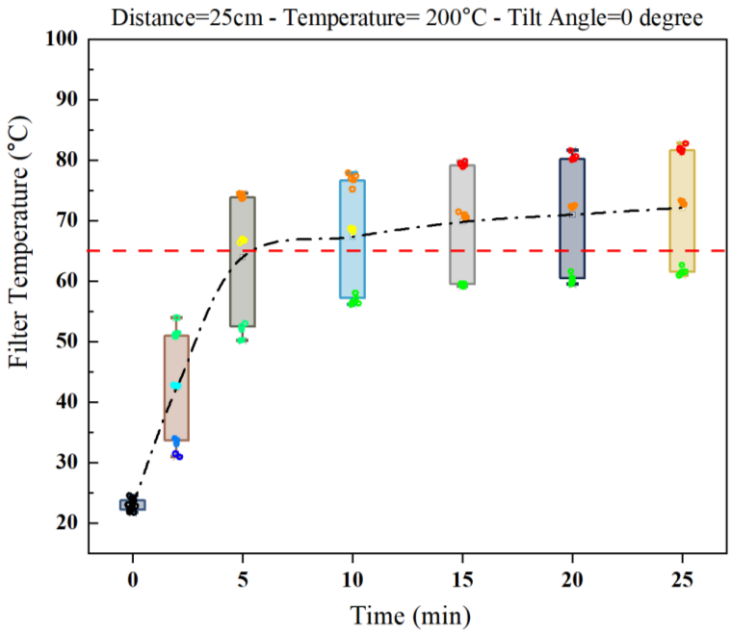

Figure 5.34a. Temperature distribution across the filter using two ceramic heaters set to 200 ℃, at D= 25 cm and $\alpha = 0°$ with transparent gates

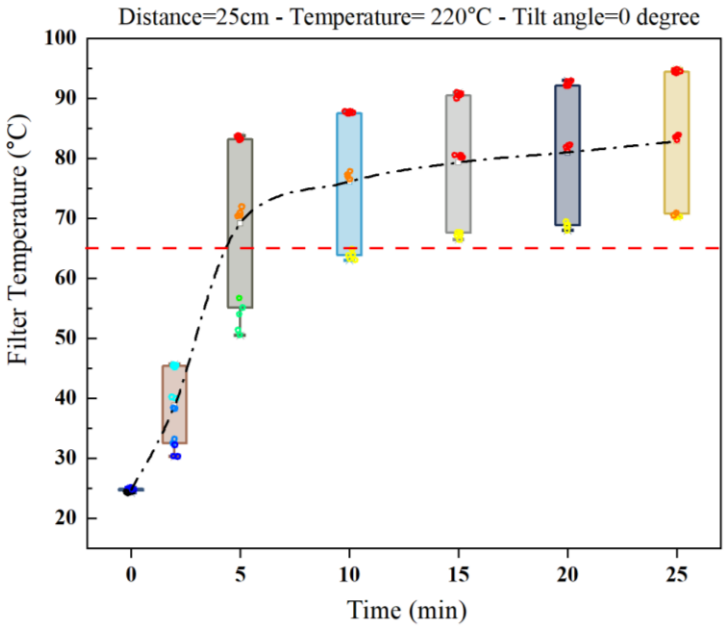

Figure 5.34b. Temperature distribution across the filter using two ceramic heaters set to 220 ℃, at D= 25 cm and $\alpha = 0°$ with transparent gates.

Figure 5.35 illustrates the temperature variation at D= 35 cm and a setpoint temperature of 220 ℃ at $\alpha = 0°$. As shown in Figure 5.36, the filter reached the disinfection threshold during 7 minutes. Despite the greater distance, the minimum temperature rose to 65 °C more quickly than at D=25 cm. Disinfection was therefore achieved after 17 minutes of operation, with a total electrical energy consumption of 0.09 kWh and a maximum temperature difference of approximately 8 ℃.

At D = 25 cm, the top region of the filter exhibited the lowest temperature. By increasing the distance to 35 cm, a larger portion of the filter surface, particularly the upper area, became exposed to the emitted radiation. As a result, temperature uniformity improved, and the heating of the filter to the target disinfection temperature was facilitated.

This suggests that even at these relatively larger distances, the ceramic heater is capable of transferring sufficient heat to the filter surface to maintain the required temperature for disinfection.

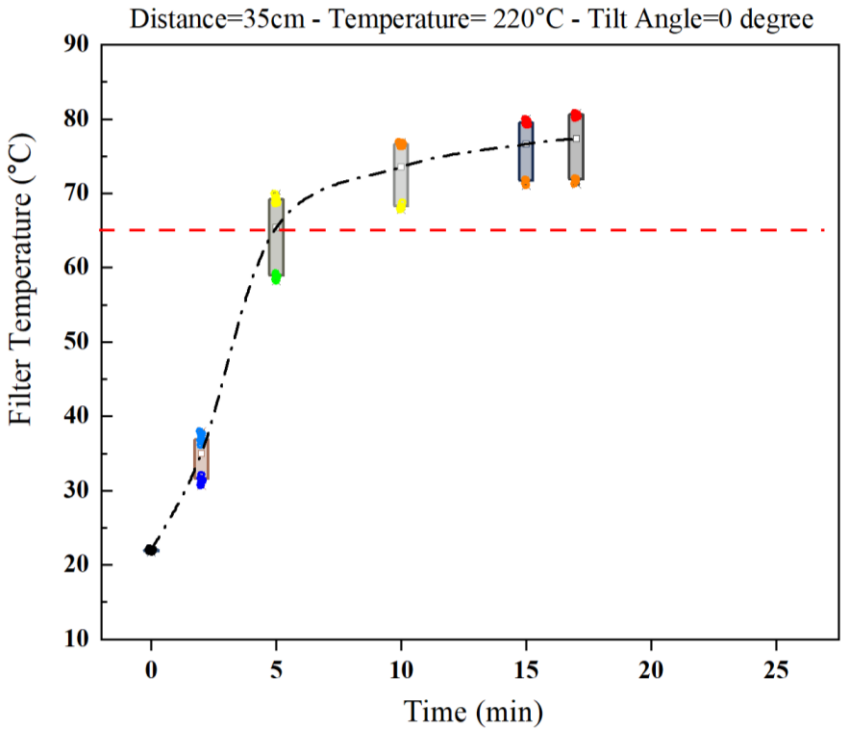

Figure 5.35. Temperature distribution over the filter over time using two ceramic heaters with temperature of 220°C a distance of 35 cm with 0 ° tilt angle in a duct with transparent gates.

5.6.1.2 Evaluation of Temperature Distribution and System Performance at $\alpha = 10\,°$ and $\alpha = 20\,°$

Regarding the effect of tilt angle, figure 5.36a and 5.36b demonstrates the temperature distribution over the filter at D=25 cm, setpoint temperature of 220 ℃ , and $\alpha = 10\,°$ and $\alpha = 20\,°$, respectively. Furthermore, the temperature distributions at a distance of 35 cm, with the same setpoint temperature (220 ℃) and tilt angles of $\alpha = 10\,°$ and $\alpha = 20\,°$, are presented in Figures 5.37a and 5.37b, in turn.

As can be seen from the given figures, at a distance of 25 cm, increasing the tilt angle from $\alpha = 10\,°$ to $\alpha = 20\,°$ reduced the temperature difference across the filter. At 35 cm, the distributions became even more compact, with both tilt angles showing improved uniformity compared to 25 cm. However, the difference between $\alpha = 10\,°$ and $\alpha = 20\,°$ was not significant at this larger distance.

Overall, while disinfection was achieved at both D=25 cm and D=35 cm, the maximum filter temperatures were lower and more stable at 35 cm, which indicates improved thermal stability and a lower risk of overheating. In contrast, configurations at smaller distances (10–15 cm) or with lower heater power resulted in strong local overheating or incomplete heating, preventing safe disinfection.

Figure 5.38 illustrates the temperature distribution over time across different sections of the filter at a distance of 35 cm, tilt angle of $\alpha = 0\,°$, and a setpoint temperature of 220 ℃. As observed, the temperatures at the front and back surfaces of the filter are nearly identical. The middle and bottom regions exhibit the highest temperature values, whereas the top section shows the lowest temperature, with a temperature difference of approximately 8 ℃.

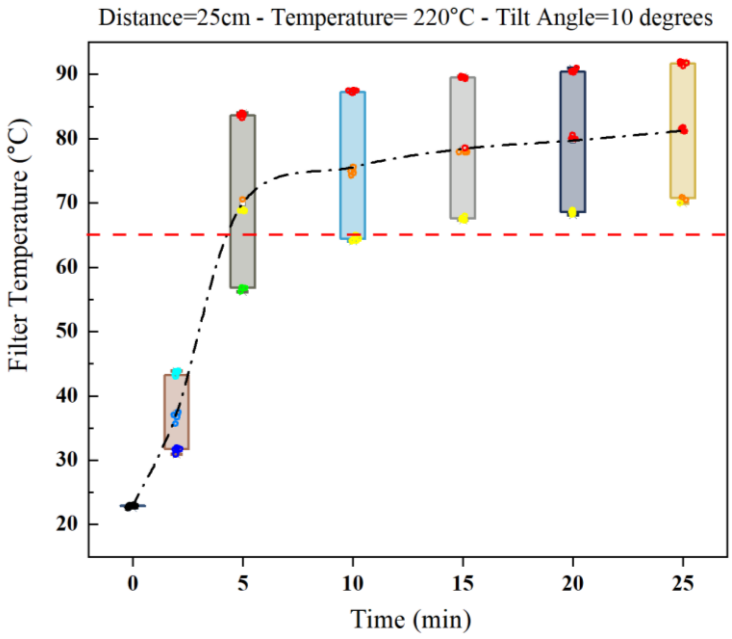

Figure 5.36a. Temperature distribution across the filter using two ceramic heaters set to 220 ℃, at D= 25 cm and $\alpha = 10°$ with transparent gates.

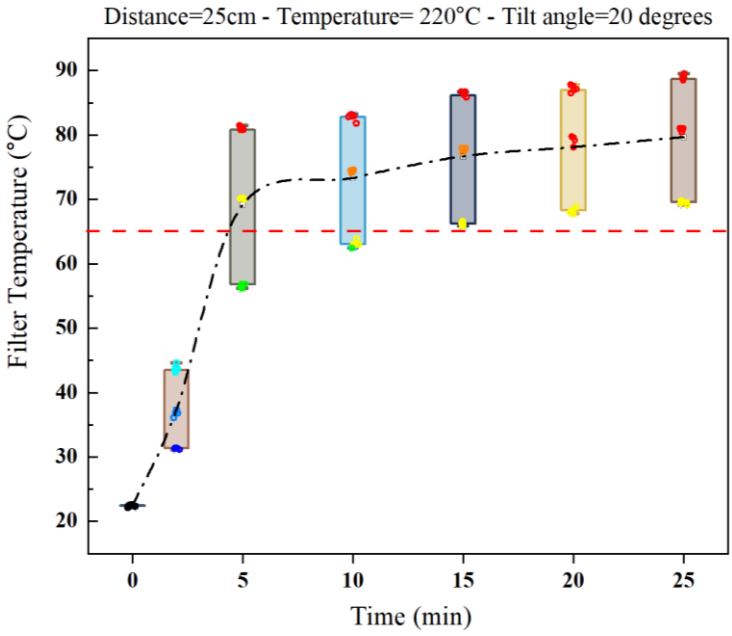

Figure 5.36b. T Temperature distribution across the filter using two ceramic heaters set to 220 ℃, at D= 25 cm and $\alpha = 20°$ with transparent gates.

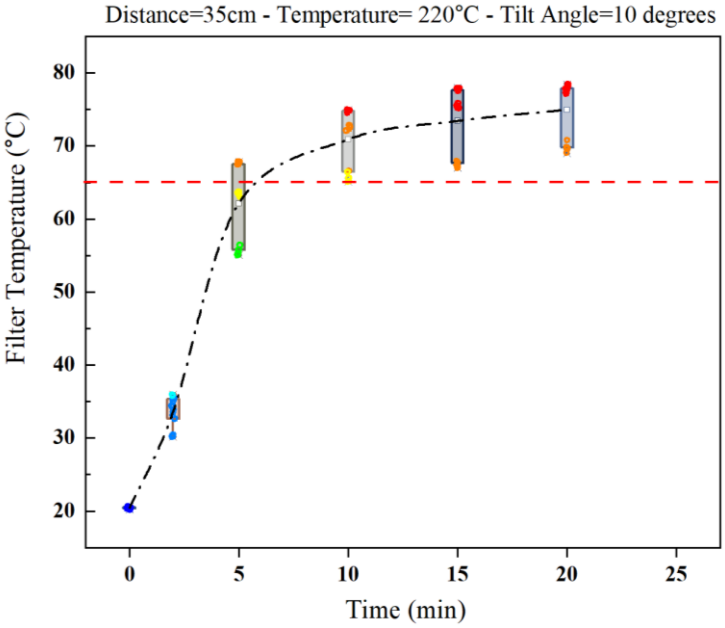

Figure 5.37a. Temperature distribution across the filter using two ceramic heaters set to 220 ℃, at D= 35 cm and $\alpha = 10°$ with transparent gates.

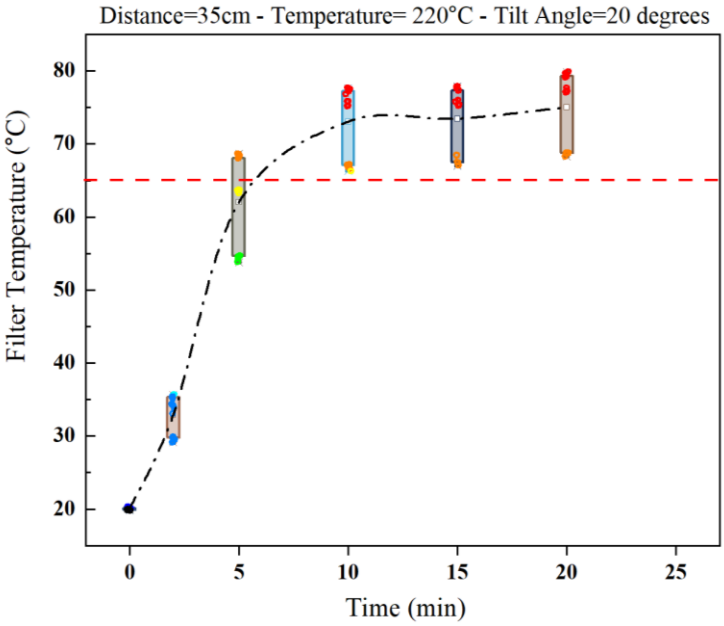

Figure 5.37b. Temperature distribution across the filter using two ceramic heaters set to 220 ℃, at D= 35 cm and $\alpha = 20°$ with transparent gates.

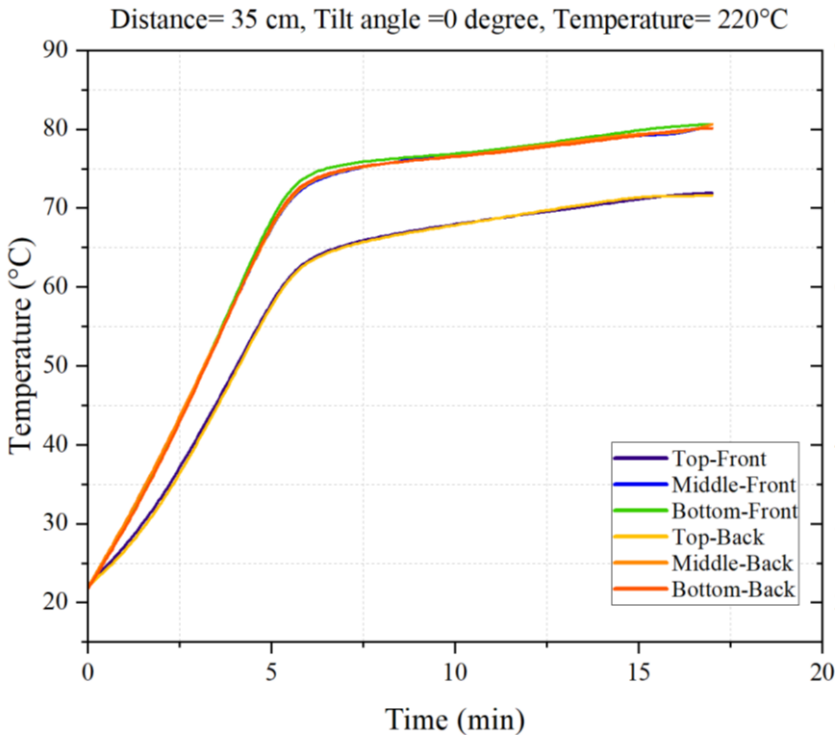

Figure 5.38. Temperature distribution over time across different sections of the filter using two ceramic heaters at $T_{setpoint}$ = 220 ℃, D= 35 cm and $\alpha = 0°$ with transparent gates.

Table 5.3 summarizes the cases in which the filter was successfully disinfected using two ceramic heaters with transparent gates.

Table 5.3. Summary of test configurations that achieved successful filter disinfection using two ceramic heaters when the gates are transparent.

Tilt angle (α) (°)	**Distance (D) (cm)**	**Setpoint temperatures** (℃)	**Minimum temperature** (℃)	**Maximum temperature** (℃)	**Duration ($minutes$)**	**Electrical Energy Consumption (kWh)**
0	25	220	70.2	95.1	25	0.10
	35	220	72.1	80.1	17	0.09
10	25	220	68.3	90.3	20	0.12
	35	220	68.6	77.6	16	0.10
20	25	220	68.4	88.2	22	0.12
	35	220	69.2	80.0	21	0.10

These experiments demonstrate that both the distance between the heaters and the filter, as well as the tilt angle of the heaters, significantly impact the efficiency and temperature uniformity of the filter during disinfection. When the heaters were placed too close (10–15 cm), the filter surface became very hot in some spots while other areas stayed too cool, meaning disinfection could not be achieved safely.

Increasing the distance to 25–35 cm allows the outcome, to reach more uniform temperature distribution without overheating. Adjusting the tilt angle to $\alpha = 10\,°$ or $\alpha = 20\,°$ helped reduce temperature differences at shorter distances, but at larger distances the effect was less noticeable because the filter was already receiving more uniform radiation.

The total energy consumption and heating duration was also reasonable in the D=25 cm to D=35 cm range, with energy usage between 0.09 kWh and 0.12 kWh and complete disinfection achieved in about 16–22 minutes at 220 ℃.

5.7 Effect of Carbon Coating on the Thermal Performance of the System

To evaluate the effect of filter material on disinfection performance under infrared heating, a carbon-coated filter was employed to examine its impact on the temperature distribution. Figure 5.39 illustrates the two sides of the filter, where one side is coated with carbon while the opposite side consists of polyester fibers.

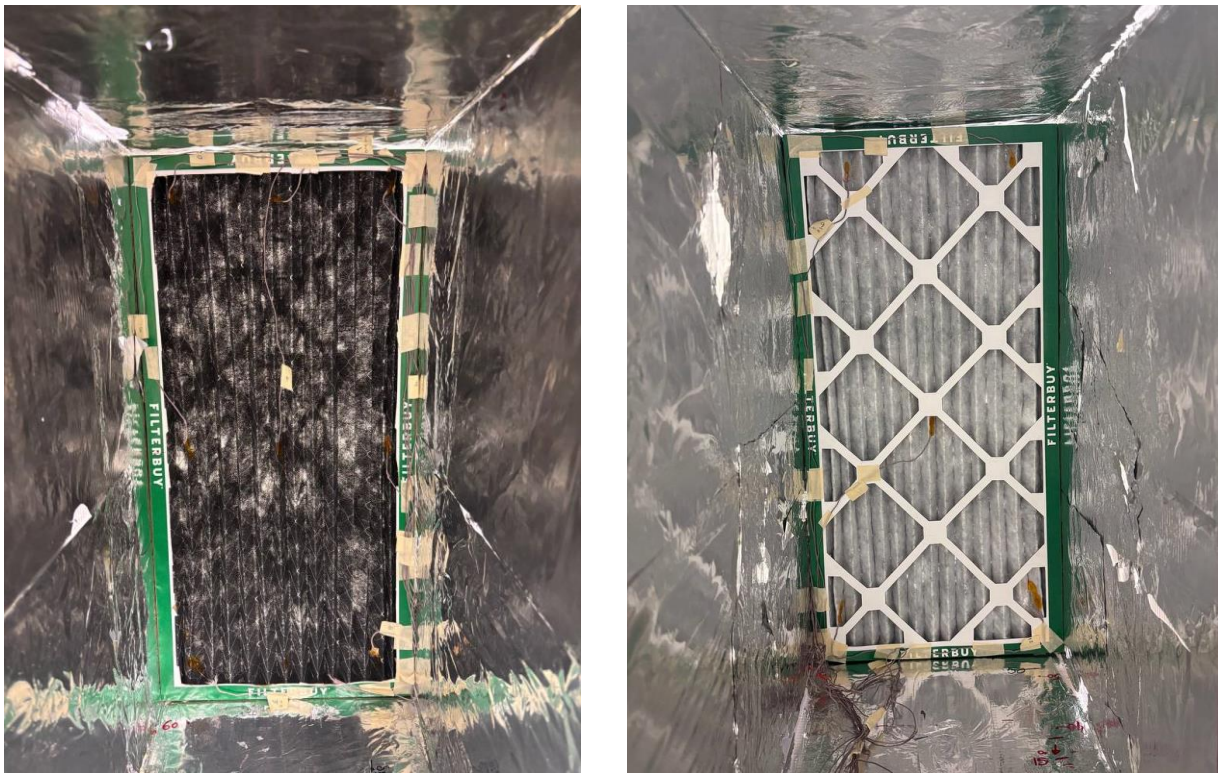

(a) (b)

Figure 5.39. Front and back sides of the pleated filter showing the (a) carbon-coated surface and (b) the polyester fiber surface.

In this experiment, the ceramic heater was used with both aluminum foil -covered gates (one ceramic heater) and transparent gates (two ceramic heaters) to evaluate the effect of carbon coating. The distance between the heater and the filter was set to D = 15 cm for the aluminum-foil-covered gates configuration and D=35 cm for the transparent configuration.

The surface temperatures were measured over time and mapped across the entire filter area to evaluate the influence of the carbon coating on temperature distribution. The results were then analyzed to determine the potential applicability of carbon-coated filters for thermal disinfection purpose.

Figure 5.40a and 5.40b present the temperature distribution over the filter at D=15 cm, $\alpha = 0$ °, and a setpoint temperature of 220 ℃, when the heater was placed facing the carbon-coated and non-carbon coated sides of the filter, respectively. The results showed that when the ceramic heater was positioned in front of the carbon-coated side of the filter, the filter reached to the target temperature of 65 ℃ after 12 minutes, and complete disinfection was achieved within 22 minutes, with a total energy consumption of 0.05 kWh. In contrast, when the uncoated (white) side of the filter was exposed to the heater, the same temperature was achieved after 16 minutes, with full disinfection in 26 minutes and an energy consumption of 0.07 kWh.

Moreover, as illustrated in Figure 5.40, the temperature distribution was noticeably more uniform when the heater faced the carbon-coated surface.

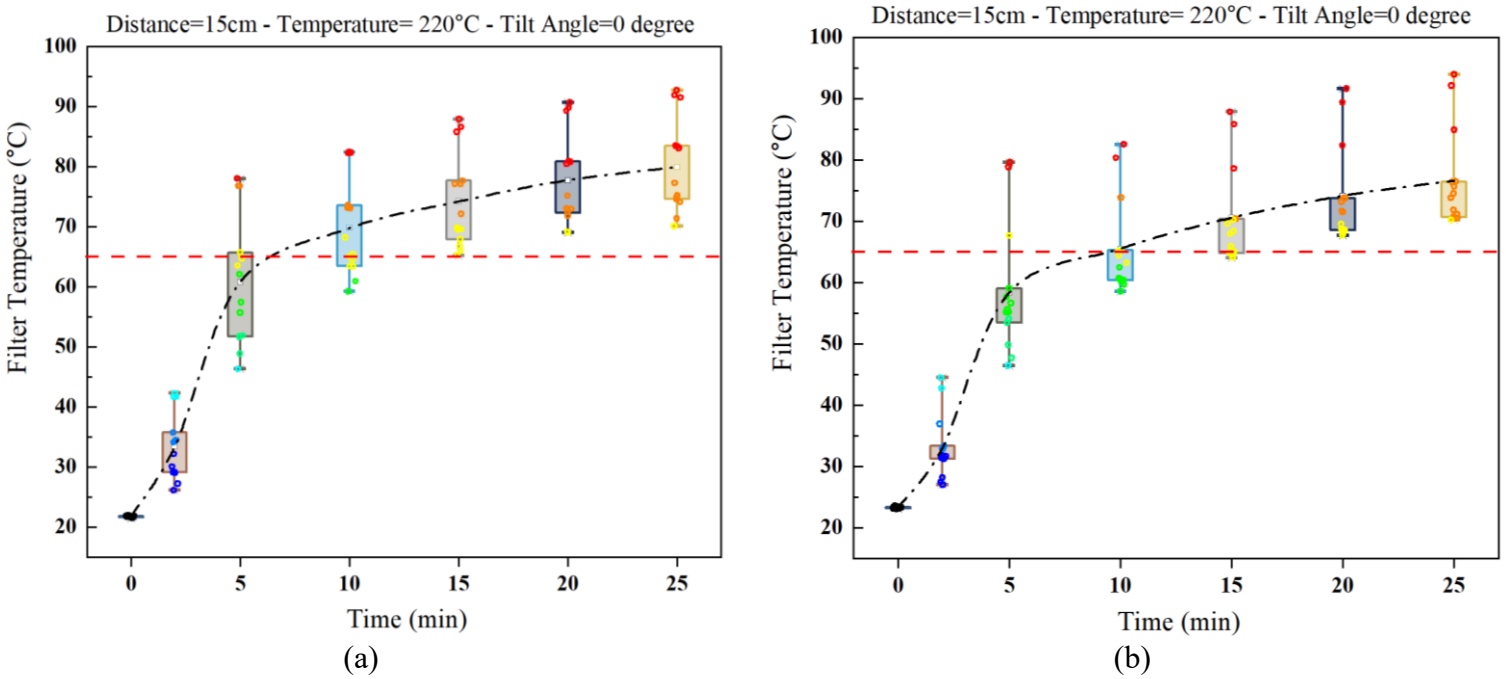

Figure 5.40. Temperature distribution over the filter at D=15 cm, $\alpha = 0$ °, and $T_{setpoint} = 220$ ℃, with the gates covered by aluminum foil. (a) heater facing the carbon-coated side of the filter, and (b) heater facing the uncoated side.

Figure 5.41a and 5.41b illustrate the temperature distribution over the carbon-coated and uncoated sides of the filter at D = 35 cm, $\alpha = 0$ °, and a heater setpoint temperature of 220 ℃ for both ceramic heaters. As observed, the carbon-coated side reached the target temperature of 65 ℃ within 8 minutes, whereas the uncoated side required approximately 15 minutes to achieve the same temperature. After 25 minutes, the carbon-coated surface maintained a more uniform and higher overall temperature compared to the uncoated side. This faster heating of the coated surface suggests that coating both sides of the filter with carbon could further reduce the overall energy consumption of the system.

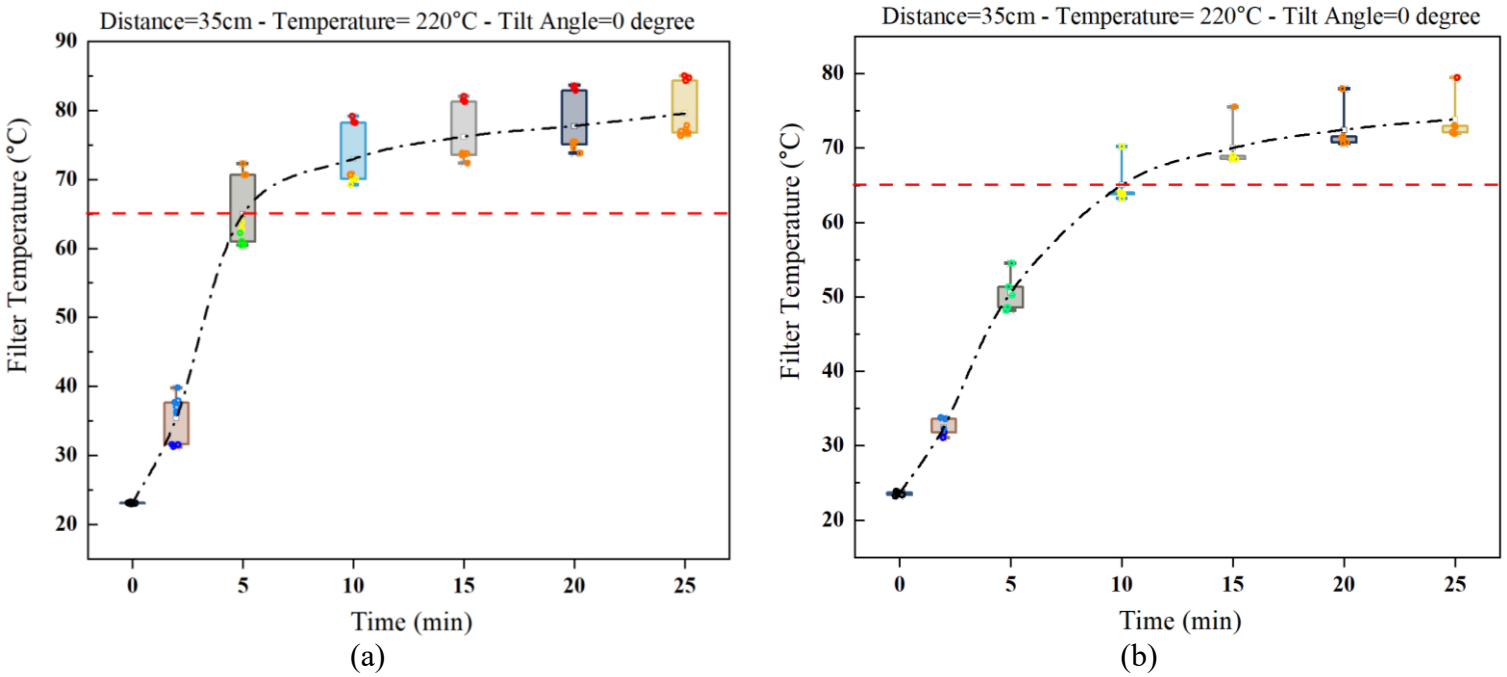

Figure 5.41. Temperature distribution over (a) carbon-coated side of the filter and (b) uncoated side of the filter, at D=35 cm, $\alpha = 0$ °, and $T_{setpoint} = 220$ ℃, with the transparent gates.

In general, the results demonstrated the positive influence of the carbon-coated filter in two key aspects: lower energy consumption and a more uniform temperature distribution across the filter surface compared to the regular polyester filter. This improvement can be attributed to the strong

infrared absorptivity of the carbon coating [83]. To better illustrate this, Figure 5.42 presents a comparison of the temperature distribution across three sections of the filter for both the carbon-coated and regular polyester cases.

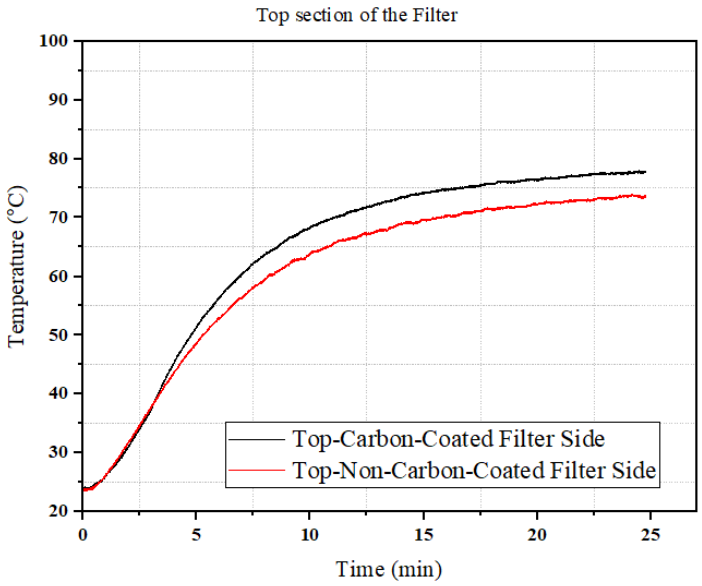

(a)

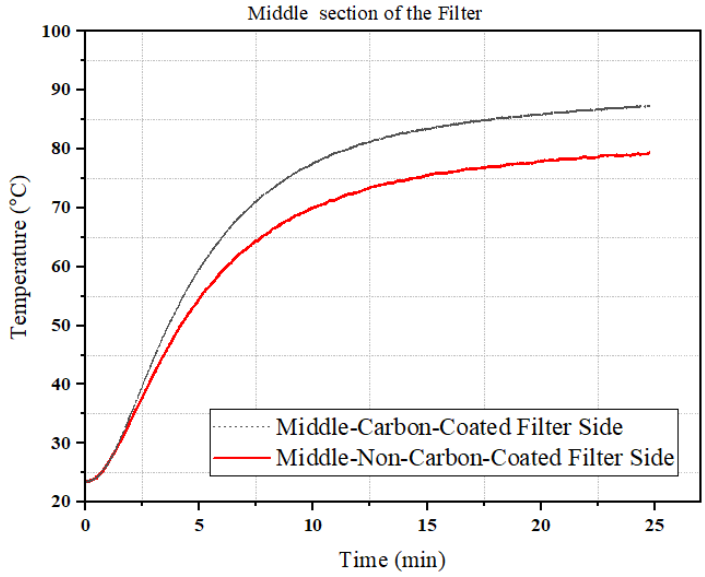

(b)

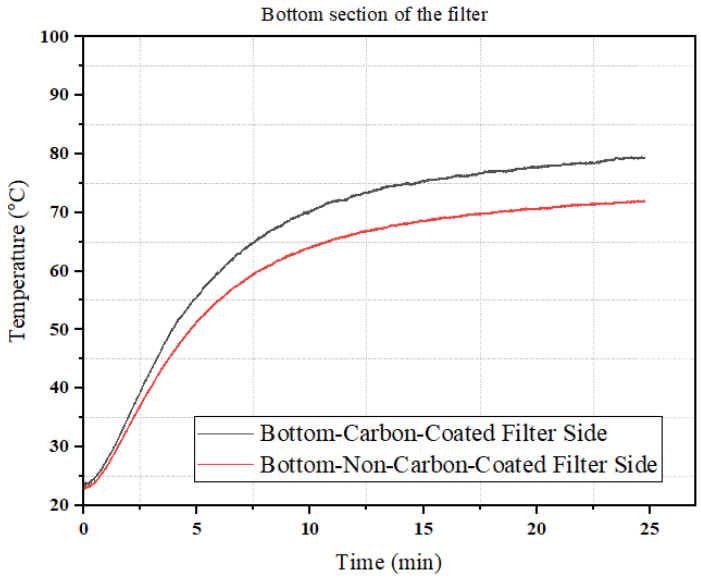

(c)

Figure 5.42. Temperature distribution across three sections of the filter for both the carbon-coated and regular polyester cases at D = 35 cm, $T_{setpoint}$ = 300 ℃, and α = 0 °: (a) top section, (b) middle section, and (c) bottom section.

Although the carbon-coated surface also has a relatively high emissivity [95], the net radiative heat transfer remains directed toward the filter. According to the Stefan–Boltzmann law, radiative emission increases with the fourth power of the absolute temperature ($q \propto T^4$). Therefore, the radiation emitted by the ceramic heater is several times greater than the energy re-emitted by the filter, as the heater operates at a much higher temperature than the filter surface. This leads to a net energy gain, faster surface heating, and a more uniform temperature field across the filter.

5.8 Comparison between the Experimental Data and the Calculated View Factor

A series of tests was conducted to compare the experimentally measured temperature distribution on pleated HVAC filters with the calculated view factors between the ceramic heater and the filter surface based on theoretical radiative principles. The objective was to assess whether the spatial

temperature variations observed experimentally align with the non-uniform radiative exposure predicted by view factor analysis.

In these experiments, the distance between the ceramic heater and the filter, the tilt angle of the heater, and the heater's setpoint temperature are the variable parameters. In each test, the ceramic heater was first induced to the desired setpoint temperature and then positioned in front of the filter. This approach ensured that the temperature rise on the filter surface was evaluated precisely at the target heater temperature.

To ensure that the ceramic heater reached a stable temperature before being exposed to the filter, an aluminum frame cover was constructed (as shown in Figure 5.43). In this setup, the filter and heater were first positioned in the desired configuration. After that, the cover was placed over the ceramic heater, and the heating controller was activated to heat the unit to the desired setpoint temperature. Once the ceramic heater reached the target setpoint temperature, the cover was removed and the transparent gates were immediately closed. At that point, the surface temperature of the filter was measured.

Since the view factor calculations considered only the direct view factor between the ceramic heater and the filter, the aluminum foil covering the gates was removed. Additional reflections from the foil surfaces would have caused discrepancies between the measured temperature distribution and the radiative behavior predicted by the view factor model.

Figure 5.43. Aluminum frame cover used to stabilize the ceramic heater temperature before exposing the filter.

5.8.1 Dominant Mode of Heat Transfer: Identification the Radiation-Dominant Period

To analyze the experimental measurements with the calculated view factors, it is first necessary to determine the period when radiation was the dominant mode of heat transfer and the influence of natural convection was minimal.

Figure 5.44 shows the temperature variation at the top, middle, and bottom sections of the filter when the ceramic heater was operated at a setpoint temperature of 200 ℃, with a tilt angle of $\alpha = 20\ °$ and a distance of 10 cm. At the very early stage (0 – 1 minute), the temperature over the filter increases sharply, especially at the bottom section of the filter. This sharp rise shows that radiation is the dominant mode of heat transfer during the first minute. After about a minute, the temperature

growth slows down. This demonstrates that although radiation continues to contribute to heating the filter, the influence of natural convection gradually becomes more dominant.

After around five minutes, buoyancy-driven flow plays a more significant role, and the temperature increase becomes gradual and approaches a steady trend. Therefore, the first minute clearly represents a radiation-dominant regime, and it is the most reliable period to evaluate the measured temperature against the view factor calculations.

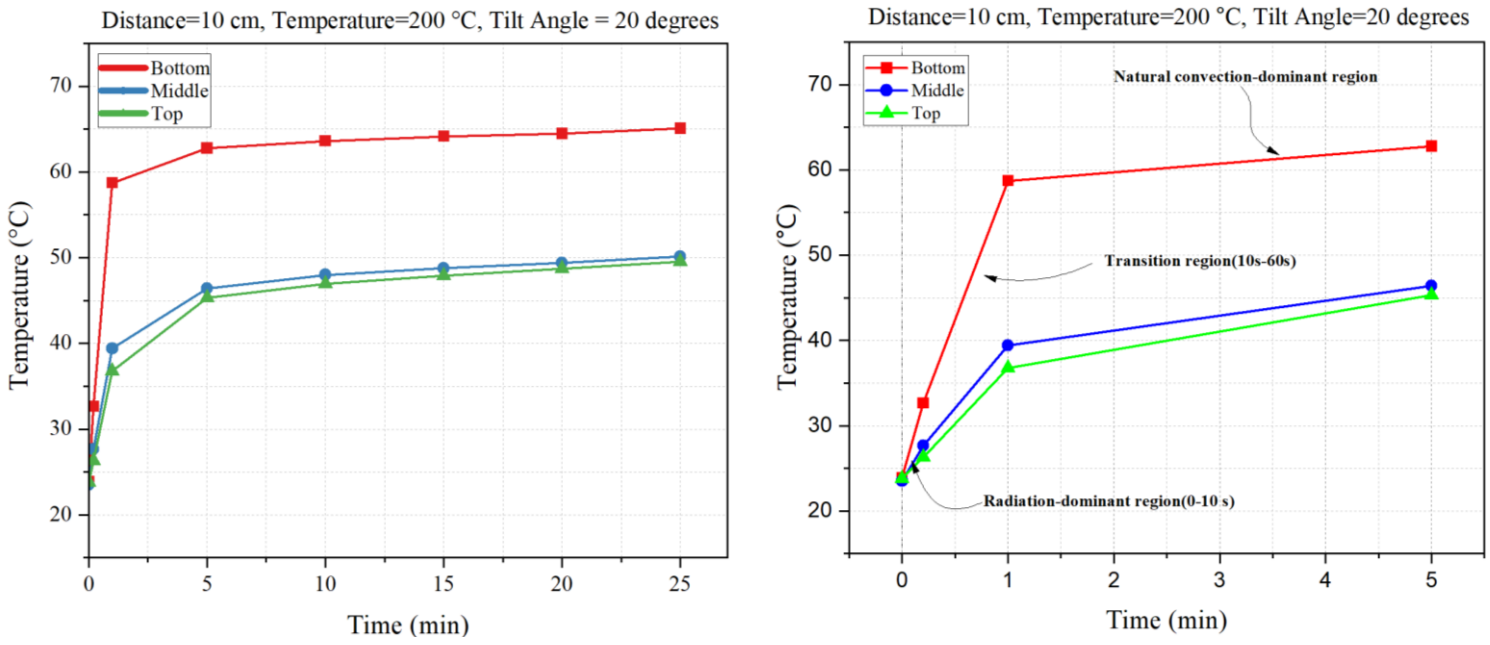

Figure 5.44. Temperature variation at the top, middle, and bottom sections of the filter with transparent gates and the ceramic heater stabilized at the setpoint temperature before exposure (D = 10 cm, $T_{set-point}$ = 200 °C, α = 20°): (a) full heating period; (b) zoomed-in view of 1–5 minutes.

Another way to determine in which period radiation is the dominant mode of heat transfer is to compare the radiative heat flux with the convective heat flux. For this purpose, a mathematical approach was applied during the initial heating stage to evaluate the relative contributions of

radiation and natural convection. The comparison was expressed through the dimensionless ratio $N_{rc} = \frac{q_r}{q_c}$, where q_r is the radiation heat flux and q_c is the convective heat flux.

For this comparison, the filter was considered as a vertical plate and the correlations provided in Incropera et al., Fundamentals of Heat and Mass Transfer [87] were used.

The convective heat flux was estimated using:

$$q_C = h\, A_1\, (T_w - T_\infty) \tag{5.1}$$

Where A_1 is the area of the filter and, h is the external free convection coefficient, determined from the average Nusselt number correlation:

$$\overline{Nu} = \frac{hL}{k} = \mathrm{C}\, {Ra_L}^n \tag{5.2}$$

with the Rayleigh number defined as:

$$Ra_L = \frac{g\beta(T_w - T_\infty)L^3}{\nu\alpha} \tag{5.3}$$

Where T_w is the temperature of the bottom side of the filter and T_∞ is the ambient temperature.

Appropriate constants C and n were selected for laminar $(10^4 \leq Ra_L \leq 10^9)$ and turbulent $(10^9 \leq Ra_L \leq 10^{13})$ regimes. For improved accuracy, the Churchill–Chu correlation was also considered.

For laminar natural convection over a vertical plate $(10^4 \leq Ra_L \leq 10^9)$, the constants are C = 0.59 and $n = 1/4$. For turbulent flow $(10^9 \leq Ra_L \leq 10^{13})$, the corresponding values are C = 0.10 and $n = 1/3$. To cover the entire range of Rayleigh numbers, Churchill and Chu [96] proposed a unified correlation for the average Nusselt number, expressed as:

$$\overline{Nu} = \left\{0.825 + \frac{0.387\ {Ra_L}^{1/6}}{[1 + (0.492/Pr)^{9/16}]^{8/27}}\right\}^2 \quad 5.4$$

This correlation provides reliable predictions for both laminar and turbulent regimes and is widely recommended for engineering applications involving natural convection from vertical plates.

Although Equation 5.4 is suitable for most engineering calculations, slightly higher accuracy can be obtained for laminar flow conditions ($Ra_L \leq 10^9$) using the following correlation [87]:

$$\overline{Nu} = 0.68 + \frac{0.670\ {Ra_L}^{1/4}}{[1 + (0.492/Pr)^{9/16}]^{4/9}} \quad 5.5$$

The net radiative heat exchange between the filter and the ceramic heater surface is expressed as:

$$q_r = \frac{\sigma\ ({T_h}^4 - {T_w}^4)}{\frac{1-\varepsilon_1}{\varepsilon_1 A_1} + \frac{1}{A_2 F_{2-1}} + \frac{1-\varepsilon_2}{\varepsilon_2 A_2}} \quad 5.6$$

where T_h is the ceramic heater temperature, A_2 is the surface area of the ceramic heater, ε_1 and ε_2 are the emissivity's of the filter and ceramic heater, respectively, and F_{2-1} is the view factor from the heater to the filter. For the configuration shown in Figure 6.45 (i.e., D= 10 cm, $\alpha = 20°$), the view factor was calculated as $F_{2-1} = 0.6011$. Based on literature [97], the emissivity of polyester filters was taken as 0.8, and the emissivity of the ceramic heater was assumed to be 0.95 [87,98].

Using these parameters, the radiation and convection heat fluxes were calculated at two-time instants for $t = 10\ s$ and $t = 60\ s$, and their ratio was determined:

- At $t = 10\ s$ ($T_w = 32.0$ ℃, $T_h = 200$ ℃):

$$q_{rad} = 585.06\ w,\ q_c = 16.35w,\ N_{rc} = \frac{q_r}{q_c} = \frac{585.06}{16.35} = 35.78,\ O(N_{rc}) \gg 1$$

$O(N_{rc}) \gg 1$ indicates that radiation overwhelmingly dominates heat transfer.

- At $t = 60\ s$ ($T_w = 58.0$ ℃, $T_h = 200$ ℃):

$$q_{rad} = 537.67\ w,\ q_c = 81.03\ w,\ N_{rc} = \frac{q_r}{q_c} = \frac{537.67}{81.03} = 6.64,\ O(N_{rc}) \cong 1$$

$O(N_{rc}) \cong 1$ shows that radiation and natural convection become comparable.

These results demonstrate that at very early times ($t = 10\ s$), radiation is the dominant mechanism, whereas after about 60 s, convection strengthens and begins to play a comparable role. These calculations indicate that during the early heating stage, when radiation dominates, the temperature rise across the filter can be accurately predicted using the calculated view factor between the heater and the filter.

5.8.2 Experimental Results and Temperature Distribution Analysis

The key parameters used for this verification are summarized in Table 5.4.

Table 5.4. Experimental parameters investigated in this study

Effective parameters	**Values tested**
Setpoint temperature of ceramic heater (℃)	180, 200, 220, 250
Tilt angle of ceramic heater ($\boldsymbol{\alpha}$°)	0, 10, 20
Heater–filter distance (D (cm))	10, 15, 25

Before investigating how variations in distance and tilt angle affect the view factor and resulting temperature distribution, it is necessary first to demonstrate that the experimentally measured temperature field aligns with the theoretical view-factor predictions for a configuration. This gives confidence that the comparisons made in the following sections are reliable.

Figure 5.45a and 5.45b present the temperature rise across the filter sections at $\left(D = 10\ cm, \alpha = 0\ °, T_{set-point} = 250\ ℃, t = 10\ s\right)$ and the corresponding view factors, respectively.

The temperature rise is the temperature difference relative to the initial filter temperature (i.e., 22 °C).

As it is evident from Figure 5.45b, the view factor at the bottom section of the filter is the largest (0.18) compared to the middle (0.0078) and top (0.00055) sections. This corresponds to the maximum temperature rise observed at the bottom (19.7 °C), which is much greater than at the middle (3.0 °C) and top (0.8 °C).

The variation in measured temperatures across the filter sections follows the same trend predicted by the calculated view factors, indicating that the observed non-uniform heating in the experiments primarily arises from geometric effects, thereby strengthening the reliability of the subsequent analysis.

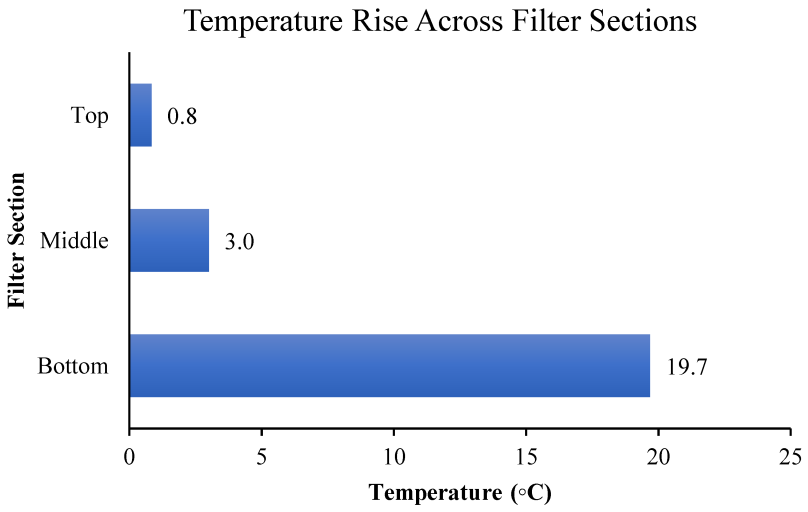

(a)

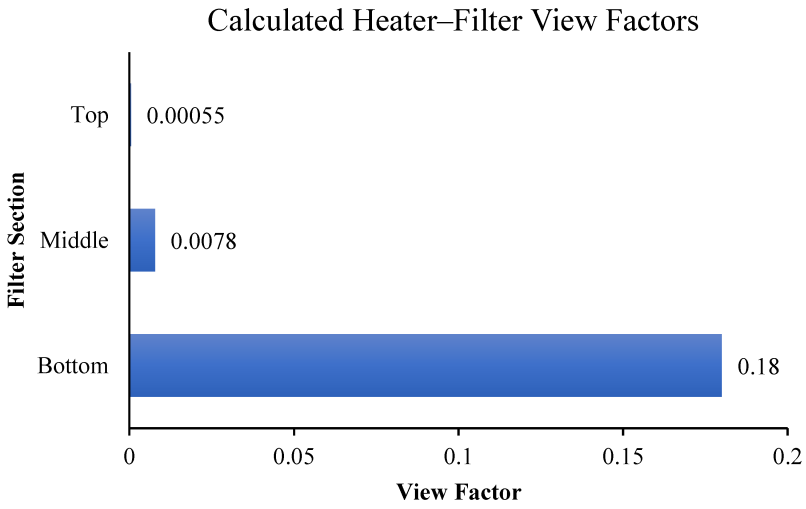

(b)

Figure 5.45. a) Temperature rise across the filter sections at $\left(D = 10\ cm, \alpha = 0\ °, T_{set-point} = 250\ ℃, t = 10\ s\right)$, b) corresponding calculated heater–filter view factors at the same configuration.

In this section, the objective of this analysis is to determine whether the temperature distribution over the filter could be predicted using the view factor approach. For this reason, the results in the following sub-sections are presented at a single setpoint temperature of the ceramic heater.

Since the view factor depends only on geometrical parameters (distance and tilt angle) and not on heater temperature, varying the setpoint would not influence the comparison. Because radiative heat transfer scales with T_h^4, the results are shown at the maximum setpoint temperature ($T_{set-point} = 250\ ℃$) to magnify the radiation effects.

5.8.2.1 Effect of Heater–Filter Distance on Temperature Distribution

The temperature distribution across different sections of the filter and the corresponding view factors between the ceramic heater and the filter at various distances for three tilt angles are illustrated in Figures 5.46-5.48.

As shown in Figure 5.46, the measured temperature rise across the filter and the calculated view factors confirms the strong correlation between radiative exposure and local heating. For example, at shorter distances (D=10 cm), the bottom section of the filter exhibited the largest temperature increase (∼19.7 ℃), while the top section increased by less than 1 ℃ and the middle section rose by 3 ℃ . This non-uniform distribution corresponds directly to the calculated view factors, where the bottom section has the highest value (0.18), and the top and middle sections have negligible values, (0.00055 and 0.0078, respectively).

At greater heater–filter distances, the variation in view factors between the different sections of the filter becomes smaller, which results in a more even temperature distribution. For instance, at a distance of 25 cm, the view factor at the bottom section of the filter is 0.0559 and the temperature rise is about 12.3 ℃, and the temperature of the top section with view factor of 0.0025 increases by around 2.2 ℃. The difference between the top and bottom temperatures decreases from 18.9 ℃ at D=10 cm to about 10.1 ℃ at D=25 cm.

Additionally, the total view factor decreases as the distance between the ceramic heater and the filter increases, and a corresponding reduction in the maximum filter temperature is observed. This trend is expected, since greater distance reduces the fraction of radiative energy intercepted by the filter surface. For example, the total view factor was calculated as 0.5570 at D = 10 cm, 0.4323 at D = 15 cm, and 0.2874 at D = 25 cm. The corresponding temperature increases were 19.7 ℃, 17.9

°C, and 12.3 °C, respectively. This consistent decrease confirms the direct relationship between the view factor and the measured temperature rise across the filter.

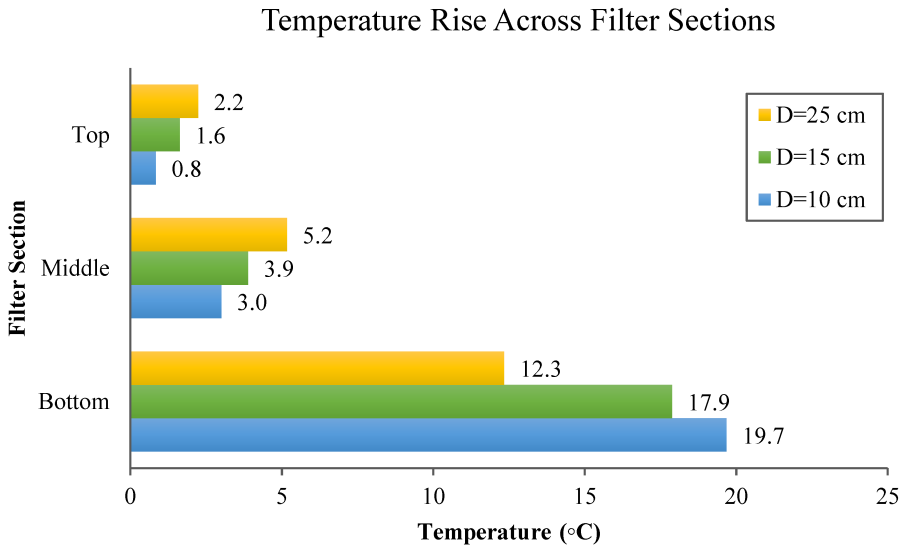

(a)

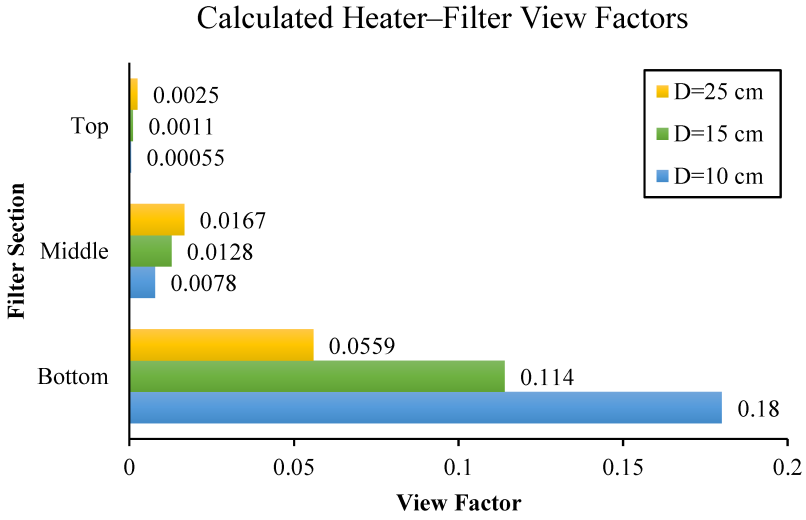

(b)

Figure 5.46. Effect of heater–filter distance on (a) temperature rise across the top, middle, and bottom sections of the filter relative to the initial condition at different distances for $(\alpha = 0\,°, T_{setpoint} = 250\,°C)$ and (b) the corresponding view factors between the ceramic heater and the filter at different distances for $(\alpha = 0\,°)$.

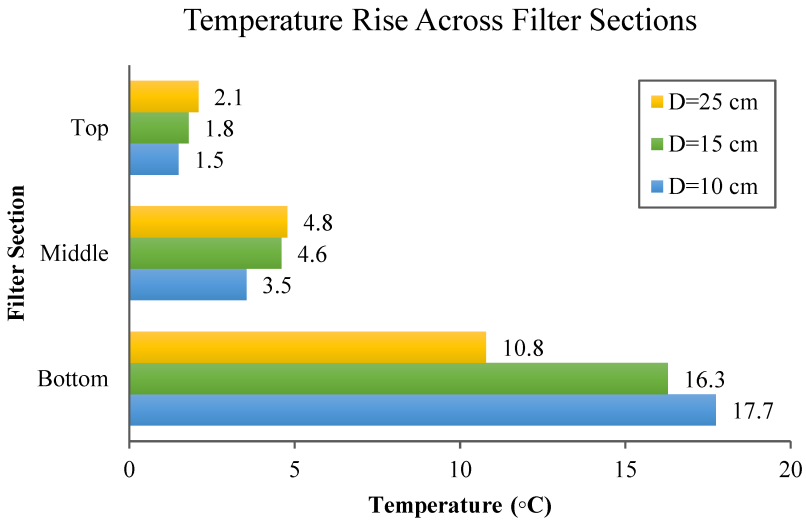

(a)

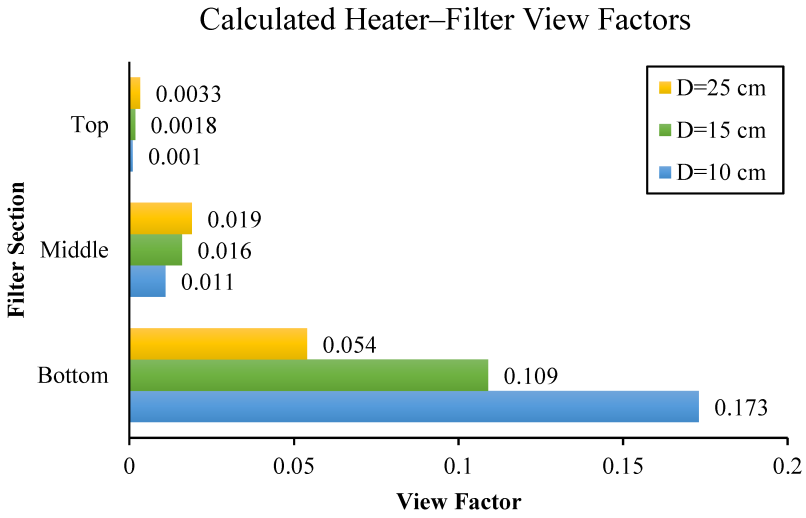

(b)

Figure 5.47. Effect of heater–filter distance on (a) temperature rise across the top, middle, and bottom sections of the filter relative to the initial condition at different distances for $(\alpha = 10\ °, T_{setpoint} = 250\ ℃, t = 10\ s)$ and (b) the corresponding view factors between the ceramic heater and the filter at different distances for $(\alpha = 10\ °)$.

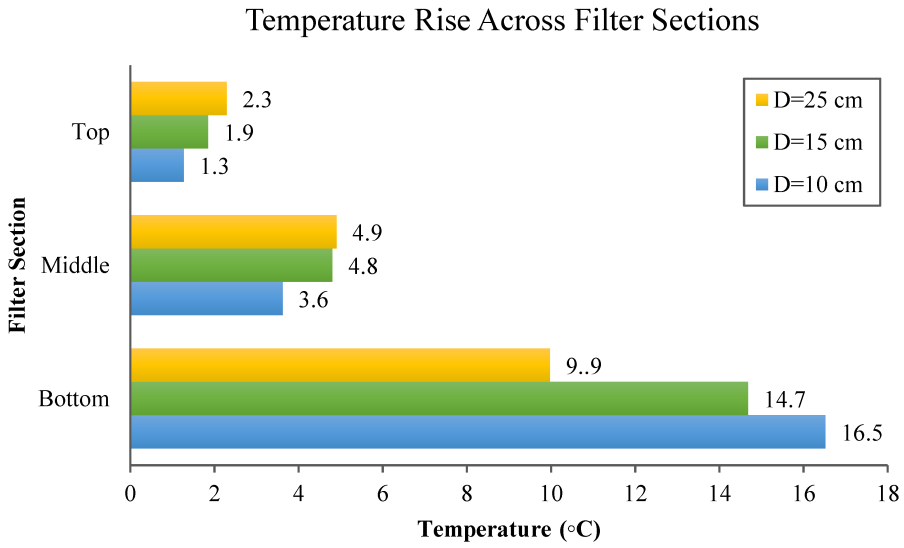

(a)

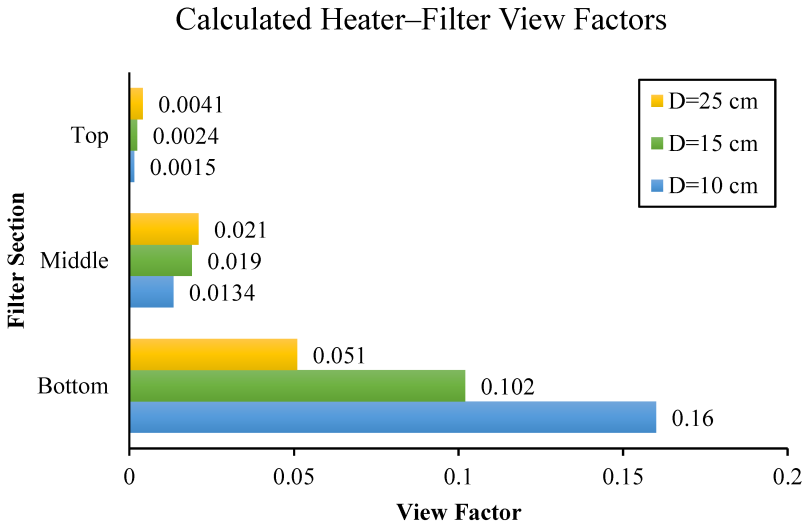

(b)

Figure 5.48. Effect of heater–filter distance on (a) temperature rise across the top, middle, and bottom sections of the filter relative to the initial condition at different distances for $(\alpha = 20\,°, T_{setpoint} = 250\,℃, t = 10\,s)$ and (b) the corresponding view factors between the ceramic heater and the filter at different distances for $(\alpha = 20\,°)$.

The results of this section clearly demonstrate that the experimental temperature distribution is well supported by the calculated view factors. Sections with higher view factors consistently

warmed more than those with lower values. This confirms that view factor analysis can explain the non-uniform heating patterns observed in the experiments.

5.8.2.2 Effect of Heater Tilt Angle on Temperature Distribution

Figures 5.49 to 5.51. illustrate the effect of heater tilt angle on the temperature rise across the filter sections and the corresponding view factors at distances of 10 cm, 15 cm, and 25 cm, respectively, with a setpoint temperature of 250 ℃. From Figure 5.49 b, increasing the tilt angle from 0 ° to 20 ° decreases the view factor at the bottom section (from 0.18 at 0 ° to 0.16 at 20 °). At the same time, the view factors of the middle and top sections increase slightly (from 0.0078 to 0.014 at the middle, and from 0.00055 to 0.0015 at the top).

Moreover, regarding Figure 5.49a, as the tilt angle increases from 0 ° to 20 °, the temperature rise at the bottom decreases from 19.7 ℃ to 16.5 ℃, while the middle and top sections show a slight increase (from 3.0 ℃ to 3.6 ℃ and from 0.8 ℃ to 1.5 ℃, respectively). Therefore, it can be concluded that the temperature rise follows the same trend as the view factor.

As shown in Figure 5.49, both the top and middle sections have very small view factors compared with the bottom section. However, despite their small absolute values, the effect of tilt is more pronounced at the top. At 0 °, the top section has a nearly negligible view factor (0.00055), which increases to 0.0015 at 20 °, representing a rise of about 172 %. In contrast, the middle section increases from 0.0078 to 0.014 from $\alpha = 0$ ° to $\alpha = 20$ °, a roughly 80 % increase.

This difference explains why the temperature rise at the top grows more noticeably (from 0.8 ℃ at $\alpha = 0$ ° to 1.5 ℃ at $\alpha = 20$ °, about 77 % increase) compared to the middle section (from 3.0 ℃ at $\alpha = 0$ ° to 3.6 ℃ $\alpha = 20$ °, near 20 % increase). Thus, while both values remain small in absolute terms, the top section shows a stronger relative response to heater tilt.

Overall, tilting the heater helps spread the radiative energy more evenly across the filter. This suggests that a slight adjustment in the tilt angle can significantly improve temperature uniformity.

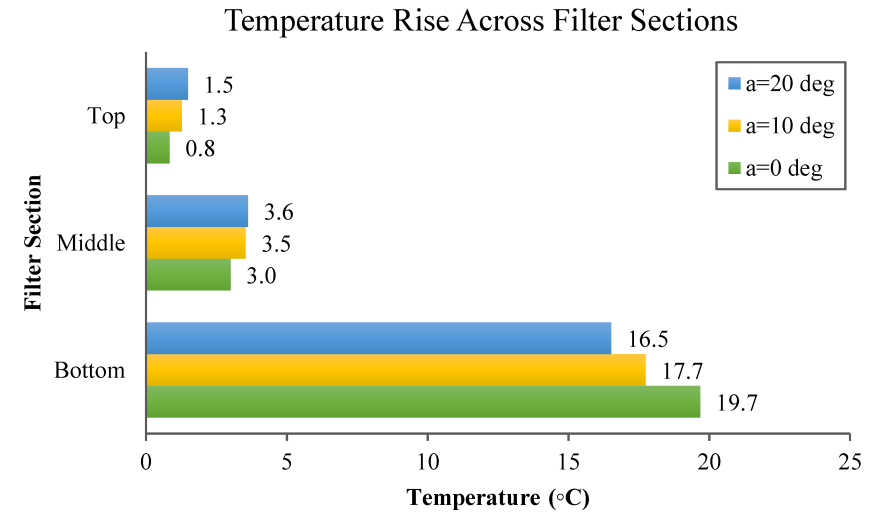

(a)

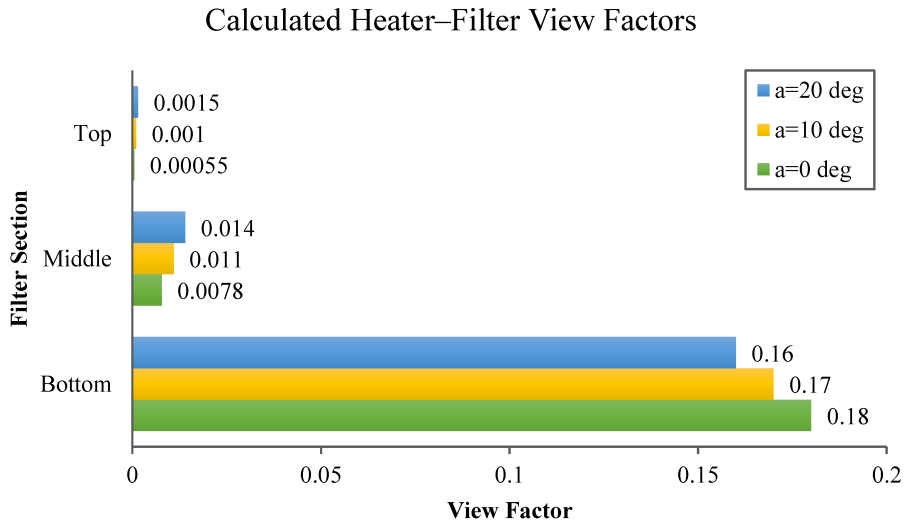

(b)

Figure 5.49. Effect of heater tilt angle on (a) temperature rise across the top, middle, and bottom sections of the filter relative to the initial condition at different distances for $(D = 10\ cm\ , T_{setpoint} = 250\ ℃\ , t = 10\ s)$ and (b) the corresponding view factors between the ceramic heater and the filter at different tilt angle for $(D = 10\ cm)$.

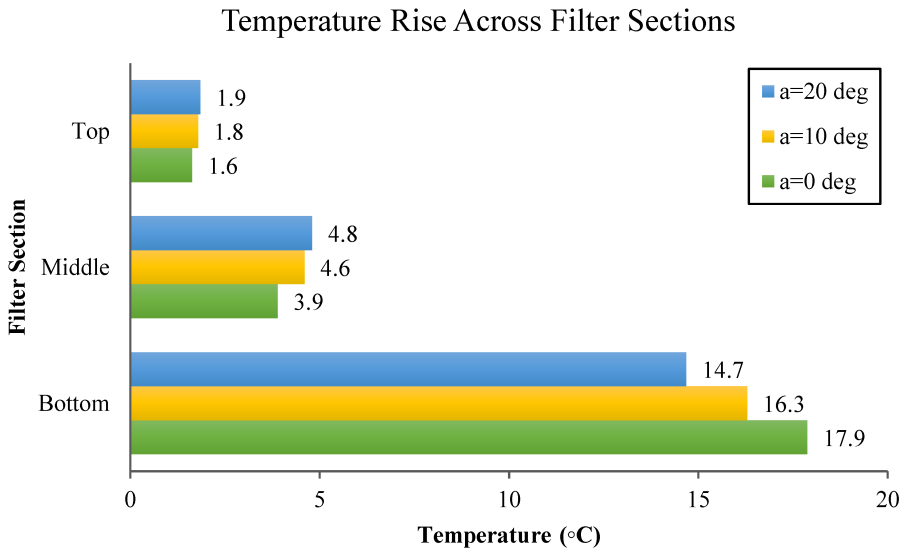

(a)

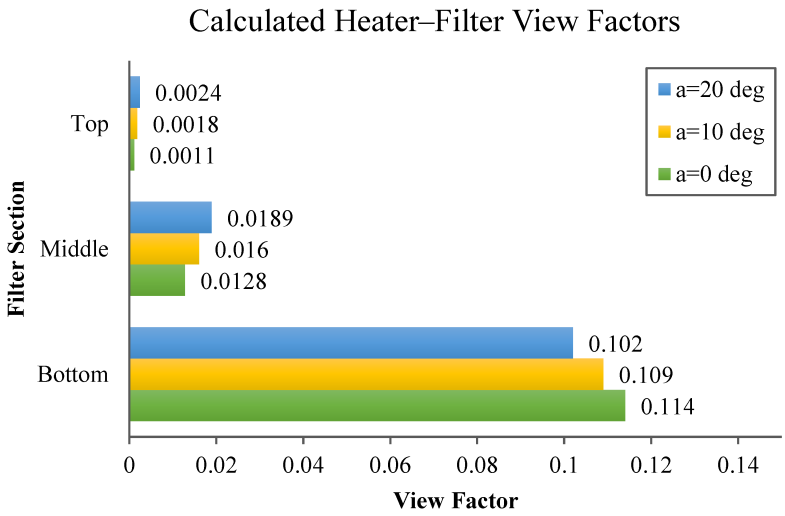

(b)

Figure 5.50. Effect of heater tilt angle on (a) temperature rise across the top, middle, and bottom sections of the filter relative to the initial condition at different distances for $(D = 15\ cm\ , T_{setpoint} = 250\ ℃\ , t = 10\ s)$ and (b) the corresponding view factors between the ceramic heater and the filter at different tilt angle for $(D = 15\ cm)$.

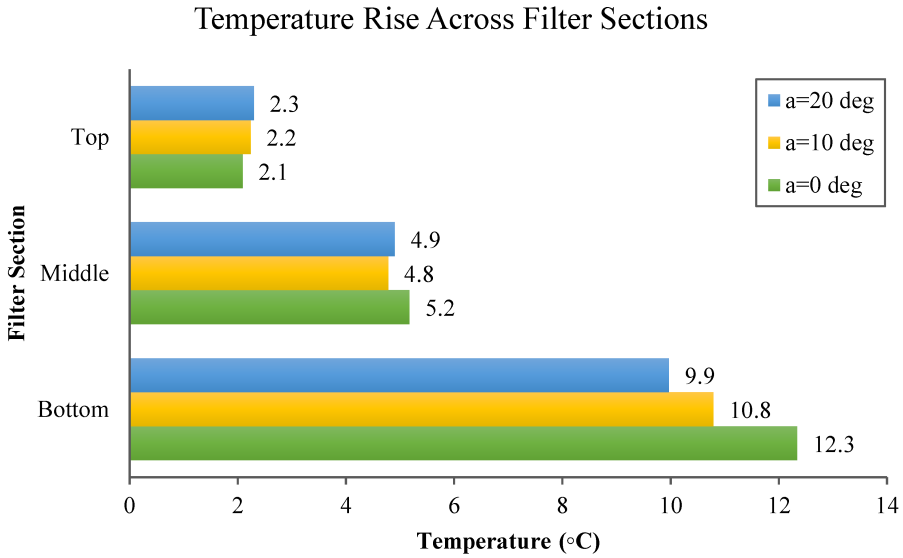

(a)

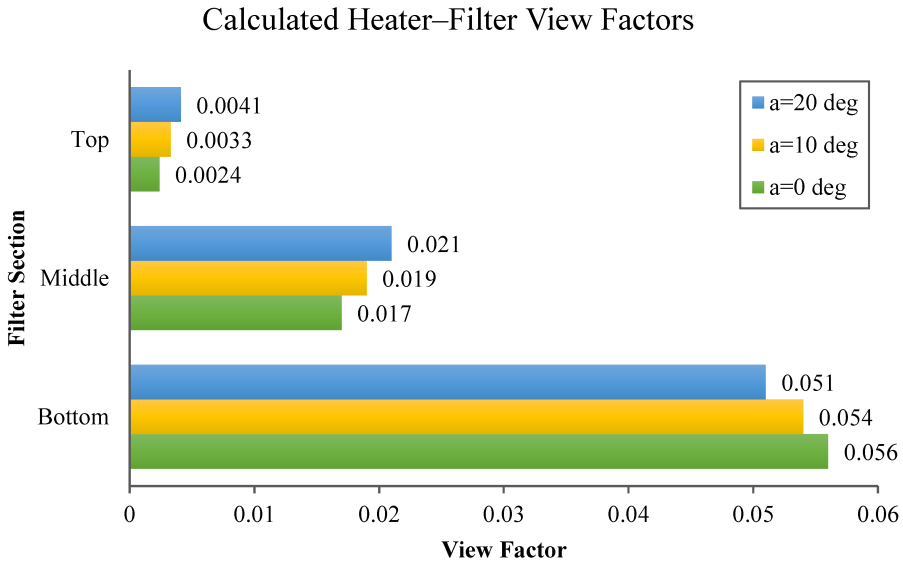

(b)

Figure 5.51. Effect of heater tilt angle on (a) temperature rise across the top, middle, and bottom sections of the filter relative to the initial condition at different distances for $(D = 25\ cm\ , T_{setpoint} = 250\ ℃\ , t = 10\ s)$ and (b) the corresponding view factors between the ceramic heater and the filter at different tilt angle for $(D = 25\ cm)$.

At a D=25 cm (Figure 5.51), the temperature rise in the middle section does not follow the same trend as the view factor. These findings show that when the distance between the heater and filter increases, radiation becomes less dominant and other heat transfer modes play a greater role. At

larger distances, the radiative flux incident on the filter surface spreads over a wider area and becomes weaker. As a result, natural convection and re-radiation from the filter surface contribute more to the overall heat transfer. Under these conditions, the small increase in view factor at the middle section does not cause a clear rise in temperature. In contrast, the top section, which initially receives very little radiation, shows a stronger response to tilt because even a small change in its exposure leads to a noticeable increase in radiative heating.

The comparison between experimental temperature measurements and view factor calculations confirms that during the initial heating period, radiation is the dominant heat transfer mode. The reduction in the temperature rise in the bottom section of the filter and the increase in the middle and top sections as the tilt angle increases are consistent with the redistribution of view factors. This agreement supports the interpretation that geometric orientation directly governs the distribution of radiative energy across the filter.

5.9 Comparison of Experimental Results and the Numerical Study

In this section, the experimental results are compared with the numerical simulations in ANSYS Fluent. Since the exact properties of the filter were unknown, different values of thermal conductivity, and boundary conditions were tested until the simulations matched the experiments most closely. After determining the optimal parameters, three heater tilt angles were simulated.

A schematic of the experimental setup is shown in Figure 5.52. The system consists of a pleated filter and a ceramic heater positioned 10 cm apart, which were used for both the experimental tests and the numerical simulation presented in the following subsections. This arrangement was used to study radiative heat transfer to the filter for the numerical verification.

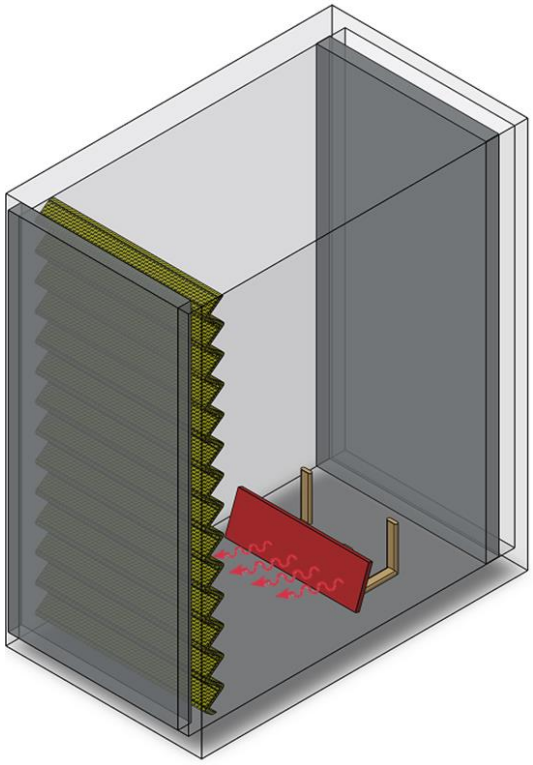

Figure 5.52. Schematic of the experimental setup for comparison with the numerical results. The pleated HVAC filter was mounted vertically inside an insulated enclosure, while a ceramic heater was positioned at an adjustable tilt angle in front of the filter.

5.9.1 Uncertainty Analysis of Filter Properties and Boundary Conditions

Since the exact thermophysical properties of the filter were not available, a series of simulations was carried out by varying the filter's thermal conductivity and boundary conditions.

This uncertainty analysis was conducted to estimate the unknown filter parameters by testing different values of thermal conductivity and varying the boundary conditions. The objective was to identify the parameter values that minimized the discrepancy between numerical predictions and experimental results. In all simulations of this section, the filter emissivity was set to 0.8, consistent with typical literature values for polyester-based filters [97,99].

5.9.1.1 Effect of Boundary Conditions

The first set of simulations examined the influence of boundary conditions, as they define the thermal environment of the system. The boundary condition cases considered are summarized in Table 5.5.

To illustrate the results, Figure 5.57 compares the experimental temperature profile along the filter height with the numerical results for two boundary condition cases. Both Cases 1 and 2 follow the experimental trend similarly.

Interestingly, there is little difference between Cases 1 and 2. This is because the results are shown after only 10 seconds, when the wall temperature rise is still slight, making the temperature difference between the unit walls and the surrounding room negligible. Under these conditions, the convective heat transfer rate is very low, and the boundaries effectively behave as if they were adiabatic. The low convective heat transfer coefficient at room temperature further reduces heat exchange, making the outcomes nearly identical to the zero–heat-flux condition.

Overall, Case 2 provided the best agreement with the experimental data. Therefore, the subsequent simulations were performed using adiabatic side walls and radiative front and back surfaces.

Table 5.5. Boundary condition definitions for the three simulated cases

Case	Right & Left	Top	Bottom	Front & Back
1	Convection	Convection	Zero heat flux	Radiation
2	Zero heat flux	Zero heat flux	Zero heat flux	Radiation

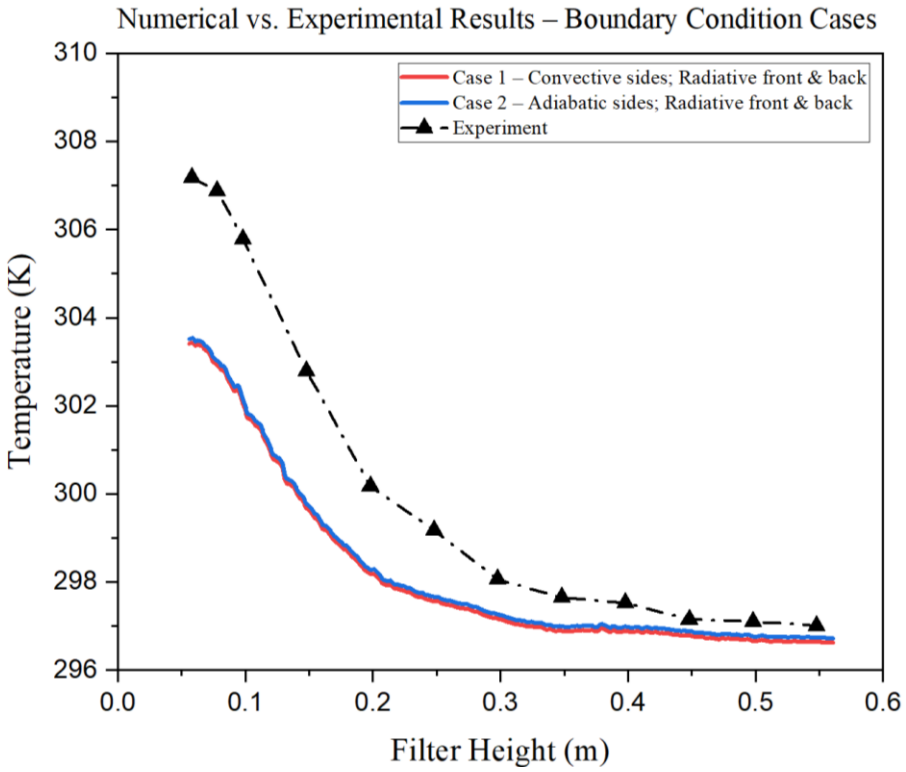

Figure 5.53. Comparison of experimental results with numerical simulations under different boundary condition assumptions at $\alpha = 0°$, $\varepsilon = 0.8$, $k = 0.14\ w/mK$, $T_{setpoint} = 200℃$.

5.9.2 Effect of Thermal Conductivity

After identifying the most suitable boundary conditions, the next step was to examine the effect of the filter's thermal conductivity, as this property was not provided by the manufacturer. Figure 5.58 compares the experimental data with numerical predictions for different assumed values of thermal conductivity: thermal conductivity of the polyester fiber ($k_{Fiber-polyester}$) and bulk thermal conductivity. The bulk thermal conductivity was calculated using the following relation [100]:

$$k_{bulk} = (1 - \varphi)k_{fiber-polyester} + \varphi k_{air} \qquad 5.7$$

At room temperature (22 ℃), the thermal conductivity of polyester fibers and air are $k_{Fiber-\ polyester} = 0.14\ w/mK$ and $k_{air} = 0.025\ w/mK$, respectively [87]. Assuming a typical porosity of $\varphi = 0.9$ for MERV 11 filters, the bulk thermal conductivity was calculated as $k_{bulk} = 0.0365\ w/mK$.

From Figure 5.54 when the thermal conductivity of polyester fiber $\left(k_{Fiber\ polyester} = 0.14\ w/mK\right)$ was directly applied, the model produces temperatures lower than the measurements across the filter height. This assumption treats the filter as a solid polyester medium and neglects the influence of porosity and the presence of air between the fibers.

In contrast, using the bulk thermal conductivity (k_{bulk}) provided much better agreement with the experimental results. This approach accounts for the porous nature of the filter by combining the conductivities of polyester fibers and air, yielding a more realistic representation of heat transfer through the filter. The filter is highly porous and made up mostly of air pockets, and since air conducts heat poorly, the filter behaves more like a low-conductivity medium. In this case, heat does not penetrate deeply but stays near the surface, causing the surface temperature to rise more noticeably. This explains why the lower conductivity assumption agrees better with the experimental results.

Overall, the comparison highlights that the bulk conductivity is more appropriate for modeling porous filters, as it captures both the solid and air phases within the structure. Consequently, k_{bulk} was adopted in the subsequent simulation.

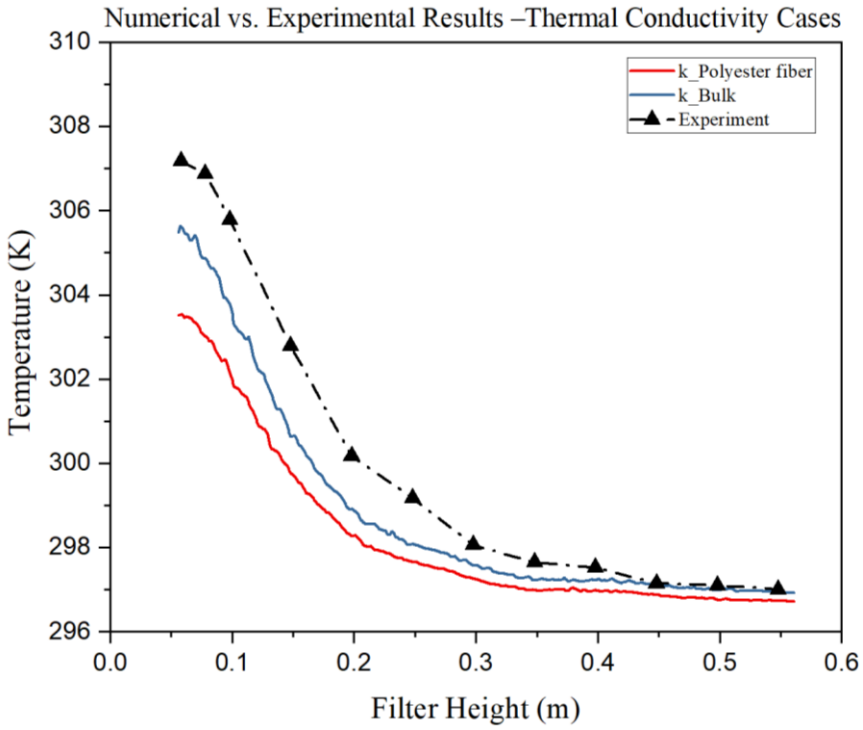

Figure 5.54. Comparison of experimental and numerical temperature distributions along the filter height for two thermal conductivity assumptions with $\varepsilon = 0.8$, $\alpha = 0°$, and $T_{setpoint} = 200℃$.

After identifying the most appropriate boundary condition for the unit walls (zero heat flux) and determining the effective bulk thermal conductivity of the filter medium, the next step was to investigate the effect of heater orientation. After confirming the accuracy of the selected parameters, the verification step examined how changing the heater's orientation with respect to the filter influenced the predicted temperature distribution.

5.9.3 Verification of Heater Orientation Effects

In this stage of the verification, the influence of heater orientation was examined by tilting the ceramic heater at three different angles ($\alpha = 0°$, $\alpha = 10°$, and $\alpha = 20°$) relative to the pleated filter. The experimental setup was arranged in the same manner, allowing direct comparison between measured and simulated results.

Figures 5.55 and 5.56 illustrate the temperature profiles along the filter height for the three tilt angles in the numerical model and experiments, respectively. The results correspond to 10 seconds of heating, with the heater set at 200 ℃ and positioned 10 cm from the filter surface. In both sets of results, the temperature profiles show a similar pattern, with the maximum values occurring at the lower part of the filter, where the radiative effect is most intense, and gradually declining toward the top. Furthermore, since the heater was positioned only 10 cm from the filter surface, the maximum temperature consistently occurred at the bottom regardless of orientation.

In addition, Figure 5.56 shows that when the heater is tilted to 20 °, the temperature at the bottom drops slightly, while the top experiences a slight increase. This limited effect is mainly because the exposure time was short (10 seconds), and the same trend also appears in the numerical results.

Finally, as can be seen from Figures 5.55 and 5.56, there is a consistency between the experimental and numerical profiles, which demonstrates that the simulations can predict the experimental data, capturing the correct transient behaviour and the relative impact of heater tilt under these conditions.

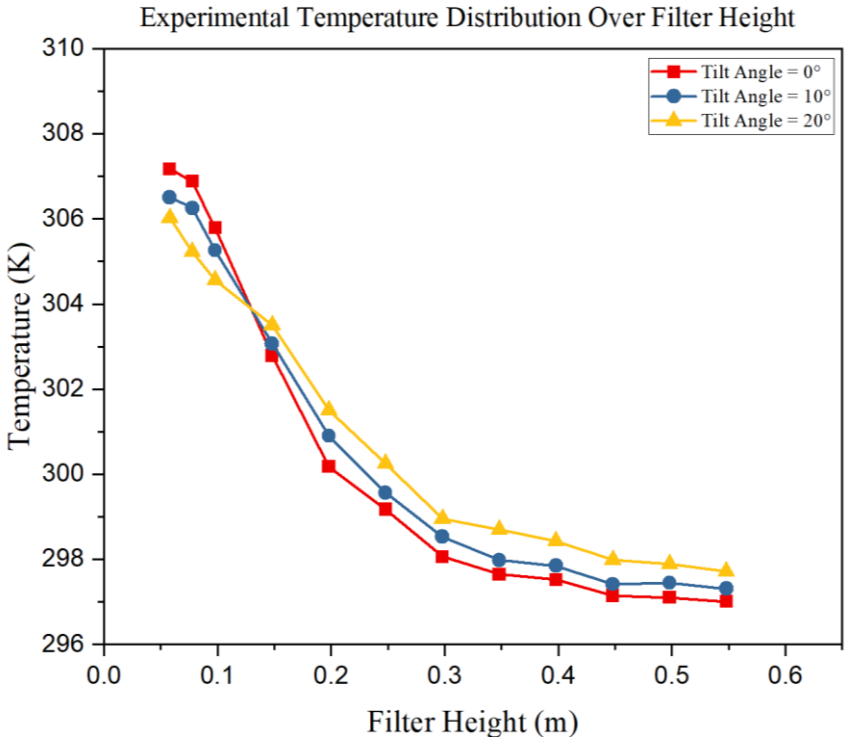

Figure 5.55. Experimental temperature distribution along the filter height for different tilt angle.

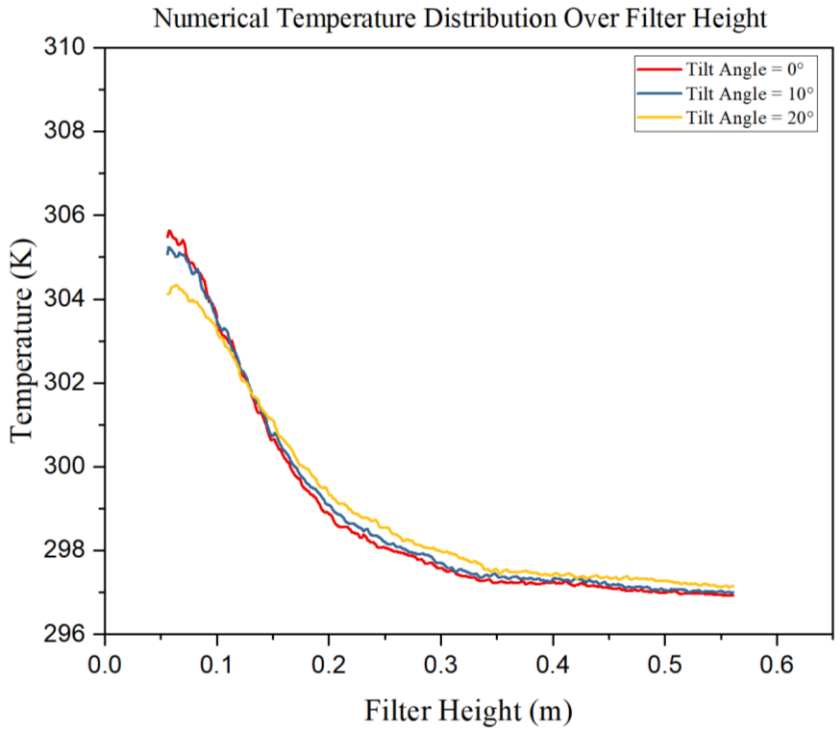

Figure 5.56. Experimental temperature distribution along the filter height for different tilt angle

To clearly demonstrate the comparative behavior between experimental measurements and numerical predictions, Figure 5.57 shows the temperature distributions along the filter height for each tilt angle individually: (a) $\alpha = 0\,°$, (b) $\alpha = 10\,°$, and (c) $\alpha = 20\,°$. In all cases, the profiles show the same general behavior, with maximum temperatures occurring at the bottom of the filter and gradually decreasing with height.

For the $\alpha = 0\,°$ case (Figure 5.57a), the maximum error between numerical and experimental results is 7.26% at a height of 0.148 m, while the error at the top of the filter is less than 1% (0.27%). For the $\alpha = 10\,°$ case (Figure 5.56b), the maximum error increases slightly to 7.73% at 0.148 m, with the error at the top rising to 1.17%. In the $\alpha = 20\,°$ case (Figure 5.57c), the maximum error is 7.75%, and the error at the top further increases to 2.39%. The variations between numerical results and experimental data in the top section of the filter, which occur with changing tilt angle, are mainly due to the neglect of natural convection in the numerical model. Although the exposure time is short and radiation dominates the heat transfer process, natural convection is still present in the experiments, whereas it is entirely absent in the simulations. This difference, though minor, becomes more noticeable as the tilt angle increases, since the upper sections of the filter receive greater radiative exposure and the contribution of convection helps to elevate the temperatures in those regions.

In addition, Figure 5.57 reveals that the discrepancy between numerical and experimental results becomes larger at $\alpha = 20\,°$ than at $\alpha = 0\,°$ or $\alpha = 10\,°$, reflecting the increased difficulty of capturing heat distribution at higher tilt angles. These discrepancies can be explained by the simplifying assumptions in the simulations, which were discussed in section 4.3.

Despite these discrepancies, the consistent alignment of overall trends across the three tilt angles confirms that the numerical model can predict the experimental data within the tested range.

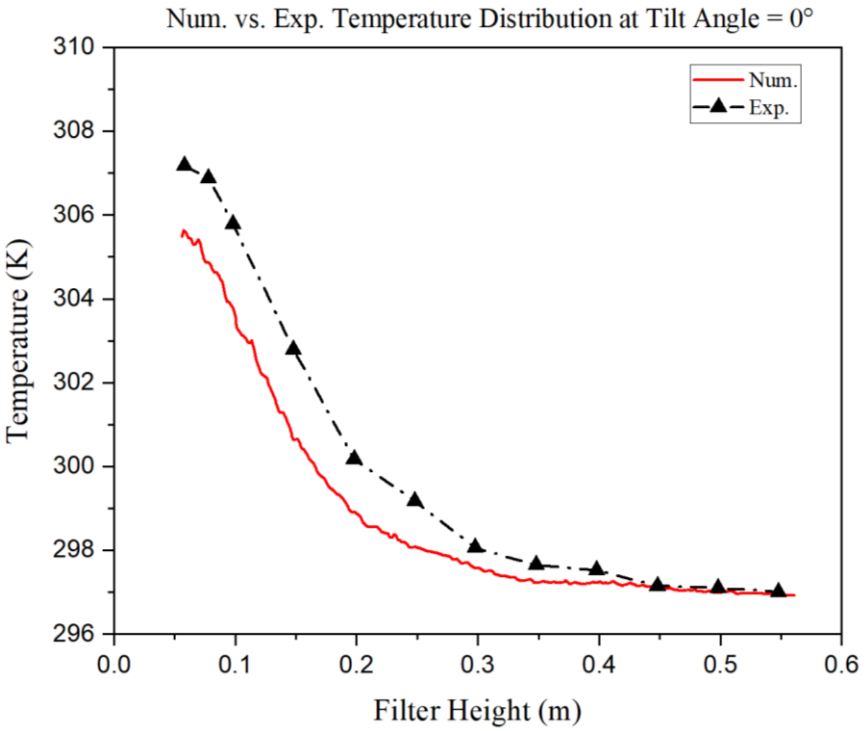
Num. vs. Exp. Temperature Distribution at Tilt Angle = 0°
Num.
Exp.
Temperature (K)
310
308
306
304
302
300
298
296
0.0
0.1
0.2
0.3
0.4
0.5
0.6
Filter Height (m)

(a)

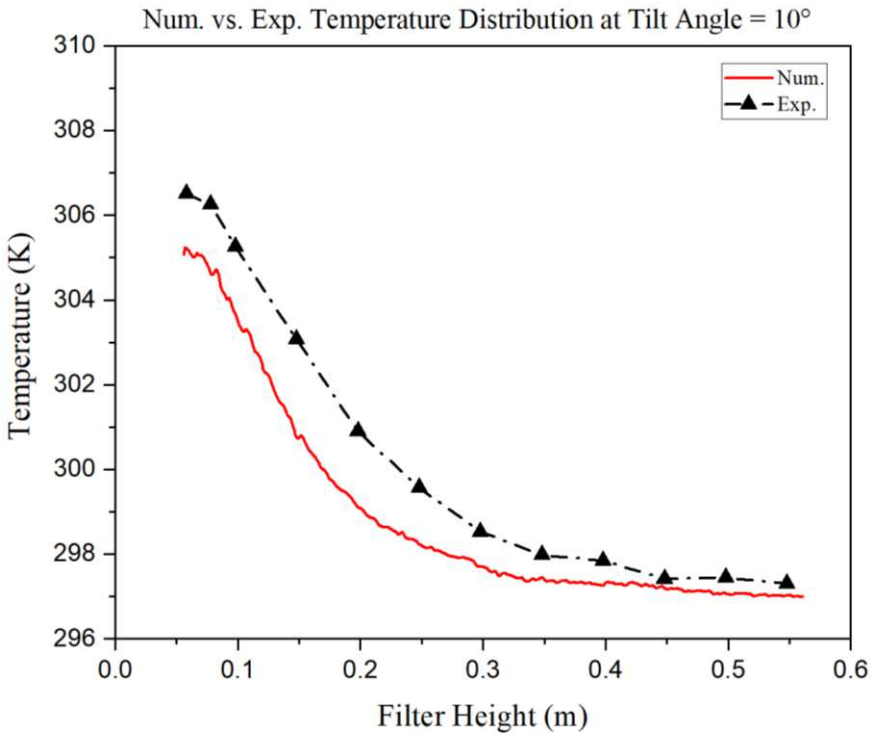
Num. vs. Exp. Temperature Distribution at Tilt Angle = 10°
Num.
Exp.
Temperature (K)
310
308
306
304
302
300
298
296
0.0
0.1
0.2
0.3
0.4
0.5
0.6
Filter Height (m)

(b)

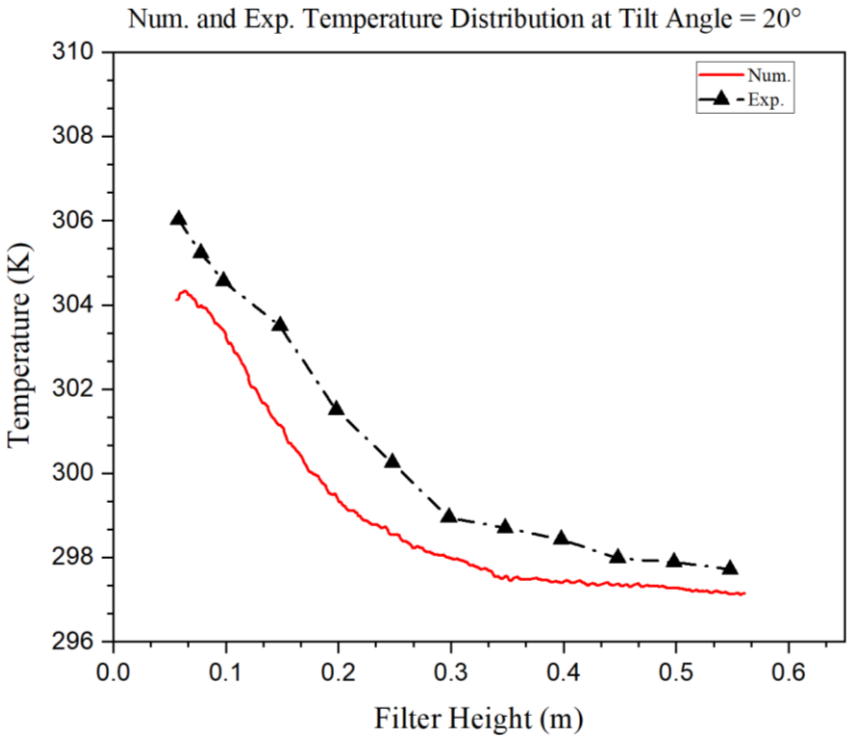

(c)

Figure 5.57. Comparison of experimental and numerical temperature distributions along the filter height at three heater tilt angles: (a) $\alpha = 0$ °, (b) $\alpha = 10$ °, and (c) $\alpha = 20$ °.

Chapter 6. Conclusion and Future Work

6.1 Conclusion

This study developed and evaluated a novel infrared heat-based disinfection approach for pleated HVAC filters, combining ceramic heaters and filter media to achieve surface sterilization without heating the bulk air. A combination of experimental measurements, radiative view factor calculations, and numerical simulations was applied to determine the influence of geometric and operational parameters, including distance between the heater and the filter, tilt angle of the heater, filter coatings, and enclosure reflectivity, on temperature uniformity, energy efficiency, and disinfection capability. The main findings can be summarized as follows:

1. **Feasibility of Heat-Based Disinfection:**

   The proposed system successfully achieved the target disinfection temperature of 65 ℃ across the filter surface within short exposure periods, confirming the viability of IR-assisted disinfection for in-situ HVAC applications when the fan is off. For instance, when two ceramic heaters were placed on both sides of the filter at a distance of 35 cm, with a tilt angle of 0 ° and a setpoint temperature of 220 ℃, complete disinfection was achieved within 17 minutes, corresponding to a total electrical energy consumption of 0.09 kWh and a maximum temperature difference of 8 ℃ across the filter surface.

2. **Influence of Geometry:**

   The heater–filter distance and tilt angle have a significant influence on temperature uniformity.

At shorter distances, heat transfer as well as net radiative heat flux are enhanced because a greater portion of the radiation emitted by the heater is incident on the filter; however, this also raises the risk of localized overheating due to non-uniform radiation distribution. Conversely, at larger distances, the maximum filter temperature decreases as the view factor and the fraction of intercepted radiation are reduced. In addition, the larger distance facilitates stronger buoyancy-driven airflow, which carries heat away from the filter surface and further contributes to temperature reduction.

In addition, the tilt angle (α) alters the directionality of the radiative flux and the local view factor across the filter surface. Small tilt angles, particularly at short heater–filter distances, improve radiation coverage and enhance temperature uniformity by redirecting part of the heat flux toward previously cooler regions of the filter. For instance, at D = 15 cm in the fully aluminum-covered configuration, the maximum filter temperature difference is 10 ℃ after 18 min at $0\,°$ tilt, whereas it drops to 6 ℃ after 22 min when the heater is tilted by $20\,°$.

3. **Surface and Enclosure Modifications:**

Surface and enclosure modifications also played an important role in thermal performance. The use of aluminum reflectors behind the ceramic improved radiation distribution. Reflators are used for focusing the radiation energy in the direction of the material to be heated. For instance, at D =25 cm, $\alpha = 20\,°$, and a setpoint temperature of 250 ℃, the filter reaches 65 ℃ in 15 minutes when the ceramic heater is equipped with a reflector. When the reflector is removed, the filter reaches 65 ℃ after 20 minutes. After 25 minutes, the temperature difference across the filter decreases from approximately 9.2 ℃ without the reflector to about 7.5 ℃ with the reflector.

Moreover, the application of a carbon coating on the filter surface increased its absorptivity and accelerated heating compared to the uncoated polyester filter. Two positive influences of the carbon-coated filter are the reduction in electrical energy consumption and the improvement in the temperature distribution uniformity across the filter surface.

4. Energy Performance:

The proposed infrared-based disinfection system is energy efficient, as it achieves effective microbial inactivation with minimal power consumption compared with conventional thermal treatment methods. The average electrical energy required for each disinfection cycle ranged between 0.04 kWh when one ceramic heater is used and 0.12 kWh when two ceramic heaters are used.

For the optimal configuration with transparent gates, the maximum electrical consumption was 0.09 kWh when two ceramic heaters were placed on each side of the filter at a distance of 35 cm, a tilt angle of 0 °, and a setpoint temperature of 220 ℃.

5. Comparison of Experimental Results and View Factor Calculations

The comparison between the calculated view factor between the ceramic heater and the filter and the measured temperature distribution over the filter surface revealed a clear qualitative relationship between them. As the heater–filter distance increases, the view factor decreases, which reduce the total radiative energy incident on the filter and consequently the maximum filter temperature also decreases. In addition, as the tilt angle increases, the view factor in the lower section of the filter decreases, while the middle and upper regions experience higher values. This pattern is also reflected in the temperature

distribution, particularly at shorter distances where radiative heat transfer dominates over natural convection.

6. **Comparison of Experimental and Numerical Results**

   The numerical simulations which were performed with certain simplifications and considering only the radiative heat transfer during the initial heating period, showed good agreement with the experimental results and can serve as a reliable basis for future design optimization and system scalability. The predicted temperature distribution over the filter matched the measured data with errors below 8% in most cases.

Overall, the research confirms that using infrared ceramic heaters can uniformly disinfect pleated HVAC filters without damaging the media and significantly decreasing the energy consumption. The results establish the fundamental design criteria for implementing in-duct or standalone self-disinfecting filtration units.

Additionally, the system is scalable to fit a variety of HVAC system dimensions. By utilizing view factor analysis and validated numerical simulations, the design can be adjusted to different filter sizes and geometric configurations. In other words, the integration of an infrared ceramic heater and filter can be customized for various HVAC systems, making the solution broadly applicable and practical for real-world deployment.

6.2 Current Research Limitations and Future Recommendations

The present research has certain limitations that should be addressed in future studies. First, the numerical simulations primarily accounted for radiative heat transfer, neglecting the influence of natural convection. Second, the investigation focused mainly on short-term heating to isolate the effects of radiation, without examining the long-term thermal stability of the system or its

performance under repeated disinfection cycles. Finally, the view factor and CFD analyses were based on simplified geometrical assumptions and idealized surface emissivity values, which did not account for the practical irregularities present in pleated filter structures or variations arising from manufacturing tolerances.

Moreover, the experiments were carried out under controlled laboratory conditions with still air and no fan operation, which does not fully represent the dynamic nature of real HVAC systems. In practical applications, airflow patterns, humidity levels, and particle concentrations fluctuate continuously and can significantly affect thermal performance and disinfection efficiency. In addition, the study was limited to testing polyester and carbon-coated filters in combination with ceramic infrared heaters; therefore, the impact of alternative filter media and other heater types was unexplored.

Another limitation of the present study is that the effect of dust accumulation on both the filter surface and the ceramic heater was not considered. Although many HVAC systems include a pre-filter to capture larger particles, dust accumulation on the ceramic heater surface and filter remains a potential concern. This accumulation can alter the optical and thermal properties of the materials and affect the temperature distribution and energy efficiency.

On the filter side, dust loading can act as an insulating layer, which reduces local heat transfer and creates nonuniform temperature regions. It may also modify the emissivity and absorptivity of the surface; therefore, the overall heating effectiveness may be diminished. On the heater side, the deposited layer of particles introduces a fouling effect. The fouling layer increases thermal resistance and energy dissipation, leading to some of the input heat being absorbed by the dust rather than transmitted to the filter media. This reduces the net energy available for disinfection and can eventually alter the temperature distribution across the filter surface.

Recognizing these requirements, future research recommendations are listed below:

I. **Microbial validation:**

Perform controlled biological experiments using bacterial or viral surrogates to directly confirm pathogen inactivation at measured surface temperatures.

II. **Dynamic (fan-on) testing:**

Extend the experiments to include forced-airflow conditions representative of actual HVAC ducts to assess the combined influence of forced convection and radiation on heat transfer and pathogen inactivation rate.

III. **Techno-economic and life-cycle assessment:**

Conduct a comprehensive analysis of energy savings, operational cost, and potential carbon footprint reduction compared with conventional filter replacement or UV-based systems.

IV. **Scaling and commercialization:**

Explore scaling strategies for larger duct sections and evaluate manufacturability, safety compliance, and retrofit potential in existing HVAC installations.

V. **Influence of Filter Geometry and Pleat Structure**:

Investigate how filter geometry, pleat orientation, and media thickness affect thermal distribution, air circulation, and disinfection uniformity under different heating configurations.

VI. **Coupled CFD–radiation–convection modeling:**

Improve numerical models to include natural and forced convection coupling with spectral radiation for more accurate prediction of transient heating and flow fields.

VII. Effect of Dust Accumulation on Thermal Performance

To ensure sustained performance, future studies should investigate the combined impact of dust loading and heater fouling on the long-term stability, energy consumption, and temperature uniformity of the system. Regular maintenance and cleaning of the heater surface are also recommended to preserve consistent heating efficiency and minimize unwanted energy losses during prolonged use.

One of the strategic future research objectives is the practical implementation of the proposed system beyond bench-scale testing toward integration into full-scale HVAC systems, including actual ductwork and air handling units. To achieve this transition, a comprehensive understanding of how to adapt the geometry and configuration of the heater and filter is required to ensure optimal fit and performance within real-world HVAC environments.

In order to achieve full-scale implementation, it is necessary to identify the relationships among key parameters that affect the temperature distribution across the filter. These parameters can be listed as the Rayleigh number, view factors between surfaces, surface emissivity and absorptivity, the ceramic heater temperature setpoint, and the physical dimensions of the components. Therefore, CFD simulation that account for both natural convection and radiation, as well as controlled experiments at different scales, should be implemented.

Furthermore, by conducting a range of CFD simulations and experimental tests at various scales, we can establish correlations between effective parameters to provide a basis for setting the heater temperature to achieve effective disinfection under diverse HVAC system conditions. Therefore, this gives us a practical guideline for scaling up the technology from a controlled lab setup to real-world HVAC installations.

References

[1] WHO Coronavirus (COVID-19) Dashboard, (2023). https://covid19.who.int/data.

[2] Y. Shang, H. Li, R. Zhang, Effects of pandemic outbreak on economies: evidence from business history context, Frontiers in Public Health 9 (2021) 146. https://doi.org/https://doi.org/10.3389/fpubh.2021.632043.

[3] G. Verikios, The dynamic effects of infectious disease outbreaks: The case of pandemic influenza and human coronavirus, Socio-Economic Planning Sciences 71 (2020) 100898.

[4] T.T. Nguyen, G.R. Johnson, S.C. Bell, L.D. Knibbs, A systematic literature review of indoor air disinfection techniques for airborne bacterial respiratory pathogens, International Journal of Environmental Research and Public Health 19 (2022) 1197.

[5] K. Tran, K. Cimon, M. Severn, C.L. Pessoa-Silva, J. Conly, Aerosol-generating procedures and risk of transmission of acute respiratory infections: a systematic review, CADTH Technology Overviews 3 (2013).

[6] R.M. Jones, L.M. Brosseau, Aerosol transmission of infectious disease, Journal of Occupational and Environmental Medicine 57 (2015) 501–508.

[7] A. Fernstrom, M. Goldblatt, Aerobiology and its role in the transmission of infectious diseases, Journal of Pathogens 2013 (2013) 493960.

[8] E.A. Nardell, Indoor environmental control of tuberculosis and other airborne infections, Indoor Air 26 (2016) 79–87.

[9] A.J. Cohen, M. Brauer, R. Burnett, H.R. Anderson, J. Frostad, K. Estep, K. Balakrishnan, B. Brunekreef, L. Dandona, R. Dandona, Estimates and 25-year trends of the global burden

of disease attributable to ambient air pollution: an analysis of data from the Global Burden of Diseases Study 2015, The Lancet 389 (2017) 1907–1918. https://doi.org/https://doi.org/10.1016/S0140-6736(17)30505-6.

[10] G. Liu, M. Xiao, X. Zhang, C. Gal, X. Chen, L. Liu, S. Pan, J. Wu, L. Tang, D. Clements-Croome, A review of air filtration technologies for sustainable and healthy building ventilation, Sustainable Cities and Society 32 (2017) 375–396. https://doi.org/10.1016/j.scs.2017.04.011.

[11] J.C. Luongo, J. Brownstein, S.L. Miller, Ultraviolet germicidal coil cleaning: Impact on heat transfer effectiveness and static pressure drop, Building and Environment 112 (2017) 159–165.

[12] D. Menzies, J. Popa, J.A. Hanley, T. Rand, D.K. Milton, Effect of ultraviolet germicidal lights installed in office ventilation systems on workers' health and wellbeing: double-blind multiple crossover trial, The Lancet 362 (2003) 1785–1791.

[13] A. Handbook, HVAC systems and equipment, (1996).

[14] C.A. Balaras, E. Dascalaki, A. Gaglia, HVAC and indoor thermal conditions in hospital operating rooms, Energy and Buildings 39 (2007) 454–470. https://doi.org/10.1016/j.enbuild.2006.09.004.

[15] L. Song, J. Zhou, C. Wang, G. Meng, Y. Li, M. Jarin, Z. Wu, X. Xie, Airborne pathogenic microorganisms and air cleaning technology development: A review, Journal of Hazardous Materials 424 (2022) 127429. https://doi.org/https://doi.org/10.1016/j.jhazmat.2021.127429.

[16] (n.d.). Camfil, COMBATING THE VIRUS IN THE AIR & CORONAVIRUS AIR FILTRATION STRATEGIES, (n.d.). https://www.camfil.com/en-us/insights/life-science-and-healthcare/virus (accessed March 2, 2023).

[17] W. Zheng, J. Hu, Z. Wang, J. Li, Z. Fu, H. Li, J. Jurasz, S.K. Chou, J. Yan, COVID-19 impact on operation and energy consumption of heating, ventilation and air-conditioning (HVAC) systems, Advances in Applied Energy 3 (2021) 100040.

[18] Z. Liu, S. Ma, G. Cao, C. Meng, B.-J. He, Distribution characteristics, growth, reproduction and transmission modes and control strategies for microbial contamination in HVAC systems: A literature review, Energy and Buildings 177 (2018) 77–95. https://doi.org/https://doi.org/10.1016/j.enbuild.2018.07.050.

[19] M. Baselga, J.J. Alba, A.J. Schuhmacher, Impact of needle-point bipolar ionization system in the reduction of bioaerosols in collective transport, Science of the Total Environment 855 (2023) 158965.

[20] J. Liu, Z.J. Yu, Z. Liu, D. Qin, J. Zhou, G. Zhang, Performance analysis of earth-air heat exchangers in hot summer and cold winter areas, Procedia Engineering 205 (2017) 1672–1677.

[21] X. Li, D. Liu, J. Yao, Aerosolization of fungal spores in indoor environments, Science of The Total Environment 820 (2022) 153003.

[22] K. Morisseau, A. Joubert, L. Le Coq, Y. Andres, Quantification of the fungal fraction released from various preloaded fibrous filters during a simulated ventilation restart, Indoor Air 27 (2017) 529–538. https://doi.org/10.1111/ina.12330.

[23] Z. Feng, Z. Long, Q. Chen, Assessment of various CFD models for predicting airflow and pressure drop through pleated filter system, Building and Environment 75 (2014) 132–141.

[24] S. Li, S. Hu, B. Xie, H. Jin, J. Xin, F. Wang, F. Zhou, Influence of pleat geometry on the filtration and cleaning characteristics of filter media, Separation and Purification Technology 210 (2019) 38–47.

[25] American Society of Heating, Refrigerating, and Air-Conditioning Engineers (ASHRAE), technical resources, HVAC System Maintenance and Filter Replacement during the COVID-19 Pandemic, (2020).

[26] D. Das, A. Waychal, On the triboelectrically charged nonwoven electrets for air filtration, Journal of Electrostatics 83 (2016) 73–77.

[27] S.-H. Huang, C.-W. Chen, Y.-M. Kuo, C.-Y. Lai, R. McKay, C.-C. Chen, Factors affecting filter penetration and quality factor of particulate respirators, Aerosol and Air Quality Research 13 (2013) 162–171.

[28] R. Zendehdel, M.M. Amini, M. Hajibabaei, M.J. Nasiri, M.J. Jafari, M.K. Alavijeh, Doping metal–organic framework composites to antibacterial air filter development for quality control of indoor air, Environmental Progress & Sustainable Energy 41 (2022) e13909.

[29] G. Berry, A. Parsons, M. Morgan, J. Rickert, H. Cho, A review of methods to reduce the probability of the airborne spread of COVID-19 in ventilation systems and enclosed spaces, Environmental Research 203 (2022) 111765. https://doi.org/https://doi.org/10.1016/j.envres.2021.111765.

[30] Y. Ju, T. Han, J. Yin, Q. Li, Z. Chen, Z. Wei, Y. Zhang, L. Dong, Bumpy structured

nanofibrous membrane as a highly efficient air filter with antibacterial and antiviral property, Science of the Total Environment 777 (2021) 145768.

[31] C. Balagna, R. Francese, S. Perero, D. Lembo, M. Ferraris, Nanostructured composite coating endowed with antiviral activity against human respiratory viruses deposited on fibre-based air filters, Surface and Coatings Technology 409 (2021) 126873.

[32] A.H. Mamaghani, F. Haghighat, C.-S. Lee, Photocatalytic oxidation technology for indoor environment air purification: The state-of-the-art, Applied Catalysis B: Environmental 203 (2017) 247–269.

[33] J. Mo, Y. Zhang, Q. Xu, Y. Zhu, J.J. Lamson, R. Zhao, Determination and risk assessment of by-products resulting from photocatalytic oxidation of toluene, Applied Catalysis B: Environmental 89 (2009) 570–576.

[34] S.O. Hay, T. Obee, Z. Luo, T. Jiang, Y. Meng, J. He, S.C. Murphy, S. Suib, The viability of photocatalysis for air purification, Molecules 20 (2015) 1319–1356.

[35] A. Bisag, P. Isabelli, R. Laurita, C. Bucci, F. Capelli, G. Dirani, M. Gherardi, G. Laghi, A. Paglianti, V. Sambri, Cold atmospheric plasma inactivation of aerosolized microdroplets containing bacteria and purified SARS-CoV-2 RNA to contrast airborne indoor transmission, Plasma Processes and Polymers 17 (2020) 2000154.

[36] D. Dobrynin, G. Fridman, Y. V Mukhin, M.A. Wynosky-Dolfi, J. Rieger, R.F. Rest, A.F. Gutsol, A. Fridman, Cold plasma inactivation of Bacillus cereus and Bacillus anthracis (anthrax) spores, IEEE Transactions on Plasma Science 38 (2010) 1878–1884.

[37] L.M. Vasilyak, Physical methods of disinfection (a review), Plasma Physics Reports 47

(2021) 318–327.

[38] F. Masotti, L. Vallone, S. Ranzini, T. Silvetti, S. Morandi, M. Brasca, Effectiveness of air disinfection by ozonation or hydrogen peroxide aerosolization in dairy environments, Food Control 97 (2019) 32–38.

[39] A.J. Brodowska, A. Nowak, K. Śmigielski, Ozone in the food industry: Principles of ozone treatment, mechanisms of action, and applications: An overview, Critical Reviews in Food Science and Nutrition 58 (2018) 2176–2201.

[40] X. Kang, W. Gao, B. Wang, B. Yu, L. Guo, B. Cui, A.M. Abd El-Aty, Effect of moist and dry-heat treatment processes on the structure, physicochemical properties, and in vitro digestibility of wheat starch-lauric acid complexes, Food Chemistry 351 (2021) 129303. https://doi.org/https://doi.org/10.1016/j.foodchem.2021.129303.

[41] J.H. Jung, J.E. Lee, C.H. Lee, S.S. Kim, B.U. Lee, Treatment of fungal bioaerosols by a high-temperature, short-time process in a continuous-flow system, Applied and Environmental Microbiology 75 (2009) 2742–2749.

[42] B. Bharti, H. Li, Z. Ren, R. Zhu, Z. Zhu, Recent advances in sterilization and disinfection technology: A review, Chemosphere 308 (2022) 136404.

[43] H. Luo, L. Zhong, Ultraviolet germicidal irradiation (UVGI) for in-duct airborne bioaerosol disinfection: Review and analysis of design factors, Building and Environment 197 (2021) 107852.

[44] E.F. Dunn, A. Akhtar, A. Dunn, S. Lacey, E. Pauley, C. Powers, J. McKee, D. Petereit, Evaluating an ultraviolet C system for use during SARS-CoV2 pandemic and personal

protective equipment shortage, Advances in Radiation Oncology 6 (2021) 100636.

[45] American Society of Heating, Refrigerating, and Air-Conditioning Engineers (ASHRAE), Handbook, Chapter 62: Ultraviolet Air and Surface Treatment, (2019).

[46] M. Raeiszadeh, B. Adeli, A critical review on ultraviolet disinfection systems against COVID-19 outbreak: applicability, validation, and safety considerations, Acs Photonics 7 (2020) 2941–2951.

[47] C. Wang, L. Song, Z. Zhang, Y. Wang, X. Xie, Microwave-induced release and degradation of airborne antibiotic resistance genes (ARGs) from Escherichia coli bioaerosol based on microwave absorbing material, Journal of Hazardous Materials 394 (2020) 122535.

[48] G. Kampf, A. Voss, S. Scheithauer, Inactivation of coronaviruses by heat, Journal of Hospital Infection 105 (2020) 348–349.

[49] K.R. Wigginton, B.M. Pecson, T. Sigstam, F. Bosshard, T. Kohn, Virus inactivation mechanisms: impact of disinfectants on virus function and structural integrity, Environmental Science & Technology 46 (2012) 12069–12078.

[50] R.J. Fischer, D.H. Morris, N. van Doremalen, S. Sarchette, M.J. Matson, T. Bushmaker, C.K. Yinda, S.N. Seifert, A. Gamble, B.N. Williamson, Effectiveness of N95 respirator decontamination and reuse against SARS-CoV-2 virus, Emerging Infectious Diseases 26 (2020) 2253.

[51] G. Cebrián, S. Condón, P. Mañas, Physiology of the inactivation of vegetative bacteria by thermal treatments: Mode of action, influence of environmental factors and inactivation kinetics, Foods 6 (2017) 107.

[52] J. Bartram, Legionella and the prevention of legionellosis, World Health Organization, 2007.

[53] C. Doig, A.L. Seagar, B. Watt, K.J. Forbes, The efficacy of the heat killing of Mycobacterium tuberculosis, Journal of Clinical Pathology 55 (2002) 778–779.

[54] A.S.N.W. Pahalagedara, E. Gkogka, M. Hammershøj, A review on spore-forming bacteria and moulds implicated in the quality and safety of thermally processed acid foods: Focusing on their heat resistance, Food Control 166 (2024) 110716.

[55] Y.-H. Wang, X.-L. Wang, J. Song, Q.-Q. Song, X.-N. Luo, D. Xia, J. Han, Journal of Antivirals & Antiretrovirals, (2017).

[56] M.S. Vlaskin, Review of air disinfection approaches and proposal for thermal inactivation of airborne viruses as a life-style and an instrument to fight pandemics, Applied Thermal Engineering 202 (2022) 117855.

[57] M. Shaffer, K. Huynh, V. Costantini, J. Vinjé, K. Bibby, Heat inactivation of aqueous viable norovirus and MS2 bacteriophage, Journal of Applied Microbiology 135 (2024) lxae033.

[58] S. Zou, J. Guo, R. Gao, L. Dong, J. Zhou, Y. Zhang, J. Dong, H. Bo, K. Qin, Y. Shu, Inactivation of the novel avian influenza A (H7N9) virus under physical conditions or chemical agents treatment, Virology Journal 10 (2013) 289.

[59] Z. Wu, H. Zheng, J. Gu, F. Li, R. Lv, Y. Deng, W. Xu, Y. Tong, Effects of different temperature and time durations of virus inactivation on results of real-time fluorescence PCR testing of COVID-19 viruses, Current Medical Science 40 (2020) 614–617.

[60] J.H. Jung, J.E. Lee, S.S. Kim, Thermal effects on bacterial bioaerosols in continuous air

flow, Science of the Total Environment 407 (2009) 4723–4730.

[61] M.S. Vlaskin, Review of air disinfection approaches and proposal for thermal inactivation of airborne viruses as a life-style and an instrument to fight pandemics, Applied Thermal Engineering 202 (2022) 117855. https://doi.org/10.1016/j.applthermaleng.2021.117855.

[62] S.A. Grinshpun, A. Adhikari, C. Li, M. Yermakov, L. Reponen, E. Johansson, M. Trunov, Inactivation of aerosolized viruses in continuous air flow with axial heating, Aerosol Science and Technology 44 (2010) 1042–1048. https://doi.org/10.1080/02786826.2010.509119.

[63] M.S. Vlaskin, Review of air disinfection approaches and proposal for thermal inactivation of airborne viruses as a life-style and an instrument to fight pandemics, Applied Thermal Engineering 202 (2022) 117855. https://doi.org/10.1016/j.applthermaleng.2021.117855.

[64] A.A. Sagade, R. Palma-Behnke, Experimental feasibility study of multipurpose low-cost solar thermal device for different applications including inactivation of SARS CoV-2, Sustainable Energy Technologies and Assessments 56 (2023) 103034. https://doi.org/10.1016/j.seta.2023.103034.

[65] N. Soni, D. Sharma, V. Nimesh, V. Mahendra Reddy, Solar energy assisted thermal treatment model to decontaminate airborne viruses in hospital, Thermal Science and Engineering Progress 36 (2022) 101516. https://doi.org/10.1016/j.tsep.2022.101516.

[66] H. Xie, B. Yu, J. Wang, J. Ji, A novel disinfected Trombe wall for space heating and virus inactivation: Concept and performance investigation, Applied Energy (2021).

[67] H. Xie, H. Jia, J. Ji, Y. Qian, H. Meng, J. Li, Y. Mu, Performance analysis of a novel air

filtration and sterilization PV-Trombe wall, Building and Environment 265 (2024) 111953.

[68] L. Yu, G.K. Peel, F.H. Cheema, W.S. Lawrence, N. Bukreyeva, C.W. Jinks, J.E. Peel, J.W. Peterson, S. Paessler, M. Hourani, Z. Ren, Catching and killing of airborne SARS-CoV-2 to control spread of COVID-19 by a heated air disinfection system, Materials Today Physics 15 (2020). https://doi.org/10.1016/j.mtphys.2020.100249.

[69] L.F. Ludwig-Begall, C. Wielick, L. Dams, H. Nauwynck, P.F. Demeuldre, A. Napp, J. Laperre, E. Haubruge, E. Thiry, The use of germicidal ultraviolet light, vaporized hydrogen peroxide and dry heat to decontaminate face masks and filtering respirators contaminated with a SARS-CoV-2 surrogate virus, Journal of Hospital Infection 106 (2020) 577–584. https://doi.org/10.1016/j.jhin.2020.08.025.

[70] Z.D. Bolashikov, A.K. Melikov, Methods for air cleaning and protection of building occupants from airborne pathogens, Building and Environment 44 (2009) 1378–1385.

[71] W. Kowalski, Ultraviolet germicidal irradiation handbook: UVGI for air and surface disinfection, Springer science & business media, 2010.

[72] G. Ko, M.W. First, H.A. Burge, The characterization of upper-room ultraviolet germicidal irradiation in inactivating airborne microorganisms., Environmental Health Perspectives 110 (2002) 95–101.

[73] Z. Feng, F. Wei, H. Li, C.W. Yu, Evaluation of indoor disinfection technologies for airborne disease control in hospital, Indoor and Built Environment 30 (2021) 727–731. https://doi.org/10.1177/1420326X211002948.

[74] N. Mahanta, V. Saxena, L.M. Pandey, P. Batra, U.S. Dixit, Performance study of a

sterilization box using a combination of heat and ultraviolet light irradiation for the prevention of COVID-19, Environmental Research 198 (2021) 111309.

[75] N. Mahanta, S. Sharma, L.G. Sharma, L.M. Pandey, U.S. Dixit, Unfolding of the SARS-CoV-2 spike protein through infrared and ultraviolet-C radiation based disinfection, International Journal of Biological Macromolecules 221 (2022) 71–82. https://doi.org/10.1016/j.ijbiomac.2022.08.197.

[76] S. Lim, E.R. Blatchley, UV disinfection system for cabin air, Advances in Space Research 44 (2009) 942–948. https://doi.org/10.1016/j.asr.2009.06.001.

[77] E.A. Nardell, S.J. Bucher, P.W. Brickner, C. Wang, R.L. Vincent, K. Becan-McBride, M.A. James, M. Michael, J.D. Wright, Safety of upper-room ultraviolet germicidal air disinfection for room occupants: results from the Tuberculosis Ultraviolet Shelter Study, Public Health Reports 123 (2008) 52–60.

[78] B. Karaböce, E. Saban, A. Aydın Böyük, H. Okan Durmuş, R. Hamid, A. Baş, Inactivation of viruses on surfaces by infrared techniques, International Journal of Thermal Sciences 179 (2022). https://doi.org/10.1016/j.ijthermalsci.2022.107595.

[79] I. STARETU, I.O.N. VOICU, New method of sterilization and disinfection of objects infected with COVID 19 and prototype test, Technical Sciences 7 (2022) 279–292.

[80] V.H. Mata-Portuguez, L. Sánchez Pérez, E. Acosta-Gío, Sterilization of heat-resistant instruments with infrared radiation, Infection Control and Hospital Epidemiology 23 (2002) 393–396. https://doi.org/10.1017/S0195941700083028.

[81] Information on: https://www.magnetcenter.ro/panou-radiant-infrarosu-700- w-pentru-

medii- umede-sau-exploziv-ecosun-700-in2-fenix., (n.d.).

[82] B. Damit, C. Lee, C.Y. Wu, Flash infrared radiation disinfection of fibrous filters contaminated with bioaerosols, Journal of Applied Microbiology 110 (2011) 1074–1084. https://doi.org/10.1111/j.1365-2672.2011.04965.x.

[83] R.A. Friedel, L.J.E. Hofer, Spectral characterization of activated carbon, The Journal of Physical Chemistry 74 (1970) 2921–2922.

[84] A. Mirzazade, M. Salimi, E. Rasouli, M. Shahbakhti, A. Nouri, A heat-driven disinfection technology for enhancing indoor air quality in HVAC systems, Journal of Building Engineering 115 (2025) 114513. https://doi.org/10.1016/j.jobe.2025.114513.

[85] Volton, Infrared Ceramics, (2025). https://www.volton.com/en/category/infrared-ceramics-and-panels/232-infrared-ceramics.html.

[86] S. Bell, Good Practice Guide A Beginner ' s Guide to Uncertainty of, Measurement 20 (1999) 586–587. http://opensigle.inist.fr/handle/10068/697460.

[87] F.P. Incropera, D.P. DeWitt, T.L. Bergman, A.S. Lavine, Fundamentals of Heat and Mass Transfer, 6th ed., John Wiley & Sons, Hoboken, 2007.

[88] U. Gross, K. Spindler, E. Hahne, Shapefactor-equations for radiation heat transfer between plane rectangular surfaces of arbitrary position and size with parallel boundaries, Letters in Heat and Mass Transfer 8 (1981) 219–227. https://doi.org/10.1016/0094-4548(81)90016-3.

[89] A. Dehbi, S. Kelm, J. Kalilainen, H. Mueller, The influence of thermal radiation on the free convection inside enclosures, Nuclear Engineering and Design 341 (2019) 176–185. https://doi.org/10.1016/j.nucengdes.2018.10.025.

[90] N.H. Faisal, V. Rajendran, S. Kaniapan, V. Ramalingam, A. Prathuru, R. Ahmed, N.K. Katiyar, A. Bansal, T. Whittaker, P. Isherwood, Air plasma sprayed multi-material composite coatings for enhanced light absorption and thermal emission, Surface and Coatings Technology 498 (2025) 131854.

[91] R. Siegel, J.R. Howell, M.P. Mengüç, Thermal radiation heat transfer, Sixth edit, Boca Raton : CRC Press, Taylor & Francis Group, 2016.

[92] M.F. Modest, S. Mazumder, Radiative Heat Transfer, Fourth edi, London, United Kingdom : Academic Press, 2021.

[93] ANSYS Inc., ANSYS Fluent Theory Guide, Canonsburg, PA, USA, 2024. https://ansyshelp.ansys.com/public/account/secured?returnurl=/Views/Secured/corp/v242/en/flu_th/flu_th.html.

[94] H. Wu, J. Fan, N. Du, Thermal energy transport within porous polymer materials: effects of fiber characteristics, Journal of Applied Polymer Science 106 (2007) 576–583.

[95] S. V. Muley, N.M. Ravindra, Emissivity of electronic materials, coatings, and structures, Jom 66 (2014) 616–636. https://doi.org/10.1007/s11837-014-0940-0.

[96] S.W. Churchill, H.H.S. Chu, Correlating equations for laminar and turbulent free convection from a vertical plate, International Journal of Heat and Mass Transfer 18 (1975) 1323–1329.

[97] R.G. Belliveau, S.A. DeJong, N.D. Boltin, Z. Lu, B.M. Cassidy, S.L. Morgan, M.L. Myrick, Mid-infrared emissivity of nylon, cotton, acrylic, and polyester fabrics as a function of moisture content, Textile Research Journal 90 (2020) 1431–1445.

https://doi.org/10.1177/0040517519888825.

[98] Elstein-Werk M Steinmetz GmbH & Co. KG, Ceramic Infrared Emitters, (n.d.). www.elstein.com.

[99] Optotherm, Emissivity basics, Optotherm (n.d.). https://www.optotherm.com/slides/emissivity-basics-2 (accessed September 16, 2025).

[100] K. Vafai, Handbook of porous media, Crc Press, 2015.

Appendix A- Matlab Code for View Factor Analysis

```
function F12_matrix = view_factor_x_axis_rotation_with_yOffset()
    clear all;
    clc;

    %------------------------------
    % Geometry definitions
    %------------------------------
    % Surface 1 dimensions (in-plane coordinates)
    x1 = 24.5;    % dimension in the local x direction
    y1 = 6;       % dimension in the local y direction
    A1 = x1 * y1; % area of surface 1

    % Surface 2 dimensions
    x2 = 30;      % dimension in x
    y2 = 60;      % dimension in y
    A2 = x2 * y2; % area of surface 2

    % Rotation about the x-axis
    alpha_deg = -20;        % tilt angle %put in negative
    alpha_rad = deg2rad(alpha_deg);

    % Displacement of Surface 1 along global y
    yOffset = -25;  % example offset (positive => shift up)

    % Distance between surfaces along +z
    d = 10;  % surface 2 is at z=d

    %------------------------------
    % Integration resolution
    %------------------------------
    Nx = 50;    % # subdivisions along x
    Ny = 50;    % # subdivisions along y

    %------------------------------
    % SURFACE 1 (rotated about x, then offset in y)
    % Initially, Surface 1 is in xy-plane (z=0), normal +z
    % We'll rotate about x by alpha, then shift up by yOffset.
    %------------------------------
    [X1_local, Y1_local] = meshgrid(linspace(-x1/2, x1/2, Nx), ...
                                    linspace(-y1/2, y1/2, Ny));
    dA1 = (x1/Nx) * (y1/Ny);
```

```
% z=0 initially
Z1_local = zeros(size(X1_local));

% Rotate about x-axis:
%   x' = x
%   y' = y*cos(alpha) - z*sin(alpha)
%   z' = y*sin(alpha) + z*cos(alpha)
% Because z=0, it simplifies to:
%   X1_rot = X1_local
%   Y1_rot = Y1_local * cos(alpha)
%   Z1_rot = Y1_local * sin(alpha)
X1_rot = X1_local;
Y1_rot = Y1_local .* cos(alpha_rad);
Z1_rot = Y1_local .* sin(alpha_rad);

% Now apply the additional shift along global y:
Y1_rot = Y1_rot + yOffset;

% The normal to surface 1:
% originally +z => after rotation about x => (0, -sin alpha, cos alpha)
N1x = 0;
N1y = -sin(alpha_rad);
N1z =  cos(alpha_rad);

%------------------------------
% SURFACE 2: parallel to xy-plane at z = d
% => normal is -z
% We'll subdivide surface 2
%------------------------------
num_x_sections = 3;
num_y_sections = 12;
F12_matrix = zeros(num_x_sections, num_y_sections);

dx2 = x2 / num_x_sections;
dy2 = y2 / num_y_sections;

Nx2 = 0;
Ny2 = 0;
Nz2 = -1;  % facing negative z

for i = 1:num_x_sections
   for j = 1:num_y_sections
```

```
% sub-panel in x2, y2
x2_min = -x2/2 + (i-1)*dx2;
x2_max = x2_min + dx2;
y2_min = -y2/2 + (j-1)*dy2;
y2_max = y2_min + dy2;

% Discretize sub-panel
[X2_local, Y2_local] = meshgrid(linspace(x2_min, x2_max, Nx), ...
                        linspace(y2_min, y2_max, Ny));
dA2 = (dx2 / Nx) * (dy2 / Ny);

% in global coords, surface 2 is at z = d
x2_global = X2_local;
y2_global = Y2_local;
z2_global = d * ones(size(X2_local));

%-----------------------------------
% Double integration
%-----------------------------------
F12 = 0;
for p = 1:Nx
   for q = 1:Ny
      % coords on surface 1
      x1p = X1_rot(p,q);
      y1p = Y1_rot(p,q);
      z1p = Z1_rot(p,q);

      for r = 1:Nx
         for s = 1:Ny
            % coords on surface 2
            x2p = x2_global(r,s);
            y2p = y2_global(r,s);
            z2p = z2_global(r,s);

            dx = x2p - x1p;
            dy_dist = y2p - y1p;
            dz = z2p - z1p;

            s2 = dx^2 + dy_dist^2 + dz^2;
            if s2 < 1.0e-15
               continue
            end
            dist_mag = sqrt(s2);
```

```
                % dot for cos_theta1
                dot1 = (N1x*dx + N1y*dy_dist + N1z*dz);
                cos_theta1 = abs(dot1) / dist_mag;

                % dot for cos_theta2
                dot2 = (Nx2*dx + Ny2*dy_dist + Nz2*dz);
                cos_theta2 = abs(dot2) / dist_mag;

                % dF
                dF = (cos_theta1 * cos_theta2) / (pi * s2);

                F12 = F12 + dF * dA1 * dA2;
              end
            end
          end
        end

        % shape factor from surface 1 to this sub-panel
        F12_matrix(i,j) = min(F12 / A1, 1);
      end
    end

    total_F12 = sum(F12_matrix(:));
    disp(['Total View Factor from Surface 1 to Surface 2: ', num2str(total_F12)]);
end
```

Appendix B- Experimental Results Using Two Ceramic Heaters

Table B.1 summarizes the experimental results including the effect of heater–filter distance, tilt angle and setpoint temperature on the minimum and maximum filter temperatures, heating duration, and energy consumption.

Table B.1. Experimental results for filter disinfection using two ceramic heaters

Tilt angle (α) (°)	**Distance (D) (cm)**	**Setpoint temperatures** (℃)	**Minimum temperature** (℃)	**Maximum temperature** (℃)	**Duration ($minutes$)**	**Is the filter disinfected?**	**Electrical Energy Consumption (kWh)**
0	10	180	34	93	3	NO	-
	15	180	50	88	25	NO	-
		200	43	96	5	NO	-
	25	200	61	82	25	NO	-
		220	70	95	25	YES	0.1
	35	200	63	75	25	NO	-
		220	72	80	17	YES	0.09
10	10	180	48	85	25	NO	-
		200	40	98	4	NO	-
	15	180	50	82	25	NO	-
		200	56	90	25	NO	-
		220	46	98	5	NO	-
	25	200	62	82	25	NO	-
		220	68	90	20	YES	0.12
	35	200	63	72	25	NO	-
		220	68	77	16	YES	0.1
20	10	180	49	80	25	NO	-
		200	54	90	25	NO	-
	15	180	51	76	25	NO	-
		200	56	90	25	NO	-
		220	51	93	5	NO	-
	25	200	60	76	25	NO	-
		220	68	88	22	YES	0.12
	35	200	61	73	25	NO	-
		220	69	80	21	YES	0.1

The results demonstrated that in shorter distances, increasing the tilt angle decrease the temperature differences over the filter significantly. while the effect of changing tilt angle at far

distances is not significant. For example, at distance 15 cm, setpoint temperature 180 ℃ after 25 minutes when the tilt angle is 0 °the temperature differences over the filter was 38 ℃ while this value decreases to 25 ℃ when the tilt angle rose to 20 °. On the other hand, the temperature difference at distance 35 cm remained constant approximately by increasing tilt angle. This suggests that adjusting the tilt angle is most effective in improving temperature uniformity when the heaters are positioned closer to the filter.